INSTITUTO TECNOLÓGICO DE AERONÁUTICA

João Pedro Turchetti Ribeiro

CONCURRENT IMAGING MODE DESIGN AND PERFORMANCE PREDICTION FOR EXPERIMENTAL SAR ACQUISITIONS USING TERRASAR-X

Final Paper
2021

Course of Electronic Engineering

CDU 621.396.96

João Pedro Turchetti Ribeiro

CONCURRENT IMAGING MODE DESIGN AND PERFORMANCE PREDICTION FOR EXPERIMENTAL SAR ACQUISITIONS USING TERRASAR-X

Advisor

Prof. Dr. Renato Machado (ITA)

Co-advisor

Thomas Kraus (DLR)

ELECTRONIC ENGINEERING

São José dos Campos
Instituto Tecnológico de Aeronáutica

2021

Cataloging-in Publication Data
Documentation and Information Division

Turchetti Ribeiro, João Pedro
Concurrent Imaging Mode Design and Performance Prediction for Experimental SAR Acquisitions using TerraSAR-X / João Pedro Turchetti Ribeiro.
São José dos Campos, 2021.
103f.

Final paper (Undergraduation study) – Course of Electronic Engineering– Instituto Tecnológico de Aeronáutica, 2021. Advisor: Prof. Dr. Renato Machado. Co-advisor: Thomas Kraus.

1. Synthetic Aperture Radar (SAR). I. Instituto Tecnológico de Aeronáutica. II. Title.

BIBLIOGRAPHIC REFERENCE

TURCHETTI RIBEIRO, João Pedro. **Concurrent Imaging Mode Design and Performance Prediction for Experimental SAR Acquisitions using TerraSAR-X**. 2021. 103f. Final paper (Undergraduation study) – Instituto Tecnológico de Aeronáutica, São José dos Campos.

CESSION OF RIGHTS

AUTHOR'S NAME: João Pedro Turchetti Ribeiro
PUBLICATION TITLE: Concurrent Imaging Mode Design and Performance Prediction for Experimental SAR Acquisitions using TerraSAR-X.
PUBLICATION KIND/YEAR: Final paper (Undergraduation study) / 2021

João Pedro Turchetti Ribeiro
Rua Elesbão Linhares, 394
29.055-340 – Vitória–ES

CONCURRENT IMAGING MODE DESIGN AND PERFORMANCE PREDICTION FOR EXPERIMENTAL SAR ACQUISITIONS USING TERRASAR-X

This publication was accepted like Final Work of Undergraduation Study

João Pedro Turchetti Ribeiro
Author

Renato Machado (ITA)
Advisor

Thomas Kraus (DLR)
Co-advisor

Prof. Dr. Marcelo da Silva Pinho
Course Coordinator of Electronic Engineering

São José dos Campos: November 18, 2021.

This paper is dedicated to my mentors and friends at DLR and ITA under whose constant guidance I have completed this thesis. They not only enlightened me with academic knowledge but also gave me valuable advice whenever I needed it the most.

Acknowledgments

First and foremost I would like to express my deepest gratitude to my parents – Maria Isabel Duarte Turchetti and João Carlos Magalhães Ribeiro –, not only for providing me with the best education, but also for encouraging me to pursue seemingly impossible challenges. None of this would have been possible without their support. I extend my gratitude to my girlfriend, brother and the rest of the family for always being truly supportive.

I would like to give special thanks to my co-advisor Thomas Kraus for receiving me at DLR and being extremely helpful and accessible. He is the responsible for guiding me, a previously illiterate in SAR technology, all the way to what is presented in this thesis. Similarly, I am very grateful for having Prof. Renato Machado as my advisor, who always enthusiastically gave me valuable advice and guidance to my academic life. I am forever grateful for the partnership between ITA and DLR made possible by my advisors.

Last but not least, I would like to thank everyone that has been part of my journey. Teachers, professors and friends from the schools and institutions I studied since young are immeasurably responsible for what I am today. This thesis is certainly the outcome of very hard work not only mine, but of everyone involved.

"Truth is ever to be found in simplicity,
and not in the multiplicity and confusion of things."
— SIR ISAAC NEWTON

Resumo

Stripmap e spotlight são os modos de aquisição mais utilizados e difundidos atualmente na indústria de radares de abertura sintética (SAR, *synthetic aperture radar*). Cada modo possui as suas próprias características e é usado de acordo com os requisitos do cliente. No entanto, existem situações nas quais ambos os modos são de interesse, tal como cenas nas quais não apenas uma visão geral, mas também uma imagem de resolução mais fina de uma pequena área se fazem necessárias. Nessas situações, a solução tradicional para obter ambas as imagens é esperar a próxima passagem do satélite pela região, o que pode demorar até 11 dias no caso do TerraSAR-X. O objetivo do trabalho de graduação em questão é projetar e validar uma técnica de aquisição concorrente no qual ambas as aquisições são executadas simultaneamente. Para isso, uma alta frequência de repetição de pulso (PRF, *pulse repetition frequency*) deve ser utilizada. Portanto, o trabalho foca, principalmente, nas restrições temporais e nas métricas de desempenho para avaliação das imagens. Por fim, são realizados experimentos práticos com o satélite em questão, utilizando dados reais para avaliar e validar o projeto e os resultados da técnica de imageamento proposta.

Abstract

Stripmap and spotlight have been the standard and most used acquisition modes in the synthetic aperture radar (SAR) industry. Each mode has its own characteristics and is used according to customers' requirements. However, there are situations in which both modes are of interest, namely scenes in which not only a broader view but also a high-resolution image of a small region are required. In these situations, the main solution to acquire both images is to wait until the next satellite approach to this region, which may take up to 11 days. This study aims to design and validate a concurrent imaging technique in which both acquisition modes are performed simultaneously. In order to make this possible, a very high pulse repetition frequency (PRF) must be used. Therefore, the study focuses mainly on timing constraints and imaging performance prediction. Finally, experiments with real data have been carried out to evaluate and validate the proposed imaging technique.

List of Figures

List of Tables

List of Abbreviations and Acronyms

AASR	Azimuth Ambiguity-to-Signal Ratio
AN	Ascending Node
DSP	Digital Signal Processing
FFT	Fast Fourier Transform
ISLR	Integrated Sidelobe Ratio
PRF	Pulse Repetition Frequency
PRI	Pulse Repetition Interval
PSLR	Peak-to-Sidelobe Ratio
SAR	Synthetic Aperture Radar
SNR	Signal-to-Noise Ratio
RAAN	Right Ascension of Ascending Node
RASR	Range Ambiguity-to-Signal Ratio
SM	Stripmap Mode
ST	Staring Spotlight Mode

List of Symbols

δ_{az}	Azimuth resolution
δ_{rg}	Slant range resolution
$\Pi\left(\frac{t}{T}\right)$	Rectangular function with length T
α_{os}	Oversampling ratio
$\alpha_{os,a}$	Azimuth oversampling ratio
BW	Chirp bandwidth
C_r	Compression rate
T	Pulse duration
f_s	Sampling frequency
f_d	Doppler frequency
K	Linear frequency rate
$h(t)$	Matched filter
$s_r(t)$	Noisy received signal
$y(t)$	Output of the matched filter
$\phi(t)$	Instantaneous phase of the chirp
$\mathcal{F}\{\cdot\}$	Fourier transform
σ	Backscatter coefficient
θ	Incidence angle
R	Slant range
R_0	Slant range of closest approach
λ	Wavelength of the carrier
v_s	Satellite speed
Δf_d	Processed Doppler bandwidth
Δ_{az}	Distance offset in azimuth
Δ_{rg}	Distance offset in range
v_g	Satellite ground speed
γ_w	Broadening factor
c_0	Speed of light in vacuum
B_r	Signal bandwidth
$\Delta\theta_{span}$	Total steering azimuth angle

Contents

1 Introduction

1.1 Context

The term Synthetic Aperture Radar (SAR) refers to a radar imaging technique discovered and first made functional in 1952 by Dr. Carl Wiley at the Goodyear Aircraft Corporation (Wiley, 1985). Twenty-six years later the first spaceborne satellite carrying a SAR sensor was made operational by the SEASAT mission in 1978. However, it is only since the ERS-1 launch in 1991 that SAR systems have been continuously orbiting and imaging the Earth's surface on a daily basis (Cumming; Wong, 2005) (Curlander; McDonough, 1991). At the current state of art, modern systems are capable of acquiring images with a resolution in the order of dozens of centimeters (Mittermayer *et al.*, 2014). When comparing to optical imaging, SAR systems are well known for being all weather, day and night operational. In other words, as these systems provide its own target illumination and are able to penetrate through clouds, they can acquire images regardless of bad weather or lack of sunlight.

This technique is a technical improvement of the side-looking airborne radars (SLAR). The latter consists of a real aperture imaging technique which is not suited to space applications as very long antennas are required to achieve reasonable azimuth resolution. To overcome this limitation, SAR systems synthesize a long aperture in azimuth by taking advantage of the relative movement between the target and the radar platform. As an example, a virtual 10 km long antenna can be synthesized from a physical length of 10 m in the direction of flight (NASA, [n.d.]). This improvements is enough to bring down the azimuth resolution of spaceborne systems from the order of kilometers to a few meters, thus turning the radar imaging implementation feasible.

In order to comply with different requirements, multiple imaging modes have been developed by the SAR community. These modes consist overall of a trade-off between resolution and image size. Namely, the Stripmap (SM), Staring Spotlight (ST) and ScanSAR (SC) are some of the operational modes of the German satellite TerraSAR-X (Cumming; Wong, 2005; Curlander; McDonough, 1991; Mittermayer *et al.*, 2014; Fritz; Eineder, 2013), which is the satellite under analysis in this work. This thesis has been developed in a partnership between the German Aerospace Center (DLR) and the Aeronautics Institute of Technology (ITA). All the commanding and acquisitions presented in this work were kindly made possible by colleagues at DLR.

The Stripmap and the Staring Spotlight modes are of most interest in this work and deserve a brief explanation in this section. The Stripmap is one of the most traditional and basic imaging mode and has been widely used since the ERS-1 mission. The main objective is to obtain a medium resolution image – approximately 1.2 m in range and 3.3 m in azimuth – of a long continuous strip of, theoretically, unlimited length and swath width of 30 km. The Stripmap azimuth coverage, however, is usually limited by satellite constraints on available power, thermal conditions and the amount of generated data. The Staring Spotlight mode brings an improvement in resolution to 0.6 m and 0.24 m in range and azimuth, respectively. However, the trade-off is a reduction in the scene size to a small patch of 4 km x 3.7 km (Airbus Defence and Space, 2015).

1.2 Motivation

One of the limitations of the current state-of-the-art imaging modes is the fact that only one mode can be used at a time. Due to the satellite's orbit geometry, there is a long interval of up to 11 days – period of the satellite often called repeat cycle – between consecutive flyovers of the radar to a given target on Earth. If two different acquisitions are required in nearby regions, then it may be necessary to wait almost up to two weeks. One possible solution would be to deploy a constellation of satellites at different orbit positions so that there is a shorter interval between similar acquisitions. However, this solution is clearly not cost-effective.

The motivation for this work is mostly to reduce the waiting interval between acquisitions in nearby regions. This is made possible by applying concepts of telecommunications, SAR theory, digital beamforming and orbital mechanics. This application would be specially useful in hotspots where there is a high demand for acquisitions, being Europe a good example.

1.3 Objective

The main objective of this Bachelor's thesis is to propose, design, test, and evaluate a concurrent imaging mode that would be able to obtain both Stripmap and Spotlight images in only one flyover. The idea consists of interleaving the beams of each mode in a pulse-to-pulse manner. With post-processing techniques the SAR data of each acquisition would be separated and focused.

This idea is also described in the literature, where a semi-operational implementation for the COSMO-SkyMed next-generation constellation is envisaged, focusing on the acquisition of two Spotlight acquisitions at the same time (Calabrese *et al.*, 2015). This thesis addresses the idea from the TerraSAR-X perspective, concentrating on the simultaneous acquisition of a Spotlight and a Stripmap product.

An intuitive first application is to gather medium resolution SAR data over a large area (Stripmap) while focusing with high resolution on a smaller region (Spotlight) of interest at the same time. However, there are many specific possibilities, as an example imaging simultaneously a large farm with medium resolution and its facilities with very high resolution. In commercial applications, it would be possible to perform the requests of two different clients at the same time and, therefore, potentially doubling revenues.

1.4 Thesis Outline

The thesis is divided into six chapters. The first chapter is this introduction to the topic, which presents the context, motivation, and objective of the work. Next, chapter two comes with a SAR background; more specifically, it brings concepts of timing diagram, matched filter, and ambiguity analysis. Chapter three presents the design of the proposed concurrent imaging mode by making use of the theoretical topics previously explained. Tests, evaluations and comparisons of the mode are shown in chapter four. Investigating the main drawbacks of the mode, some Earth coverage analysis and improvements are proposed in chapter five. Finally, chapter six provides an overview of the thesis, highlighting the main contributions and suggesting improvements for future work.

2 SAR Background

2.1 SAR Systems

One of the most important steps in SAR acquisitions is determining an appropriate pulse repetition frequency (PRF). The main constraints for the PRF are the satellite hardware, the required swath width and azimuth resolution, the Nadir interference, the receive window timing and the range and azimuth ambiguities (Cumming; Wong, 2005). This section will discuss these factors and, at the end, try to come up with the most appropriate PRF for a given set of acquisition parameters.

First, the satellite hardware constraints are defined mainly by its antenna and radar electronics limitations. In other words, if the transmission of the antenna can be switched on and off at the required rate and also if it can receive while switched off. Besides, it is also important to watch out for whether the electronics of the system and on-board mass memory are capable of dealing with the amount of data defined by the PRF and the sampling rate, as a higher PRF leads to more data into the memory.

The next constraint is the required swath width, which is tightly connected to the received echo window timings. As one would expect, a lower PRF implies a longer echo window, which in turn allows to receive reflected signals from further ground range positions. Therefore, it is possible to increase the swath width by lowering the PRF. However, by doing so, the azimuth bandwidth and resolution decrease the and ambiguity levels increase.

In order to comply with the conditions defined by the Nyquist theorem, a PRF higher than the azimuth bandwidth must be used. The ratio between these two parameters is defined as the azimuth oversampling factor and is usually about 1.1 to 1.4 (Cumming; Wong, 2005). By using a PRF lower than the Nyquist rate, the azimuth ambiguities drastically increase resulting in lower quality images. On the one hand, decreasing the PRF at a fixed oversampling rate reduces the azimuth bandwidth, which leads to a worse azimuth resolution. On the other hand, this lower PRF decreases the range ambiguity as the antenna receives signals from less interfering points. In summary, the PRF choice is a trade-off between swath width, azimuth resolution and range and azimuth ambiguities.

Finally, the most strict conditions are the Nadir and the transmission interferences, both defined by the receive window timing. These conditions define some prohibitive PRF values with which it is not possible to transmit without high information loss. The Nadir interference occurs when the antenna receives echoes from the Nadir line (satellite ground track) at the same time it receives the target echoes. The main problem is that Nadir echoes are characterized by its very high energy, which causes bright undesired streaks in the focused image. For the transmission interference, it is caused by the fact that the antenna transmits at a very high power, while the echoes are generally weak signals. Therefore, it is also not possible to use the antenna as a receiver while it is transmitting. These two restrictions are commonly identified in the so-called timing diagram.

2.2 Timing Diagram

As previously described, the timing diagram is an intuitive way to visualize the PRFs with which there are neither Nadir nor transmission interference at a given ground range position. To better visualize these interferences, it is helpful to observe the transmitted and received signals in time. Fig. 2.1 shows a transmitted signal in blue, point-target echo in green and the Nadir echo in orange. The simulation parameters are a PRF of 3100 Hz, an incidence angle of 38°, a satellite/platform height of 519 km and a duty cycle of 18%.

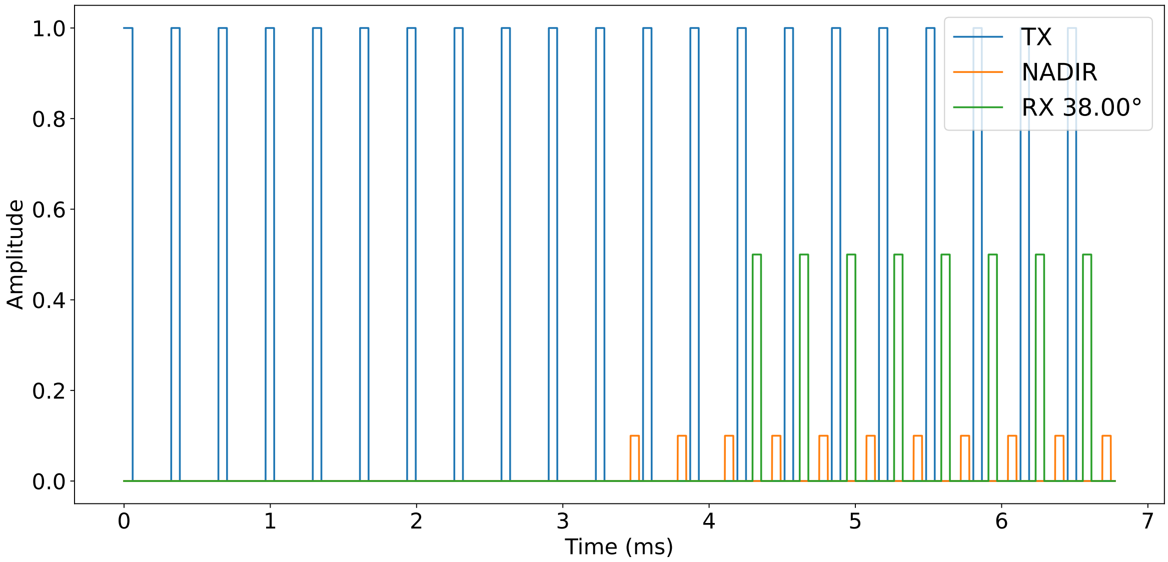

FIGURE 2.1 – Schematic plot in time of transmitted and received signals for a PRF of 3100 Hz, an incidence angle of 38°, a platform height of 519 km and a duty cycle of 18%.

From Fig. 2.1, it is possible to observe that the chosen set of conditions results in a non-interfering scenario. Nevertheless, varying any of the parameters may lead to a different scenario in which there is Nadir or transmission interference. Graphically, if the Nadir echo (orange) falls over the rising edge of the target echo (green), it is defined as Nadir interference. In a similar way, if the target echo falls over the transmitted signal (blue), it is defined as transmission interference.

As a method of summarizing these interferences, this simulation is run for a set of PRFs and incidence angles in order to check for each type of interference. The resulting graph of this simulation is the timing diagram. Using the same duty cycle and satellite height as before, but varying the PRF from 2 kHz to 7 kHz and the incidence angle from 20° to 70°, Fig. 2.2 is obtained.

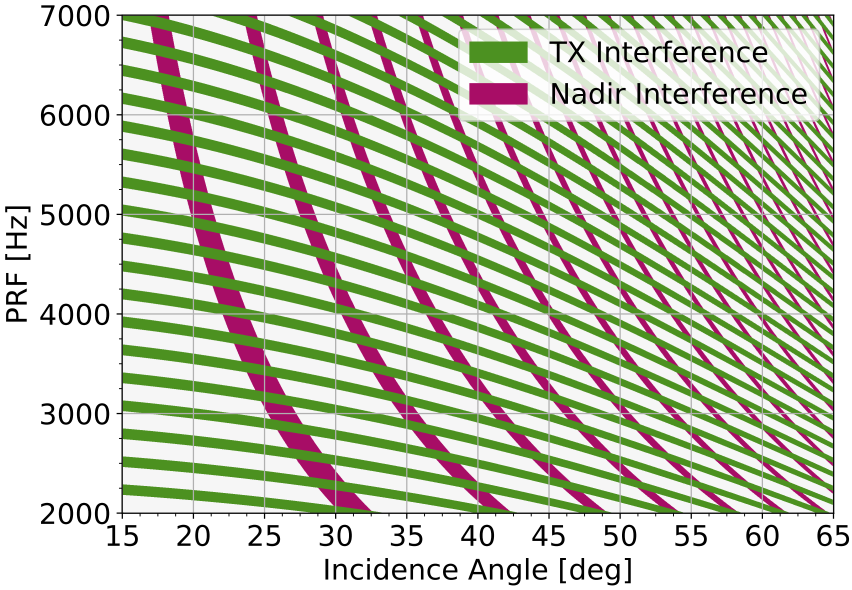

FIGURE 2.2 – Timing diagram as a function of the incidence angle for a satellite height of 519 km and duty cycle of 18%.

In Fig. 2.2, green stripes represent transmission interference, while the pink ones represent Nadir interference. The diagram can also be generated for fast time, ground range, look angle, and slant range domains. These diagrams are shown in Fig. 2.3 for information only.

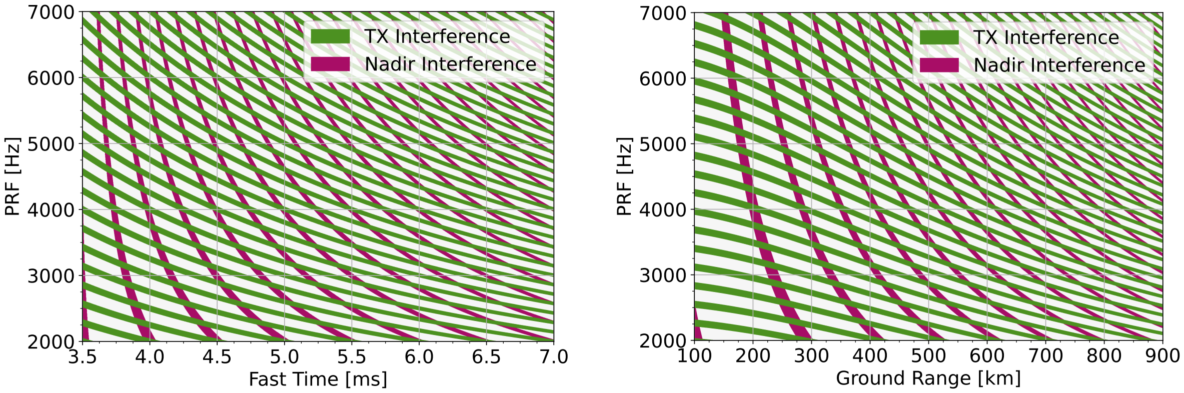

(a) Timing diagram in fast time domain.

(b) Timing diagram in ground range domain.

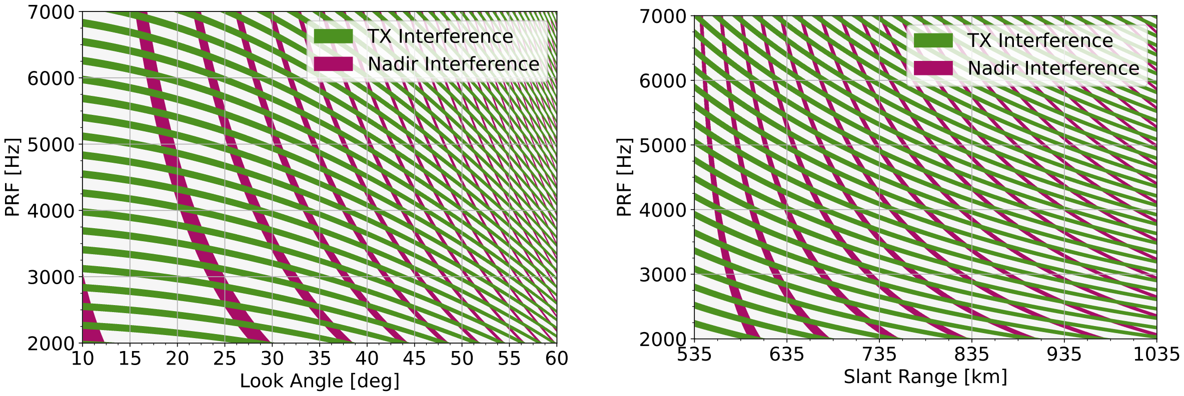

(c) Timing diagram in look angle domain.

(d) Timing diagram in slant range domain.

FIGURE 2.3 – Timing diagrams in different domains for a satellite height of 519 km and duty cycle of 18%.

The outcome of the timing diagram is, therefore, of great importance, as it determines the possible PRFs for each target region.

2.3 Matched Filter

Matched filtering is a well-known technique commonly used in radar systems. In signal processing, its main objective is to detect the presence of a given signal template in another noisy signal. The filter can be written as

$$y(t) = \int_{-\infty}^{\infty} s_r(u)h(t-u)du = (s_r * h)(t), \tag{2.1}$$

given that $h(t) = g^*(-t)$ is the time-reversed complex conjugate of the template $g(t)$, $s_r(t)$ is the noisy received signal and $y(t)$ is the output of the matched filter.

In SAR systems, pulse compression is the main application of the matched filter. This technique is used in order to cope with the limited peak transmission power, maximize SNR and also to achieve better image resolutions. However, before going into the datails of pulse compression, the transmitted signal must be analyzed.

2.3.1 Chirp

Chirp is the name given to the pulsed transmitted signal when the frequency is increasing or decreasing during pulse duration. So as to achieve an uniformly filled bandwidth, the chirp is generated from a linear time-varying frequency sweep. It is important to notice that signals in this section will be analyzed in baseband. It can be written as

$$f(t) = \frac{1}{2\pi}\frac{d\phi(t)}{dt} = Kt \Longrightarrow \phi(t) = \pi K t^2 + \phi(0), \tag{2.2}$$

given f the signal frequency, ϕ the phase, t the time variable and K the linear frequency rate.

Therefore, considering a zero initial phase, the transmitted signal can be written as

$$s(t) = \Pi\left(\frac{t}{T}\right)\exp\left\{j\pi K t^2\right\}, \tag{2.3}$$

given that T is the pulse duration and the rectangular function is defined as

$$\Pi(t) = \begin{cases} 0, & \text{if } |t| > \frac{1}{2} \\ 1, & \text{if } |t| \leq \frac{1}{2}. \end{cases} \tag{2.4}$$

As an example, one can assume a signal with its frequency varying from -75 MHz to 75 MHz (bandwidth = 150 MHz) in $T = 4$ μs. This set of parameters results in the chirp as depicted in Fig. 2.4.

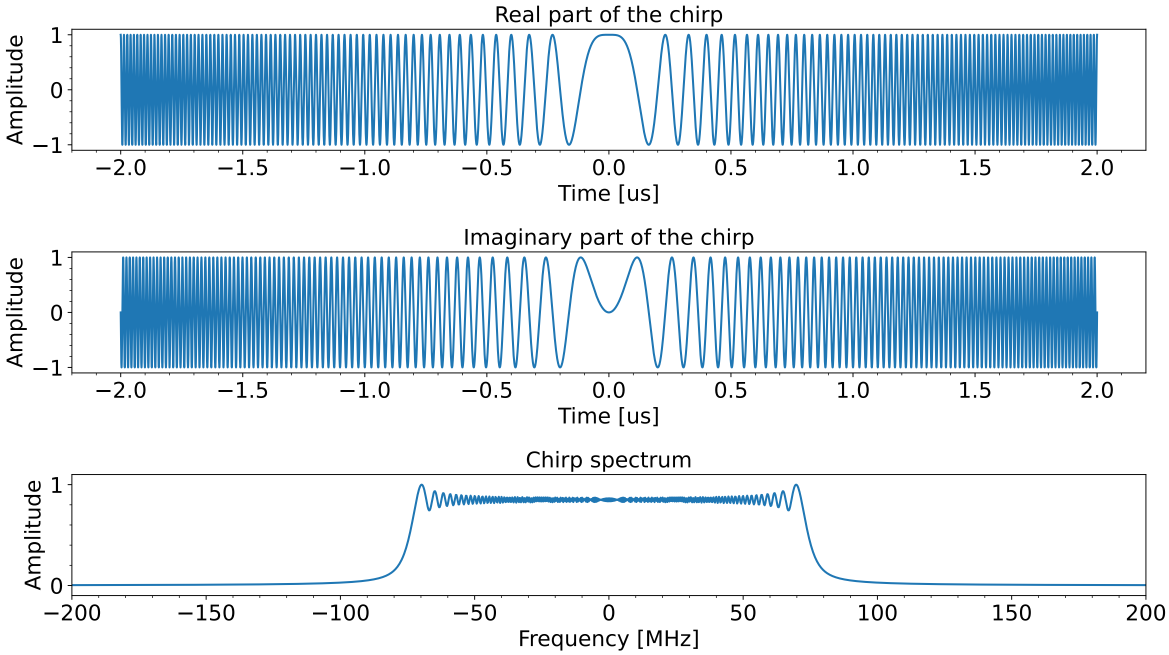

FIGURE 2.4 – Baseband chirp in time and frequency domains.

The oversampling ratio α_{os} is defined as

$$\alpha_{os} = \frac{f_s}{\mathrm{BW}}, \tag{2.5}$$

given f_s the sampling frequency and $\mathrm{BW} = |K|T$ the chirp bandwidth. This value is usually between 1.1 and 1.4 (Cumming; Wong, 2005). Fig. 2.4 uses an oversampling factor of 100 in order to improve visualization and smoothness of the plots.

In possession of the chirp as described, the pulse compression can be achieved by applying the matched filter to the received signal.

2.3.2 Pulse Compression

The urge to apply the pulse compression technique to radar systems comes from the necessity of achieving fine resolutions, which is obtained by using or synthesizing short pulses in the transmitted signal.

The first intuitive approach to improve the resolution would be to reduce the pulse duration T. However, the reduced average power would result in worsening the SNR of the received signal. To compensate this problem, it would be enough to increase the peak power of the transmitted signal. This solution, nonetheless, is limited by the hardware, as it is not always physically feasible to simply increase the peak power. Pulse compression is the technique used to solve this problem. In other words, signal processing is used to achieve a fine image resolution by exploiting the properties of a chirped waveform, namely a peak-like autocorrelation function. This method does not induce any SNR problems, as it still uses long pulses with a reasonable peak power.

As previously discussed, pulse compression is obtained through a matched filter. For SAR systems, the transmitted signal is known and has been described as the chirp. Analyzing the signal received by the antenna, the simplest solution is to use a copy of the transmitted signal shifted in time by t_0 and attenuated in amplitude by a factor L. In this case, the channel is simplified to only contribute with delay and attenuation. It is not the objective here to obtain the best modeling of the transmission by including noise and other effects, but only to clarify the pulse compression technique. Therefore, the filter to be applied and the received signal can be respectively written as

$$h(t) = s^*(-t) = \Pi\left(\frac{t}{T}\right) \cdot \exp\left\{-j\pi K t^2\right\} \text{ and} \tag{2.6}$$

$$s_r(t) = L \cdot \Pi\left(\frac{t-t_0}{T}\right) \cdot \exp\left\{j\pi K (t-t_0)^2\right\}. \tag{2.7}$$

The implementation of the matched filter can be performed by two main algorithms. On the one hand, it is possible to simply apply the convolution in the time domain as described in Equation (2.1). This method is reasonable for short arrays with size generally not longer than 500 as it is very inefficient. On the other hand, it is possible to convolute the signal and the filter by applying a fast Fourier transform (FFT) and finally simply multiply the signal and the filter in the frequency domain. This method outperforms the first one for long arrays, but may be slower for very short ones. The second method is defined by

$$y(t) = \mathcal{F}^{-1}\{\mathcal{F}\{s_r(t)\} \cdot \mathcal{F}\{h(t)\}\}. \tag{2.8}$$

It is important to notice that once the simulation is being performed by a computer, all signals must be discretized. Consequently, in Equation 2.8 the Fourier transforms must be seen as FFTs and the variables as discrete arrays. Applying the matched filter to the chirp introduced in Fig. 2.4, the output compressed pulse is obtained. Both the amplitude and the magnitude in dB of the normalized output are depicted in Fig. 2.5.

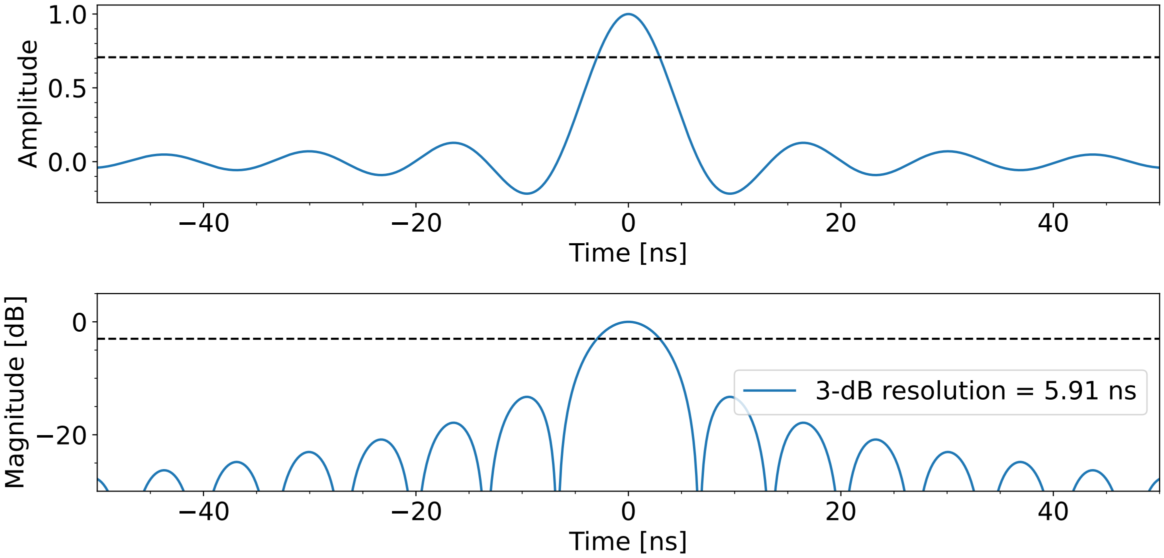

FIGURE 2.5 – Normalized output of a matched filter applied to a chirp signal with bandwidth of 150 MHz and duration of 4 μs.

From the output of the matched filter presented, two main conclusions can be drawn. First, the resulting sinc-like behavior is clear and consistent with what is expected by analytical means (Cumming; Wong, 2005). Second, from the main lobe of the output sinc, it is possible to extract the resulting pulse duration, or resolution. This resolution is defined by the -3 dB points of the main lobe. Besides, it can also be described by the compression ratio C_r. This ratio is defined by the reduction in duration between the chirp signal and the resolution of the output signal. From the result obtained in Fig. 2.5, the compression rate can be calculated by

$$C_r = \frac{\text{Chirp Duration}}{\text{Output Resolution}} \approx \frac{4 \cdot 10^{-6}}{5.91 \cdot 10^{-9}} \approx 677. \tag{2.9}$$

The compression ratio was obtained by simulation, but it can also be calculated analytically by

$$C_r = \frac{T}{0.886/(|K| \cdot T)} = \frac{\text{BW} \cdot T}{0.886} = \frac{\text{TBP}}{0.886} \approx 677, \tag{2.10}$$

where TBP $= \text{BW} \cdot T$ stands for the time bandwidth product.

2.4 Ambiguities

Other decisive factors in choosing the most adequate PRF are the ambiguities. Ambiguities happen when signals from spurious points on Earth are mistakenly mixed with the target echoes. The results are images stained with undesired blurs. They can occur both in ground range and in azimuth as indicated by their names – Range Ambiguity-to-Signal Ratio (RASR) and Azimuth Ambiguity-to-Signal Ratio (AASR). However, it is important to notice that they have different causes and a contradicting behavior and, therefore, must be analyzed independently. Ultimately, the main objective of analyzing ambiguities is to obtain the PRF for which the ambiguities are minimized to improve the overall image quality.

2.4.1 RASR - Range Ambiguity-to-Signal Ratio

The RASR will be analyzed first because it is more intuitive and thus facilitates the understanding of the AASR.

Ambiguities in ground range occur when undesired echoes reach the antenna at the same time as the target echoes. For a given PRF, the antenna transmits and receives every $\text{PRI} = \frac{1}{\text{PRF}}$. Then, if a certain point on Earth is at an integer multiple of PRIs away from the target, its echo will reach the antenna at the same time as the next or previous target echoes. This overlap in the received signals is the cause of the range ambiguity.

Fig. 2.6 depicts a range ambiguity scenario. The platform is represented by the hexagon and is flying into the page. The targets are represented by the green and red symbols and are separated in ground range on the Earth's surface. The satellite in this situation is imaging the green target, which has a slant range of R_1 and an echo delay of τ_1. The undesired red target, which is at a distance of R_2 from the satellite, is one PRI away in the time domain ($\tau_1 = \tau_2 + \text{PRI}$). In other words, the echoes from the red target arrive one PRI sooner than those from the green target. This leads to an overlapping between the echoes. This interference in the end degrades the image quality. This effect is named range ambiguity.

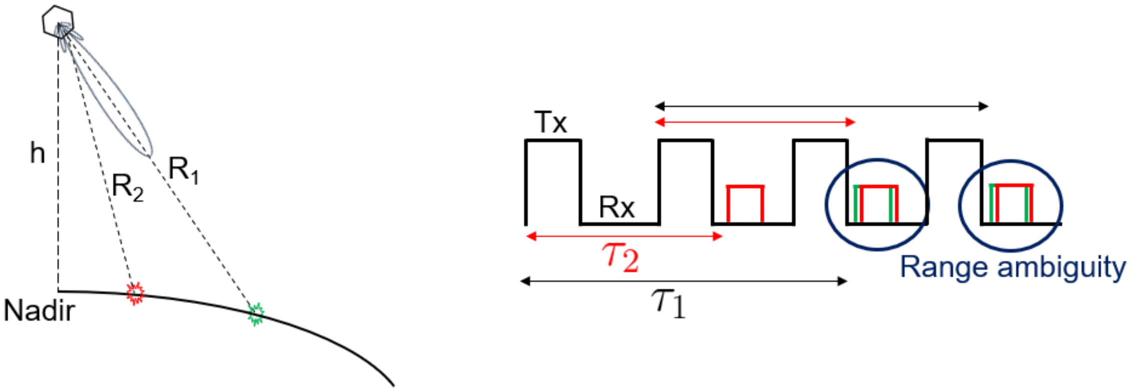

FIGURE 2.6 – Representation of a scenario contaminated with range ambiguities.

To obtain the RASR value it is necessary to know not only which points on Earth cause the ambiguities, but also what is the target region and a model of the reflectivity of the Earth. Therefore, to predict RASR performance by means of simulation, it is mandatory to know the antenna pattern, the satellite positioning, and to select a target region. Besides, a backscatter model (σ_0) for the terrain must also be known previously. This model is defined based on the incidence angle and provides information about the reflectivity of the scene. The further away from the Nadir line, the weaker the scene reflects back to the satellite antenna.

In summary, the main input variables for the simulation are the PRF range, the antenna pattern, the target region and the platform height. Aside from that, the simulation can be run for two different scenarios. First, it is possible to consider point-like targets in a given target region and calculate the RASR for each one of them. Then, the overall scene RASR can be calculated by the mean of each point-like RASR. The other option is to consider the whole target region and calculate the RASR by integrating over the ambiguity areas.

Fig. 2.7 depicts the RASR for point-like targets using different platform heights to demonstrate its influence as an horizontal shift in the PRF axis.

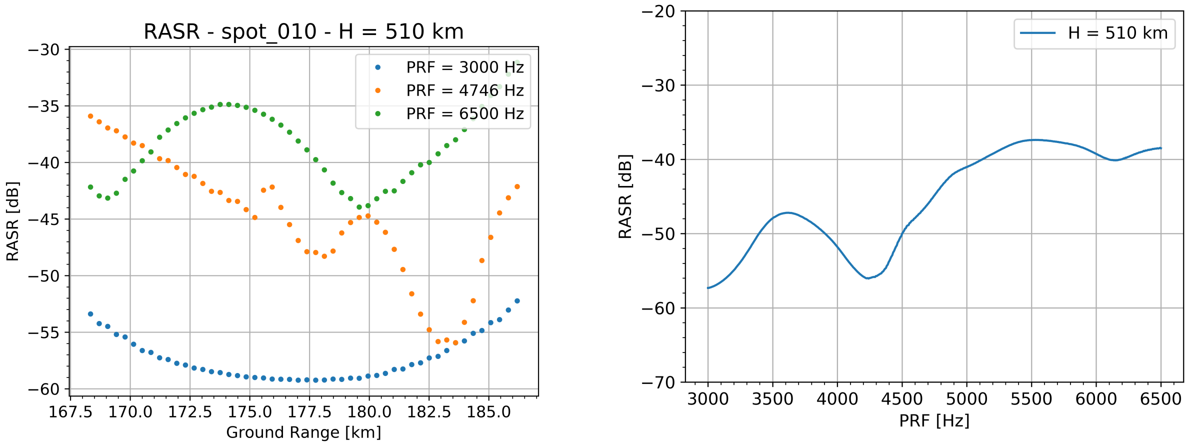

(a) RASR for each ground-range target.

(b) Average RASR for each PRF.

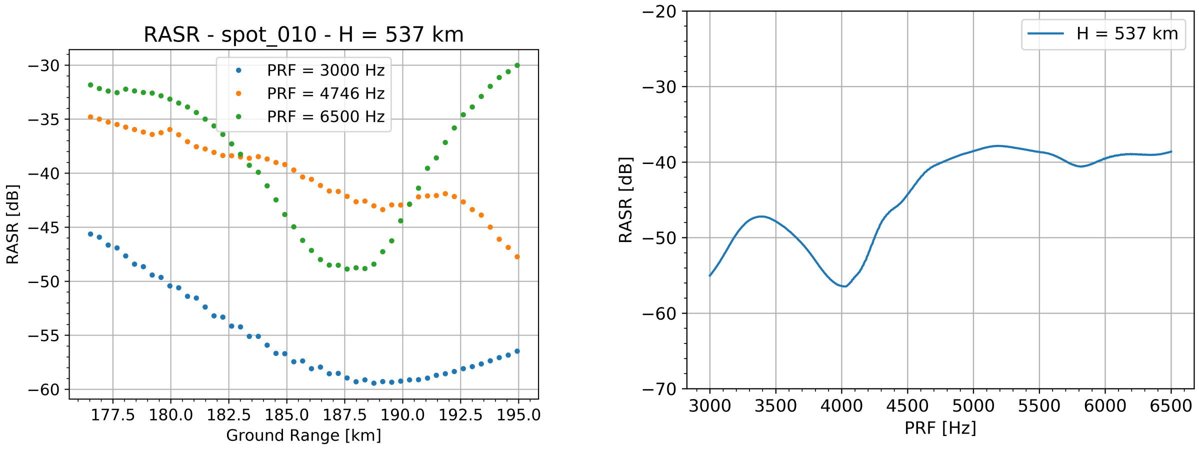

(c) RASR for each ground-range target.

(d) Average RASR for each PRF.

FIGURE 2.7 – RASR obtained for point-like targets and different platform heights.

In order to understand how the RASR is obtained for point-like targets, the power received from both the target and the ambiguity points are essential. In Fig. 2.8, the blue vertical line represents the sum of the two way antenna gain and the backscatter model of the target, while the red lines represent the same for the ambiguity points. After dividing each point on the graph by the third power of its respective slant range and the sine of the incidence angle, the RASR is calculated as the ratio between the sum of the red points and the blue one. This equation can be represented by (Curlander; McDonough, 1991)

$$\mathrm{RASR} = \frac{\sum_{m=1}^{M} P_{amb,m}}{P_{target}} = \frac{\sum_{m=1}^{M} \dfrac{G_{two-way,m} \cdot \sigma_{0,m}}{\sin\theta_{i,m} \cdot R_0^3}}{\dfrac{G_{two-way,0} \cdot \sigma_{0,0}}{\sin\theta_{i,0} \cdot R_0^3}}, \tag{2.11}$$

in which m and 0 represent the m-th ambiguity and the target, respectively.

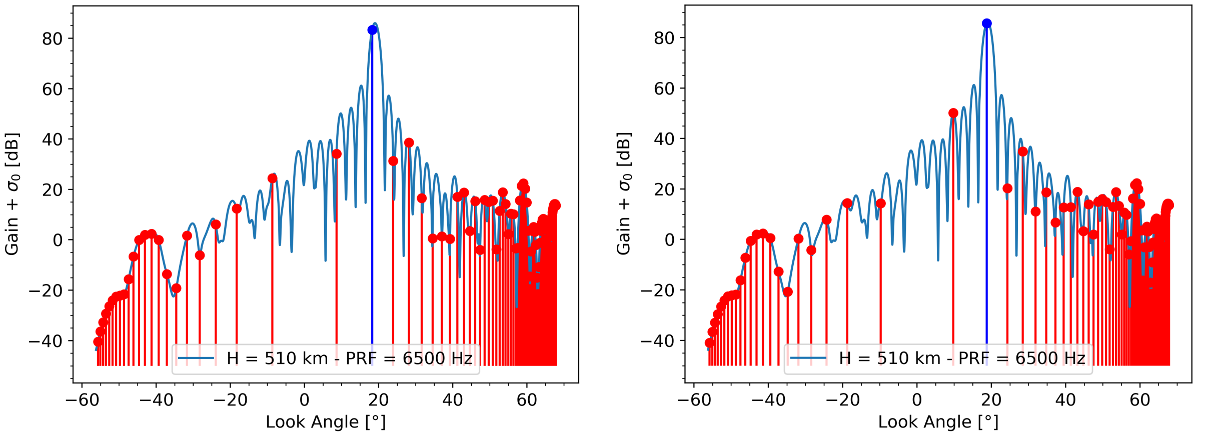

(a) Ambiguity points for ground range = 169.0 km.

(b) Ambiguity points for ground range = 174.1 km.

FIGURE 2.8 – Power received and ambiguity points for different point-like target positions.

Analyzing distributed areas instead of point-like targets, the RASR results are depicted in Fig. 2.9.

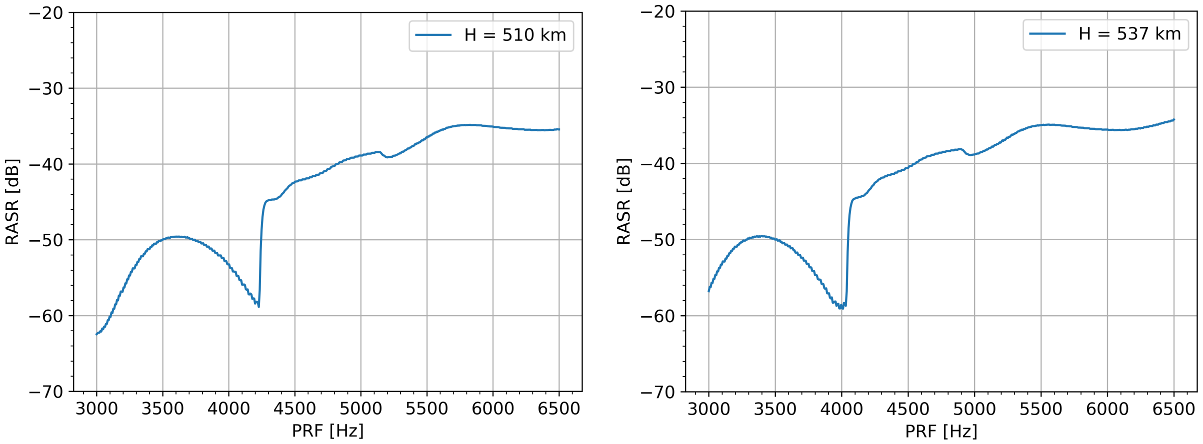

(a) RASR for a distributed target and H = 510 km.

(b) RASR for a distributed target and H = 537 km.

FIGURE 2.9 – RASR obtained for distributed targets and different platform heights.

Comparing Figs. 2.7 and 2.9, a similar behavior is observed. The use of one method over the other depends on the analysis that is being performed. Equation 2.11 shows how to obtain the RASR of a single point target. Then, the RASR of the whole scene depends on whether the definition is the mean of multiple point-like targets or one distributed target.

As it can be observed from Fig. 2.9, the RASR tends to increase with increasing PRF values. This result is intuitive, as lowering the PRI increases the amount of ambiguity points/regions on the Earth surface. However, the RASR curves are not strictly monotone because of the variations of the antenna pattern, which is usually represented by a sinc-like function.

In order to understand how the RASR is obtained for distributed areas, the power received from both the target region and the ambiguity regions are essential. In Fig. 2.10, the blue area represents the sum of the two way antenna gain and the backscatter model of the target region, while the red areas represent the same for the ambiguity regions. After dividing each point on the graph by the third power of its respective slant range, the RASR is calculated as the ratio between the sum of the red areas and the blue one.

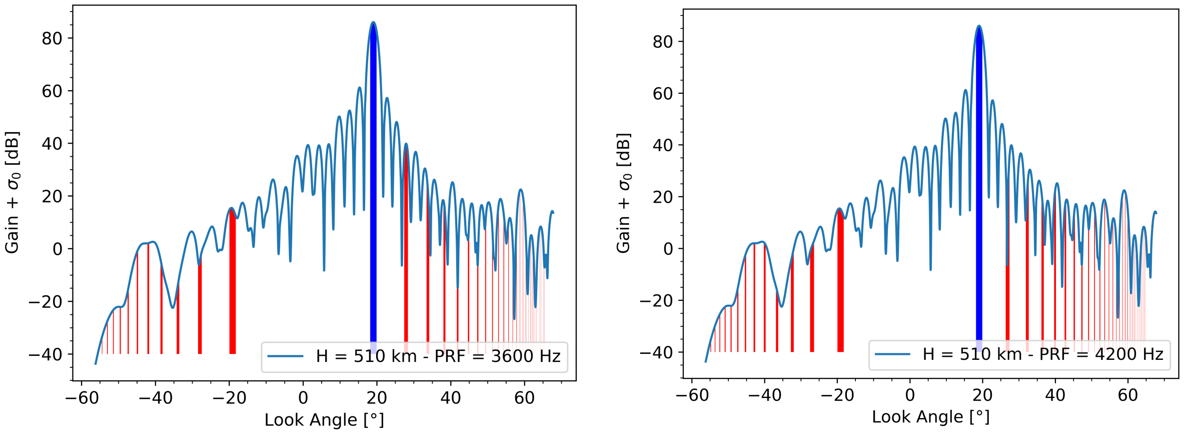

(a) Ambiguity regions for PRF = 3600 Hz. (b) Ambiguity regions for PRF = 4200 Hz.

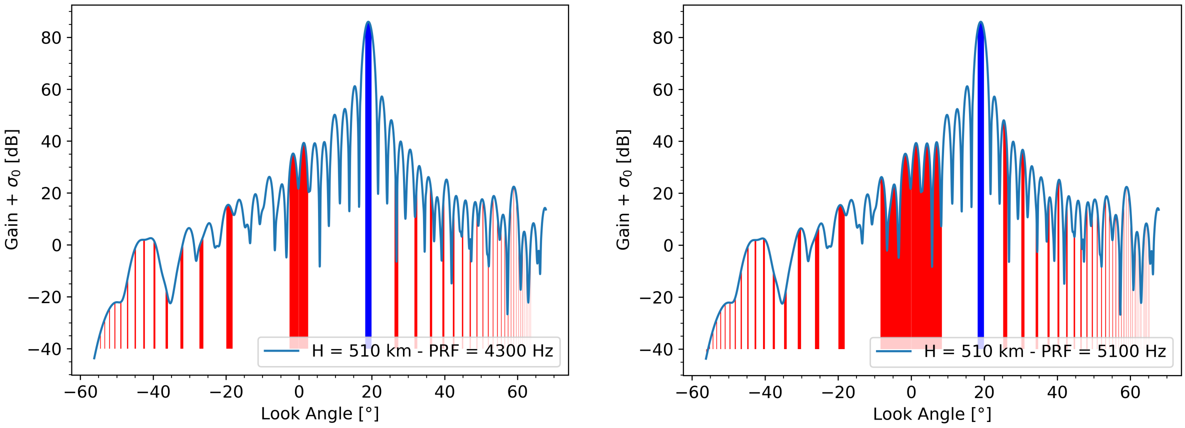

(c) Ambiguity regions for PRF = 4300 Hz. (d) Ambiguity regions for PRF = 5100 Hz.

FIGURE 2.10 – Power received and distributed range ambiguity regions for different PRFs.

In Fig. 2.10, it is possible to notice some interesting progressions. First, from Fig. 2.10a to 2.10b, the main ambiguity region went into a low antenna gain area. This explains the RASR decrease in Fig. 2.9a from 3600 Hz to 4200 Hz. Then, in Fig. 2.10c and 2.10d, ambiguities appear at low look angles, resulting in large ambiguity regions and increase in RASR.

The main objective of these results is to find a PRF that minimizes the ambiguities. From Figs. 2.7d and 2.9b, it is possible to conclude that, for a satellite height of 537 km, a PRF around 4 kHz would minimize the RASR. However, the AASR has an opposite behavior. In other words, it decreases with increasing PRF. Hence, it is necessary to analyze both range and azimuth ambiguities to find a PRF that provides a good trade-off.

2.4.2 AASR - Azimuth Ambiguity-to-Signal Ratio

The ambiguities in azimuth are caused by an effect similar to those in range. However, instead of signals being mixed because they arrive at the receptor at the same time, they are mixed for reaching with an equivalent Doppler frequency shift. To better understand this effect, it is important to first discuss how signals behave in azimuth direction.

For a given point on Earth, it is intuitive to notice that the SAR antenna first gets closer then goes away. In the slant range plane, as represented in Fig. 2.11, the variation of distance in time can be written as

$$R(t) = \sqrt{R_0^2 + (v_s t)^2}. \tag{2.12}$$

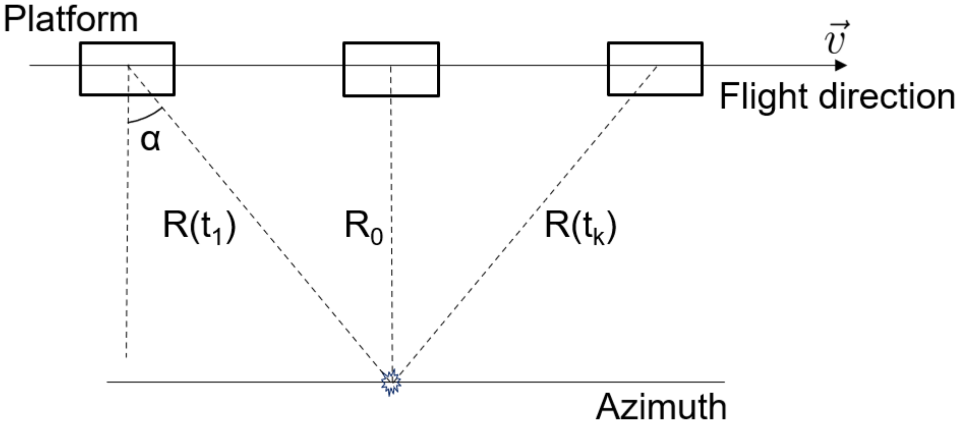

FIGURE 2.11 – Acquisition geometry in the slant range plane.

Therefore, from the Doppler effect, the signal frequency is shifted based on the relative speed between the antenna and the target. The Doppler frequency shift f_d can be written as

$$2\pi f_d = \frac{\partial}{\partial t}\left(-\frac{4\pi}{\lambda}R(t)\right), \tag{2.13}$$

which results in

$$f_d = -\frac{2}{\lambda}\frac{v_s^2 t}{\sqrt{R_0^2 + v_s^2 t^2}} \approx -\frac{2}{\lambda}\frac{v_s^2 t}{R_0}, \tag{2.14}$$

given v the satellite speed, λ the signal wavelength, R_0 the minimum distance between the satellite and the target and t the slow time.

From a signal processing point of view, it is important to notice whether these frequencies will be respected by the sampling rate. In the azimuth direction, this rate is given by the pulse repetition frequency (PRF). Usually the PRF is up to 7 kHz, while the Doppler shift may vary from -70 kHz to +70 kHz. Thus, it is clear that the azimuth sampling rate is not high enough to differentiate every incoming Doppler frequency.

From the low sampling rate as stated and the Nyquist theorem, it can be concluded that every f_d above $\frac{\text{PRF}}{2}$ and under $-\frac{\text{PRF}}{2}$ will be seen as frequencies between these two values. This effect of folding back high frequencies is the cause of azimuth ambiguities.

The AASR can be obtained by (Curlander; McDonough, 1991)

$$\text{AASR} \approx \frac{\displaystyle\sum_{\substack{m=-\infty \\ m\neq 0}}^{\infty} \int_{-\Delta f_\text{d}/2}^{\Delta f_\text{d}/2} G^2(f + m f_p) df}{\displaystyle\int_{-\Delta f_\text{d}/2}^{\Delta f_\text{d}/2} G^2(f) df}. \tag{2.15}$$

In Equation (2.15), Δf_d is the processed azimuth (or Doppler) bandwidth and can be related with the PRF by the azimuth oversampling factor $\alpha_{os,a}$ as

$$\alpha_{os,a} = \frac{\text{PRF}}{\Delta f_\text{d}} > 1. \tag{2.16}$$

As this factor gets closer to the unity, the higher will be the azimuth bandwidth, resulting in better azimuth resolution. As a trade-off, it increases the AASR. The opposite effect happens if this factor is increased.

The most common approach to find the oversampling factor is defining a maximum allowed AASR and and consequently determining the minimum factor that satisfies it.

Fig. 2.12 depicts how the AASR behaves for different oversampling factors.

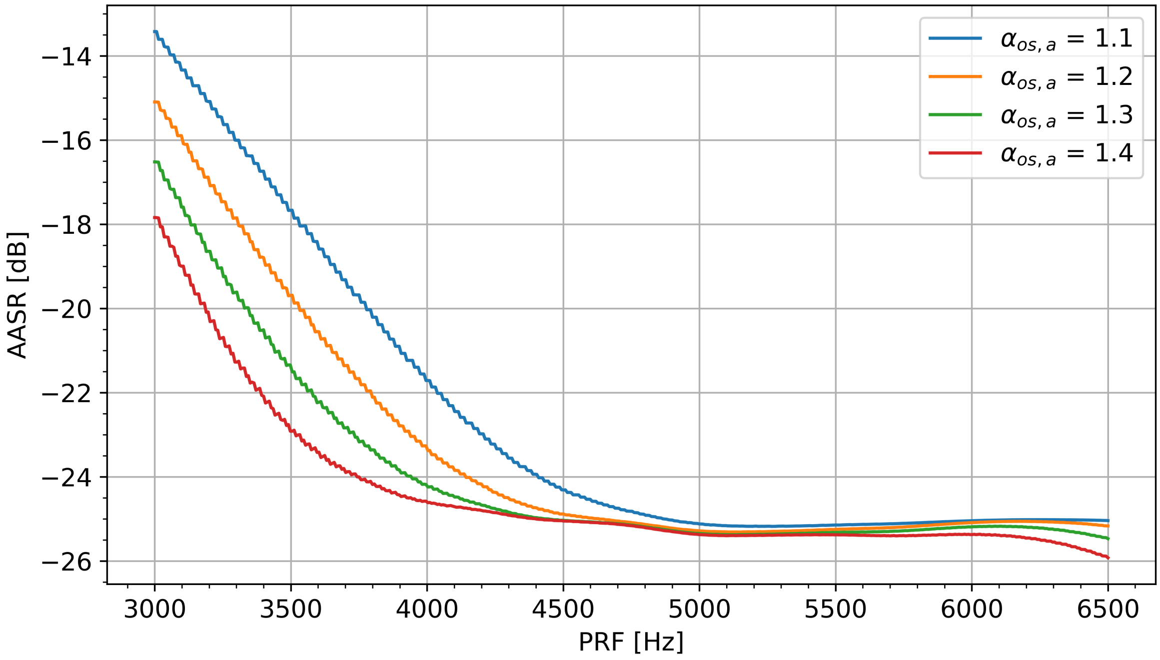

FIGURE 2.12 – AASR behavior for different azimuth oversampling factors.

As expected, lower PRFs result in higher AASR due to those frequencies obtained by high antenna gains being folded back as ambiguities. Besides, it is also clear that lower oversampling factors also result in worse AASR, also due to more frequencies being considered as ambiguous.

All results were obtained for a zero squint angle, satellite speed of approximately 7600 m/s and signal carrier frequency of 9.65 GHz.

In order to better visualize how the AASR is obtained for point-like targets, the antenna gain for each received Doppler frequency is essential. In Fig. 2.13, the blue area represents the two way antenna gain of the processed bandwidth, while the red ones represent the gain from the ambiguity frequencies. The AASR is calculated as the ratio between the sum of the red areas and the blue one, as stated in Equation (2.15).

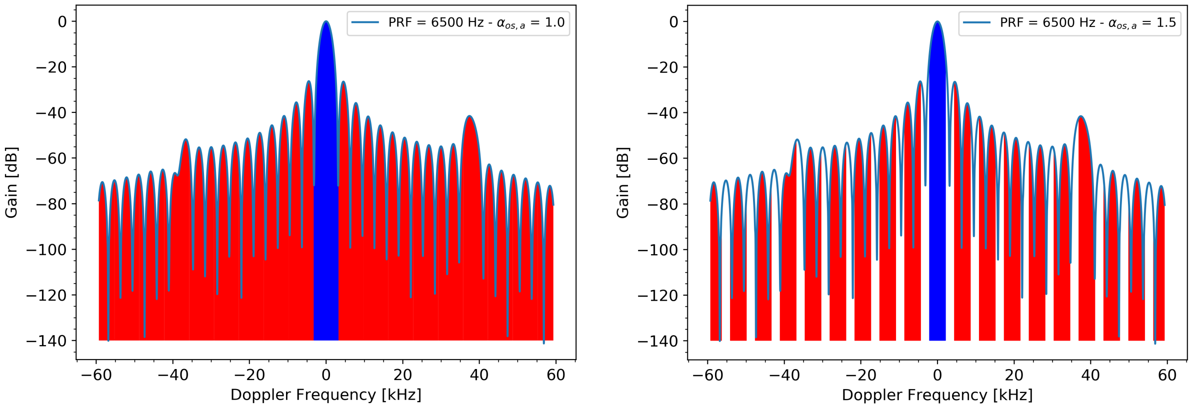

(a) Ambiguity frequencies for $\alpha_{os,a} = 1.0$.

(b) Ambiguity frequencies for $\alpha_{os,a} = 1.5$.

FIGURE 2.13 – Power received and azimuth ambiguity frequencies for different oversampling factors and a PRF of 6500 Hz.

2.4.3 ASR - Ambiguity-to-Signal Ratio

Once both ambiguities are obtained, the next step is obtaining the best trade-off between range and azimuth ambiguities. One possibility is by defining the Ambiguity-to-Signal Ratio (ASR) as

$$\mathrm{ASR} = \mathrm{RASR} + \mathrm{AASR}. \tag{2.17}$$

Equation 2.17 results in a curve representing the total amount of ambiguities in the scene. From this curve, the point of minimum is of interest as it can be understood as the point of best image performance in terms of ambiguities. Then, given a maximum ASR allowed, it is possible to obtain a PRF range with which the final image can be generated with an acceptable level of ambiguities.

As an example, one can consider a Stripmap acquisition with zero squint angle, a fixed incidence angle and $\alpha_{os,a} = 1.2$. Given this set of conditions and calculating RASR, AASR and ASR, Fig. 2.14 is obtained.

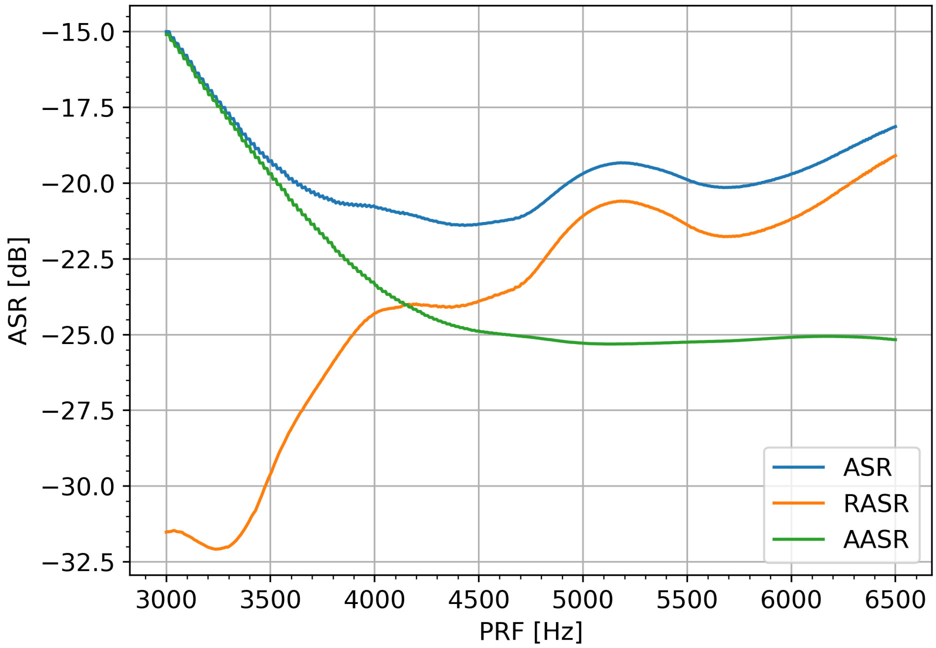

FIGURE 2.14 – Ambiguity-to-signal ratio as a function of PRF for a zero squint angle acquisition, satellite height of 510 km and azimuth oversampling factor of 1.2.

From Fig. 2.14, it is noticeable that the region of minimum ASR is around 4.4 kHz. Therefore, considering a maximum ASR allowed being approximately -20 dB, the PRF range would be between 3600 kHz and 4900 kHz.

This analysis can be made for every intended acquisition in order to avoid getting images blurred by ambiguities. Even though the result obtained is of great value, this analysis must be refined for more specific and accurate applications. In other words, to calculate the RASR neither the ellipsoid model of the Earth nor any specific backscatter model was considered. Besides, for the AASR, squint angles different than zero should be considered when required. These and many other factors must be examined in order to obtain a finer ambiguity analysis.

The following chapter is responsible for designing a new acquisition mode with more refined predictions. Not only the ellipsoid model of the Earth, but also the real TerraSAR-X trajectory and attitude are considered. It will be shown that ambiguities are of special interest in this proposed mode and, therefore, must be carefully analyzed.

3 Concurrent Imaging Mode Design

A concurrent imaging mode is the name given to the new acquisition mode proposed in this thesis. Its main idea is to interleave Stripmap and Spotlight beams in order to acquire both images during a single approach over a target. There are two main constraints that need to be overcome in order to make this concurrent acquisition possible. First, it is important to ensure the signals are properly placed from a timing point of view. Second, ambiguities must also be analyzed in order to avoid strong image degradation. In summary, the PRF must be properly chosen to guarantee a sufficient quality of the image. The PRF selection is specially important in this concurrent acquisition as two acquisitions are being made at the same time and, therefore, it is necessary to use a high PRF in order to get reasonable images in terms of azimuth resolution and ambiguities. The objective of this section is to, given a target on Earth, determine a suitable PRF and assess the quality of both Stripmap and Spotlight images.

As every target on Earth is different in terms of incidence angle and satellite position, it is important to define a specific one in order to design an optimum PRF and evaluate the acquisition. The procedure of designing the best parameters is, naturally, similar for different targets. In the following analysis, it was decided to use the region of Surat Basin, Queensland, Australia as a target due to the existence of a group of 40 corner reflectors distributed in a region of roughly 125 km x 125 km. More specifically, the Surat Basin CR 20 was chosen, a 1.5 m trihedral corner reflector, as the scene center (Garthwaite *et al.*, 2015).

3.1 Timing Analysis

The first step of the timing analysis is to avoid Nadir and transmission interference. This result can be easily obtained from the timing diagram, which is depicted in Figure 3.1.

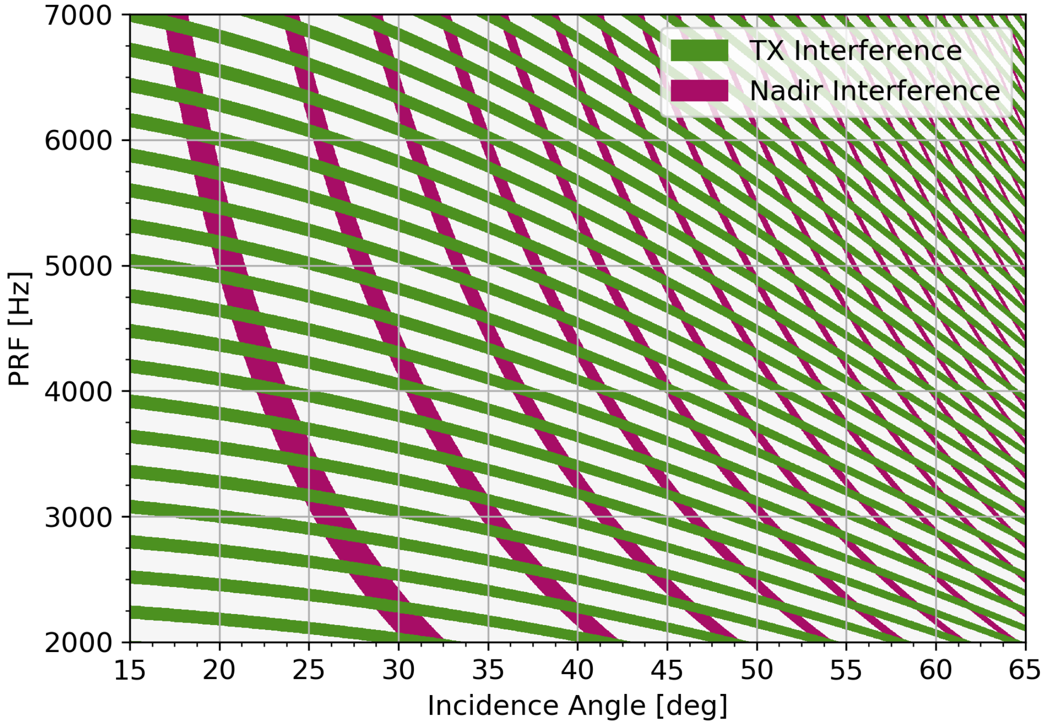

FIGURE 3.1 – Timing diagram of the acquisition over Australia as a function of the incidence angle.

In the diagram presented, the pink regions represent the combinations which result in Nadir interference, while the green lines represent the transmission interference. Therefore, at a first glance, every region in white can be used. However, there are still some limitations from a timing point of view that must be taken into account.

Besides the target center position, the scene will naturally have a certain length in ground range. This scene size can be seen in the timing diagram as a range of incidence angles. Consequently, a minimum scene size must be defined. The scene will define the minimum and the maximum incidence angle during the acquisition. This incidence angle range must be entirely respecting the timing diagram.

The other limitations are related to the satellite itself. Due to hardware constraints, the SAR instrument cannot acquire at every possible PRF. There is a list of about 500 discrete values between 2 kHz and 7 kHz that the satellite can use. Besides, after a given mode transmission, there must be a reception of the same mode. In other words, the order of the signals must be Stripmap transmission, Stripmap reception, Spotlight transmission, Spotlight reception, Stripmap transmission and so on. This timing constraint can be calculated from the number of traveling pulses, i.e., there must be an even number of pulses between the satellite antenna and the surface of the Earth so that the pulses will reach the antenna at a correct timing position. This must be taken into account due to the fact that the acquisition modes will likely use different antenna patterns.

The restriction described is visualized in Figure 3.2, which depicts the signals in time and a zoomed in version in Figure 3.3.

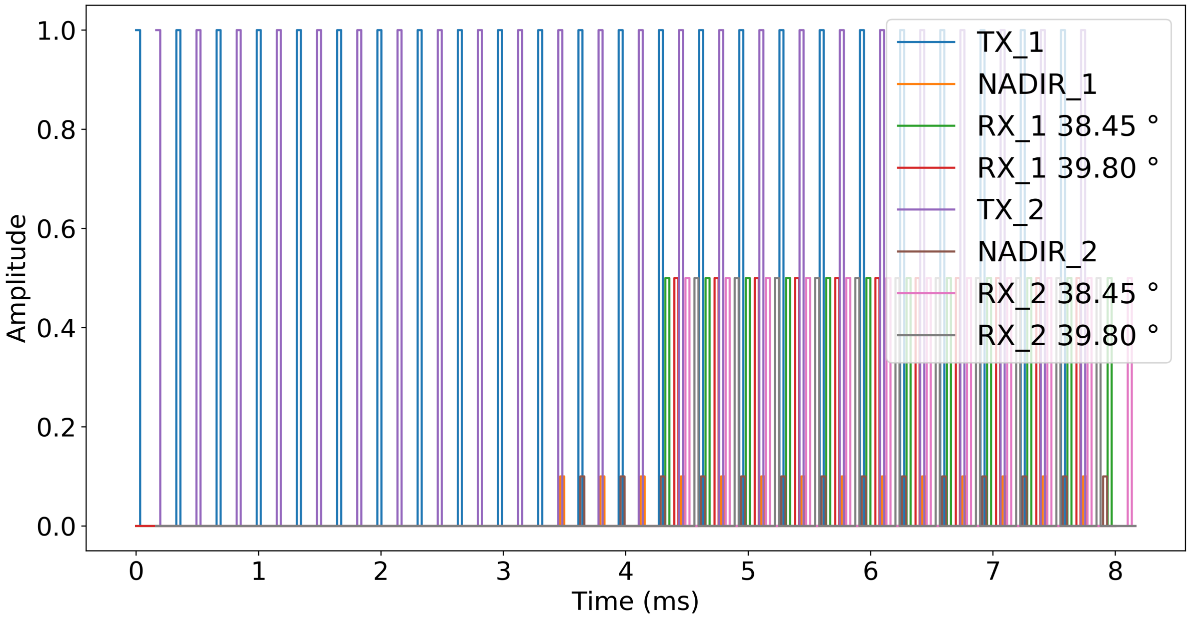

FIGURE 3.2 – Schematic of the signals in time of the acquisition over Queensland. The full PRF used was 6088.55 Hz and the satellite height 519 km.

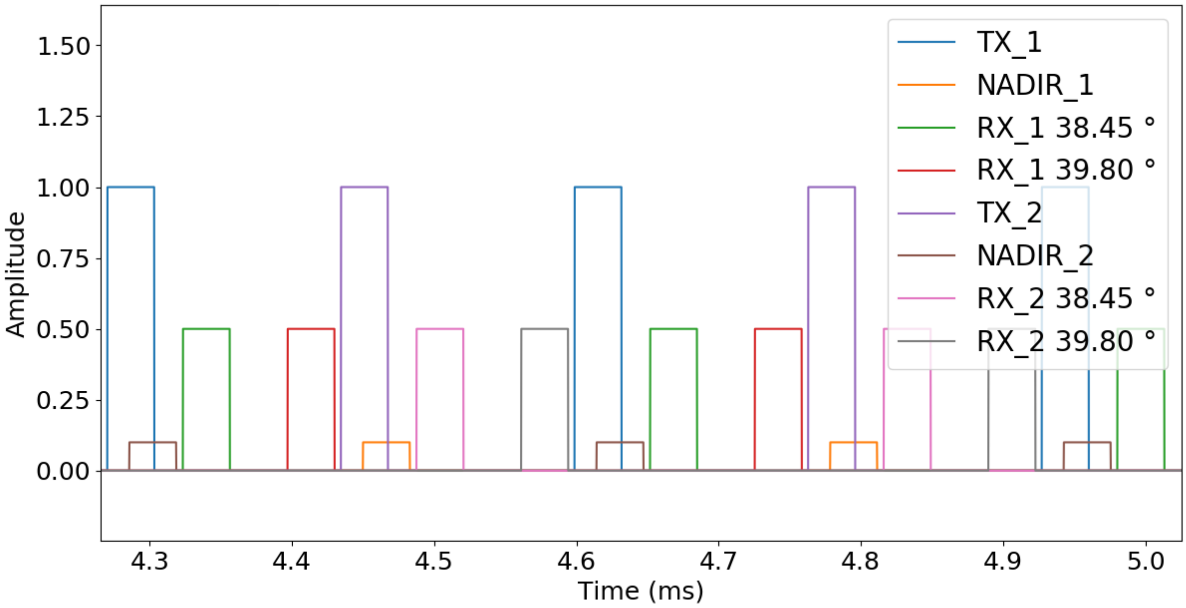

FIGURE 3.3 – Schematic of the signals in time zoomed in of the acquisition over Queensland. The full PRF used was 6088.55 Hz and the satellite height 519 km.

In the figures presented, the ‘Full PRF’ is defined as two times the PRF of each acquisition. Besides, the blue and purple lines represent the transmission pulses, while the green/red and pink/gray represent the reception of its respective mode. Important to notice that there is no interference and the signals arrive in valid timing positions using the full PRF of 6088.55 Hz. The near and far range incidence angles, 38.45 ° and 39.80 ° respectively, represent a scene of 15 km around the corner reflector.

After obtaining the available PRFs to perform the concurrent acquisition, the next step is to decide which one is the best in terms of ambiguities.

3.2 Ambiguity Assessment

The theoretical simplified approach to calculate RASR and AASR has already been described in Section 2.4. However, using the real satellite position and orientation, the procedure to calculate these parameters is slightly different.

3.2.1 RASR

The procedure to obtain the range ambiguity-to-signal ratio is fairly similar to the theoretical one. Once again, the points that are integer multiples of the pulse repetition interval in fast time from the target must be obtained. The main difference is that by using the real satellite data and the WGS 84 ellipsoid, it is possible to determine the ambiguous points on the Earth's surface more precisely. Appendix A describes the orbital mechanics used to relate the real satellite parameters with targets on the Earth's surface.

There are two main possibilities of which PRI should be used. First, if the antenna patterns are pointing at distinct directions in azimuth, then the PRF to obtain the RASR is given as half the full PRF, i.e., the own mode PRF. This is, however, an approximation due to the fact that there would be a high attenuation in both directions (azimuth and elevation). If both acquisitions are pointing at the same azimuth and elevation directions, then the adequate PRI is given by the inverse of the full PRF. In this case the signal of one mode is also interfering as an ambiguity with the reception of the other mode.

When performing Spotlight and Stripmap acquisitions with the same scene center, it is reasonable to consider the second case, i.e., the PRI being the inverse of the full PRF. This decision is justified by the fact that the squint angle of the Spotlight is not high enough to result in a high attenuation of the antenna gain in azimuth. Besides, for a short period of time, both acquisition modes are using the same azimuth antenna pattern. Figures 3.4 and 3.5 depict the RASR of a Spotlight and a Stripmap acquisition over the region of Queensland.

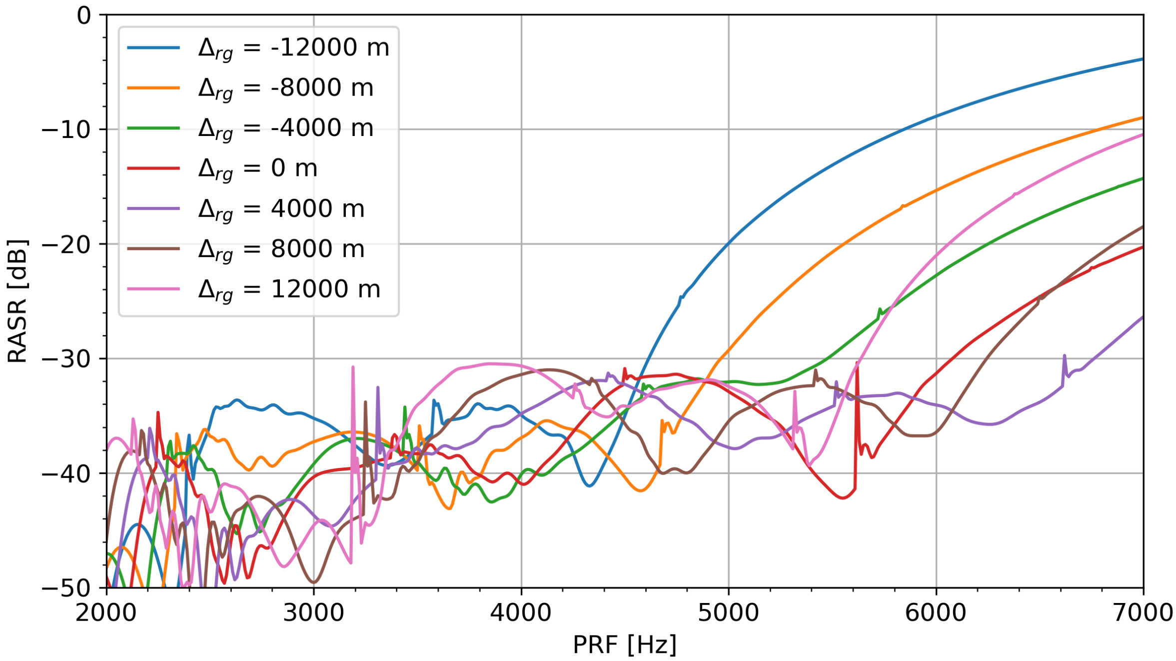

FIGURE 3.4 – RASR of the Stripmap acquisition over Queensland for targets at different range offsets from the scene center.

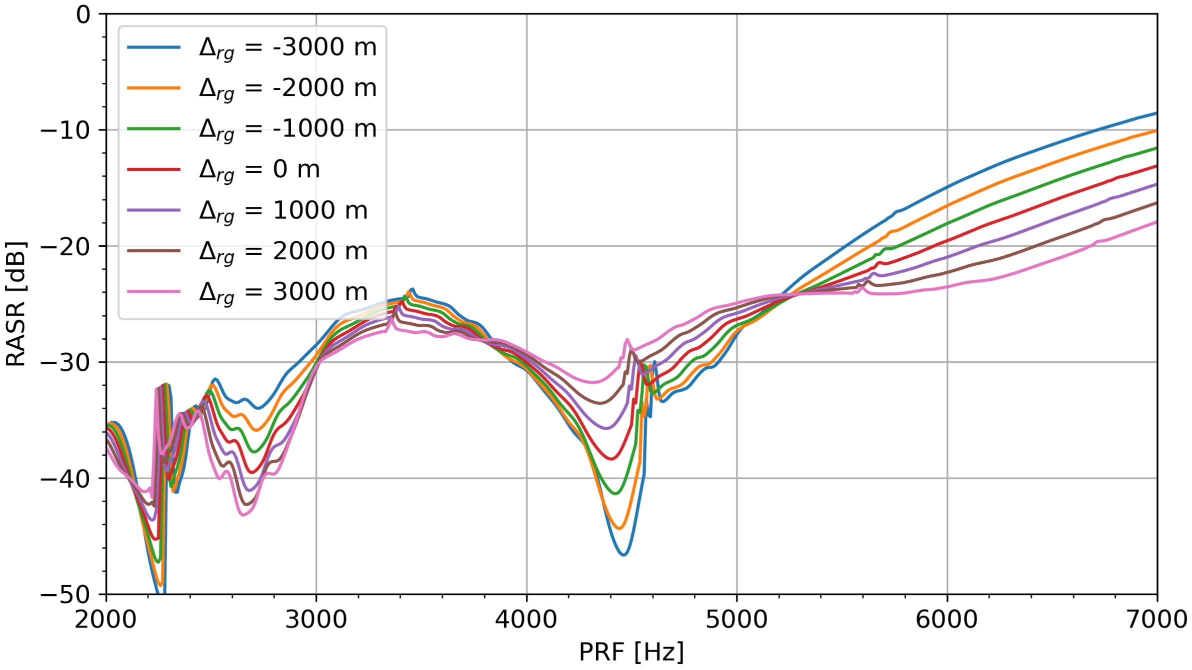

FIGURE 3.5 – RASR of the Spotlight acquisition over Queensland for targets at different range offsets from the scene center.

The behavior of the curves obtained depends mostly on the antenna pattern and the position of the ambiguities. As the antenna pattern is the real measurement of a sinc-like function and in the figures the PRF is being varied, the RASR curves are therefore very irregular and unsteady. However, ignoring these short period oscillations, the increase of the RASR when increasing the PRF is noticeable. This behavior is expected as the reduction of the PRI approximates the ambiguity points to the main lobe. Figures 3.6a and 3.6b show the target in blue and the ambiguity points in red for the bottom- and upper-end of the PRF scale.

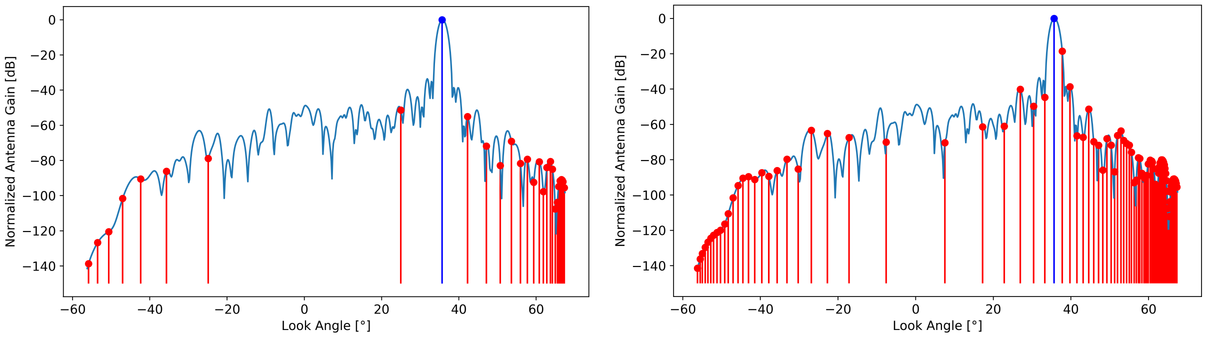

(a) PRF = 2000 Hz.

(b) PRF = 7000 Hz.

FIGURE 3.6 – Target and range ambiguity positions depicted in the antenna pattern for two different PRF values in the Stripmap acquisition.

3.2.2 AASR

The fundamentals behind obtaining the azimuth ambiguity-to-signal ratio theoretically and from the real acquisitions are the same. The first step is, once again, to obtain the Doppler shift of targets in azimuth. Instead of calculating from the derivative of the slant range, now it is possible to use the real satellite velocity relative to the target on Earth. The change in frequency as a result of the Doppler effect for stationary targets can be obtained by

$$\Delta f = \frac{2v_s^{\text{proj}}}{c - v_s^{\text{proj}}} f_0, \tag{3.1}$$

being c the speed of light, f_0 the center frequency of the chirp and v_s^{proj} the projection of the velocity of the satellite onto the vector connecting the satellite and the target.

Once the Doppler shift of a single target is known, the next step is to obtain the same result but to targets at different positions in azimuth. In other words, the antenna radiation pattern can be changed from azimuth angle to Doppler shift. This leads to an antenna gain as a function of the Doppler frequency. Knowing the target position and, consequently, its Doppler shift, the PRF will determine the position of the ambiguities.

In real Stripmap acquisitions, the AASR is calculated similarly as Equation (2.15). The main difference is the fact that now the discrete acquisitions are considered. Given the fact that each transmission and reception cycle takes one PRI and assuming that the acquisition of a target takes N cycles to occur, the AASR can be calculated by

$$\mathrm{AASR} = \frac{\sum\limits_{m \neq 0} \sum\limits_{n=1}^{N} P_r(f_o(n) + m f_p)}{\sum\limits_{n=1}^{N} P_r(f_o(n))}. \qquad (3.2)$$

In Equation 3.2, the sum in m acquires all the ambiguous points (red lines in Figure 3.7). $P_r(f)$ represents the power received from a point on Earth which Doppler shift is equal to f. $f_o(n)$ is the Doppler shift of the target when the satellite is at the n-th position and f_p is the pulse repetition frequency. Graphically, the AASR can be seen in a plot relating the antenna gain with the Doppler shift, as in Figure 3.7.

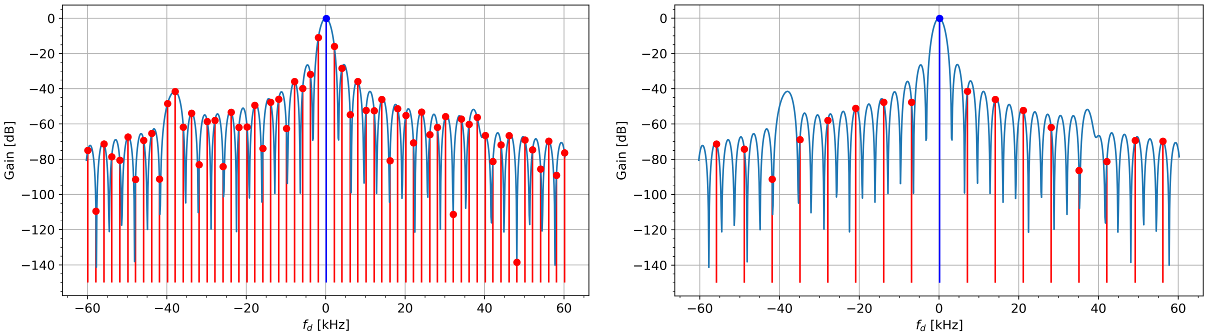

(a) PRF = 2000 Hz.

(b) PRF = 7000 Hz.

FIGURE 3.7 – Target and azimuth ambiguity positions depicted in the antenna pattern for two different PRF values using the Stripmap acquisition.

Figures 3.7a and 3.7b represent in blue the target position and in red the azimuth ambiguities at a fixed satellite position (at a specific n). Therefore, Equation (3.2) can be seen as the sum of all red lines divided by the sum of all blue lines throughout the whole acquisition. From the plots, it is clear that lower PRFs result in higher AASR. The total AASR of the Stripmap mode is depicted in Figure 3.8. The parameter $\alpha_{os,a}$ represents the azimuth oversampling factor, which defines the processed bandwidth.

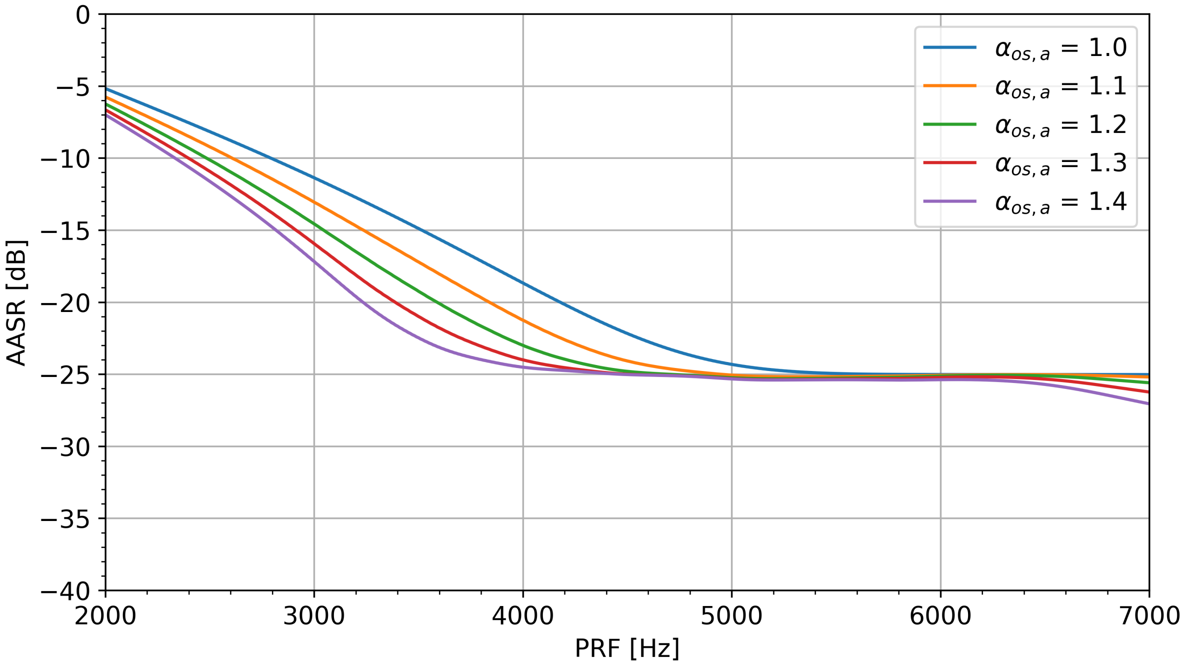

FIGURE 3.8 – AASR of the Stripmap acquisition over Queensland for different azimuth oversampling factors.

When analyzing AASR to Staring Spotlight acquisitions, one extra step is necessary. Due to the high steering angle and the consequent stronger sidelobes, the ambiguities are significantly higher at the extremities of the acquisition. In order to suppress the sidelobes and get reasonable AASR values, a weight function is applied along the integrated synthetic aperture. The AASR used in Staring Spotlight acquisitions is defined by

$$\mathrm{AASR} = \frac{\sum\limits_{m\neq 0}\sum\limits_{n=1}^{N} P_r(f_o(n)+mf_p)W^2(n)}{\sum\limits_{n=1}^{N} P_r(f_o(n))W^2(n)}. \tag{3.3}$$

The weight function W(n) is given by

$$W(n) = \alpha + (1-\alpha)\cos\left(\frac{\pi(2n-N-1)}{N-1}\right), n \in [1, N], \tag{3.4}$$

with $\alpha = 0.6$ and N the number of PRIs of the acquisition.

Once again, the AASR curve can be obtained simulating the acquisition over Queensland. The result is presented in Figure 3.9.

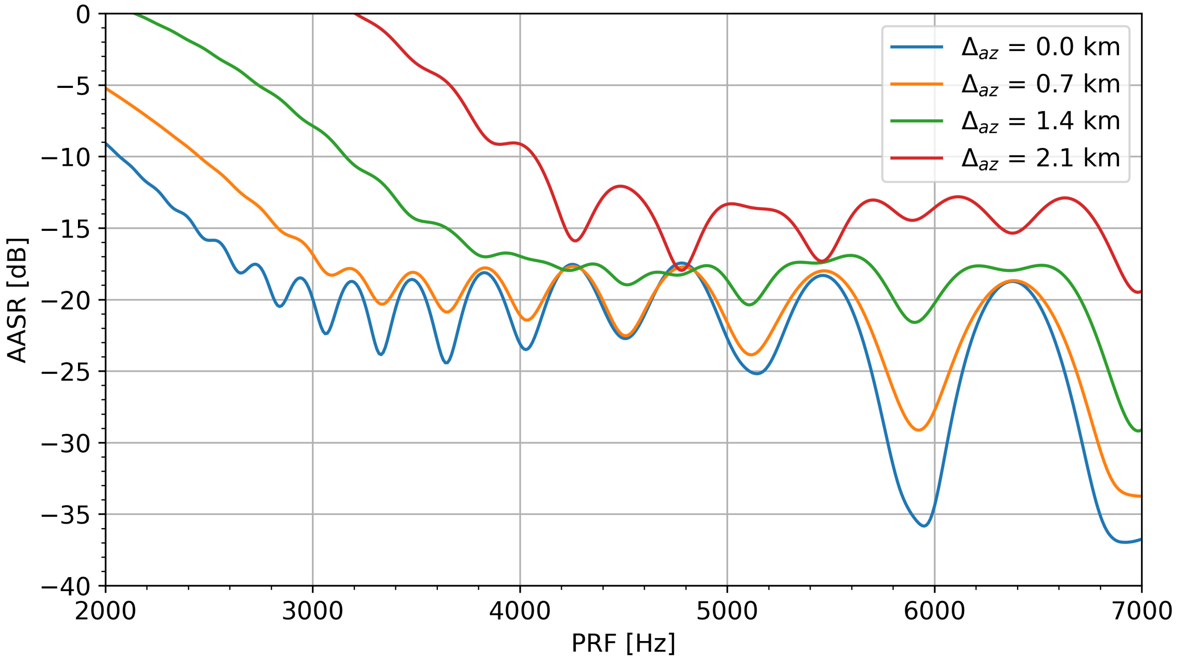

FIGURE 3.9 – AASR of the Spotlight acquisition over Queensland for targets at different azimuth offsets from the scene center. A Hamming window with $\alpha = 0.6$ was applied.

From Figure 3.9, it can be seen that when using low PRFs the scene size in azimuth gets quite limited due to strong azimuth ambiguities. The values Δ_{az} represent the distances between a point and the target center in the azimuth direction. As a matter of comparison, the result obtained can also be generated ignoring the weight function. This can be done simply using $\alpha_{os,a} = 1.0$. Figure 3.10 depicts this result. By comparing with Figure 3.9 it becomes clear how degraded the AASR gets when not suppressing the effects caused by the sidelobes in the extremities of the Staring Spotlight acquisition.

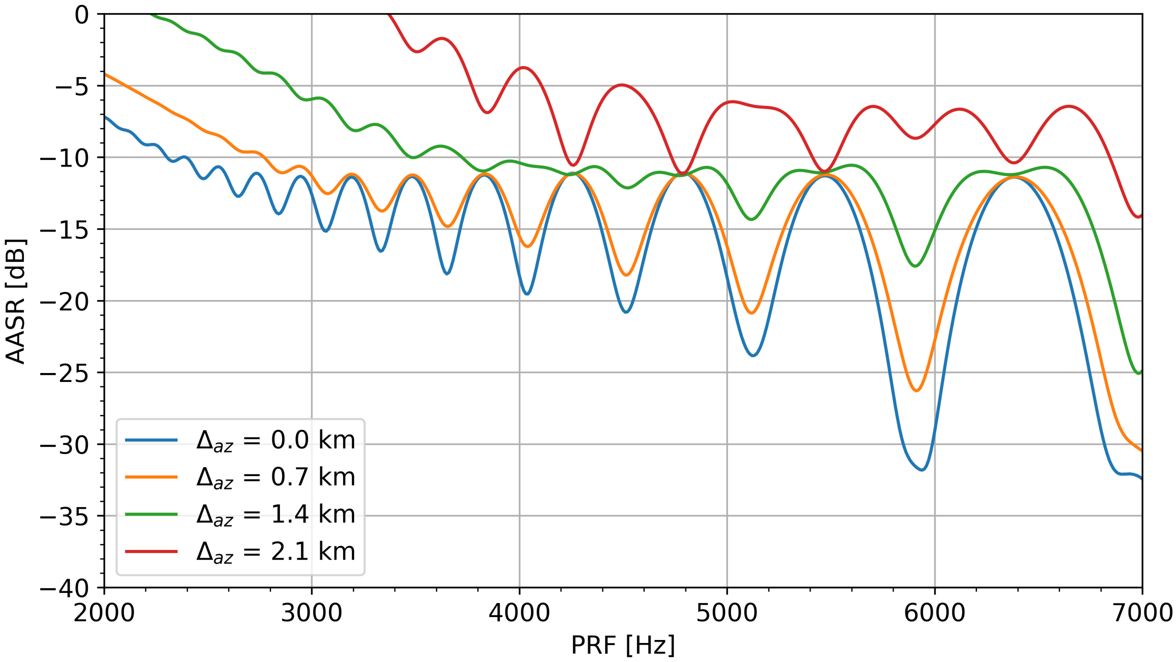

FIGURE 3.10 – AASR of the Spotlight acquisition over Queensland without weight function for targets at different azimuth offsets from the scene center.

Finally, it is important to know which PRF must be used in order to obtain the azimuth ambiguity correctly. As opposed to range ambiguities, in this case the adequate PRF is given by each mode frequency, i.e., half the full PRF. The reason for this is the fact that each mode will be separately processed and will generate a different image. In other words, as there are two acquisitions being performed, the effective rate in azimuth of each mode is given as half the PRF of the acquisition as a whole (full PRF). As an example, considering the acquisition depicted in Figure 3.3, it must be used PRF = 6088.55 Hz / 2 = 3044.275 Hz to analyze AASR. Important to notice that this result is different than the adequate PRF to analyze RASR, which is the full PRF.

From Figure 3.9, it can be observed a steep increase of the scene center AASR when using PRFs lower than 3000 Hz. Therefore, in order to avoid highly deteriorated acquisitions due to azimuth ambiguities, it was decided not to use PRFs lower than 2500 Hz. This leads to a minimum full PRF of 5000 Hz.

3.2.3 ASR

Finally, the last step when analyzing ambiguities is defining the parameter ASR (ambiguity-to-signal ratio), which is responsible for condensing both range and azimuth ambiguities into a single value. As previously described, the ASR is given as the sum of the ambiguities in the linear scale at a given PRF.

In the Stripmap mode analysis, the AASR was chosen to be the one with an oversampling factor of 1.1. This was the value chosen as it is, on average, commonly used when processing Stripmap acquisitions. However, it is important to notice that the oversampling factor is used in the post processing, i.e., after the acquisition of the raw data. Therefore, it can be changed after the acquisition as a trade-off between azimuth ambiguities and azimuth resolution. The RASR, on the other hand, was obtained as the mean of a symmetric scene of 24 km around the scene center. In Stripmap acquisitions the swath width is of high importance, the higher the better. From Figure 3.4, it is visible a high variability of the RASR at different range positions. Therefore, this importance and variability are being considered when taking the average of the RASR of a scene of 24 km. As a general rule, the desirable swath width of a Stripmap acquisition is between 15 km and 30 km, which motivated the 24 km scene.

The resulting ASR of the Stripmap acquisition is presented in Figure 3.11.

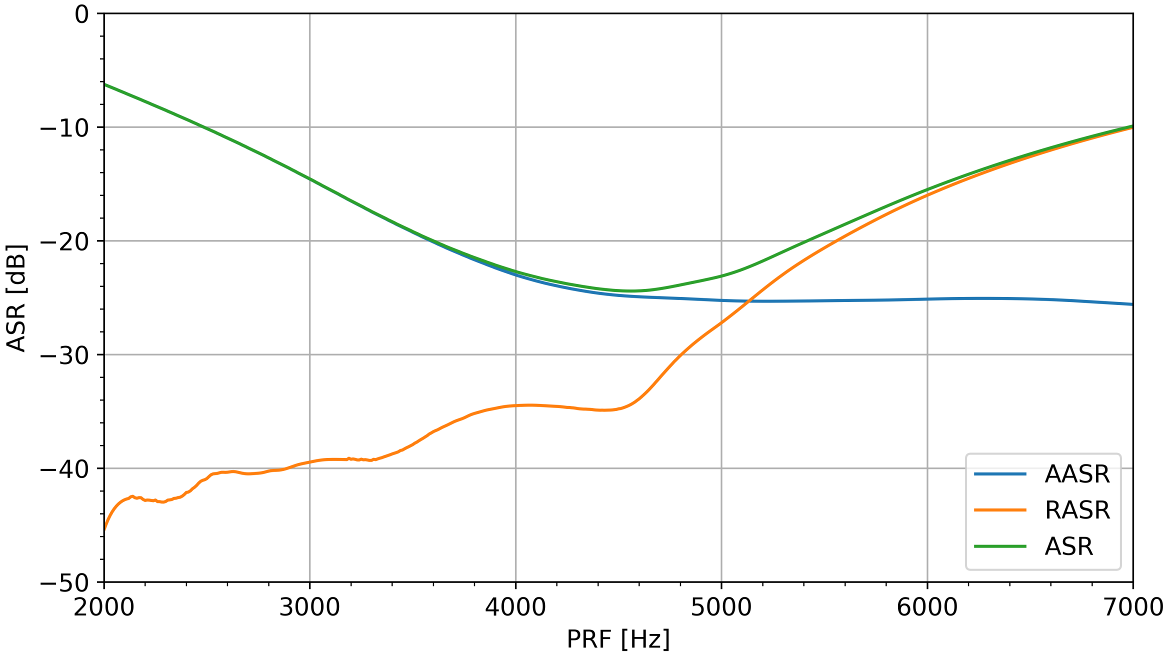

FIGURE 3.11 – ASR of the Spotlight acquisition over Queensland.

In Staring Spotlight acquisitions, however, the desired scene size in both azimuth and range are not very well defined. As a general rule, 4 km in ground range and 2 km in azimuth can be seen as the minimum requirements. In order not to assume any scene size, both RASR and AASR will be considered at the scene center. In the end, when obtaining the PRF, these parameters will be a matter of comparison. Therefore, the most important is to have a well defined and fixed definition of the ASR to each acquisition mode in order not to mix different definitions and perform an inappropriate analysis.

The resulting ASR of the Spotlight acquisition is presented in Figure 3.12.

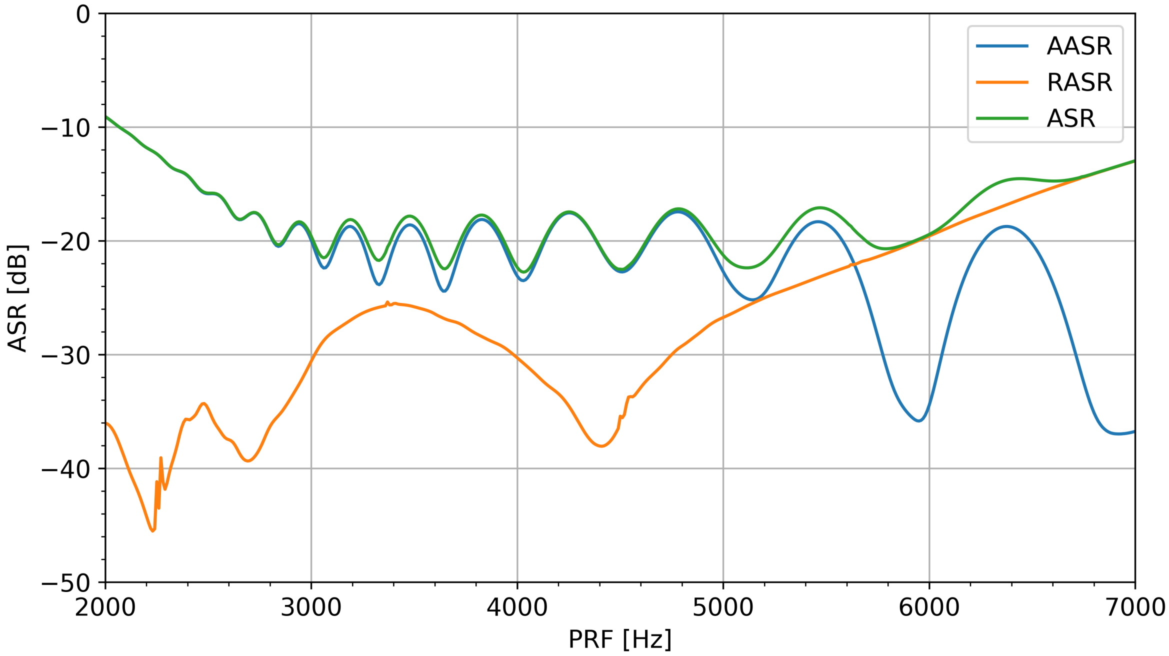

FIGURE 3.12 – ASR of the Spotlight acquisition over Queensland.

A problem when analyzing ambiguities is to know what the minimum acceptable ratios are. These minimum values depend both on the area being imaged and on the definition of RASR and AASR being used. Besides, it is not a trivial task to evaluate ambiguities of a real acquisition. From the definitions used in this work and the experience of DLR in evaluating the effect of ambiguities in real acquisitions, a target minimum ambiguity ratio is defined to be -17 dB, which means a minimum ASR of -14 dB. However, as the proposed concurrent mode is designed to operate at the limits of the satellite's capabilities, these ambiguity goals will not always be possible to achieve. In these cases, the feasibility of each individual acquisition must be analyzed.

Ultimately, there is another important point to be noticed about ambiguities. In the real acquisitions that were performed during the development of this thesis, each mode used an up or down chirp. This strategy prevents the range ambiguities of one mode to focus in the other one. By using different chirps, the image resolution and sidelobe ratios remain unchanged, but if there is a strong cross ambiguity, it will not be focused and its effect will be spread across multiple range lines.

3.3 PRF Selection

Finally, the most important parameter when performing a concurrent acquisition is the pulse repetition frequency (PRF). The previous timing and ambiguity analysis both had as final objective the selection of the PRF. In this chapter it will be described how these performance parameters are used to obtain the acquisition PRF.

First of all, it is important to notice that the timing analysis determine prohibitive values of PRF. The previous ambiguity analysis, however, merely defines performance parameters of how good the image will be in terms of ambiguities. Due to this fact, the first step of choosing the PRF is by taking a look at the timing diagram. As previously explained, Figure 3.1 puts together both Nadir and transmission interference. In order to use the timing diagram, a minimum swath width must be defined. Once again, by assuming a scene size in range of 15 km around the scene center, it is possible to obtain the minimum and maximum incidence angle of the acquisition. Then, it must be checked to which PRF values all incidence angle range fits inside a white region. This procedure may not provide any possible PRF, but may also return intervals of available PRFs. The former situation usually happens when dealing with high incidence angles or long swath widths.

Knowing which PRF intervals are initially available, it must then be checked the number of traveling pulses. In other words, the Stripmap echo must reach the antenna right after a Stripmap transmission pulse. Supposing that there are still some PRF intervals available after this selection, the last step of finding possible PRFs is checking the satellite capability, which is given by a list of possible PRFs it can operate. Those PRFs which attend the satellite capability are those that would result in a valid acquisition from a timing point of view.

However, not necessarily all these PRFs will result in images of acceptable quality. To select the best image, the ambiguities and the scene size of each acquisition must be analyzed. Assuming, in the first place, that the Spotlight acquisition will be inside the Stripmap range, only the Stripmap swath width is necessary. Once again using the timing diagram, but this time at a fixed PRF, the maximum incidence angle range of each PRF is obtained and, with this result, the maximum range size of the image is acquired. Besides, each PRF will also result in a value of RASR, AASR and ASR of each acquisition.

Due to all timing restrictions, in the end it is unlikely to obtain a high number of available PRFs. Combining this small number of possibilities with the uniqueness of the concurrent imaging mode, the final PRF selection is, for now, done individually for each acquisition. On the one hand, some acquisitions are highly sensible to ambiguities, as an example those near lakes, rivers, ocean or calm water areas in general. On the other hand, some other acquisitions have a very strict requirement of a large swath width. Therefore, the decision between different PRFs at this point really depends on what is being imaged and the requirements of the client.

As an example of the discussion above, the available PRFs and the performance of each mode to the acquisition over Queensland can be determined. The results of each mode are presented in Tables 3.1, 3.2 and 3.3.

TABLE 3.1 – Stripmap performance of the acquisition over Queensland.

PRF	**AASR**	**RASR**	**ASR**	**Scene Size**
5163.82 Hz	-13.80 dB	-17.32 dB	-12.20 dB	27.58 dB
6067.03 Hz	-19.00 dB	-8.34 dB	-7.98 dB	23.08 dB
6077.77 Hz	-19.05 dB	-8.27 dB	-7.92 dB	23.10 dB
6088.55 Hz	-19.12 dB	-8.20 dB	-7.86 dB	23.14 dB

TABLE 3.2 – Spotlight performance of the acquisition over Queensland.

PRF	**AASR**	**RASR**	**ASR**
5163.82 Hz	-16.58 dB	-24.52 dB	-15.93 dB
6067.03 Hz	-21.61 dB	-14.22 dB	-13.49 dB
6077.77 Hz	-21.84 dB	-14.13 dB	-13.45 dB
6088.55 Hz	-22.04 dB	-14.04 dB	-13.40 dB

TABLE 3.3 – Spotlight AASR performance of the acquisition over Queensland at different azimuth positions.

PRF	**AASR (Δ_{az} = 0km)**	**AASR (Δ_{az} = 1.4km)**	**AASR (Δ_{az} = 2.1km)**
5163.82 Hz	-16.58 dB	-3.44 dB	4.91 dB
6067.03 Hz	-21.61 dB	-8.16 dB	1.76 dB
6077.77 Hz	-21.84 dB	-8.21 dB	1.72 dB
6088.55 Hz	-22.04 dB	-8.27 dB	1.67 dB

From the performance ambiguity plots, mainly from Figure 3.9, it can be seen that one of the most strict constraints is the azimuth ambiguity in the Spotlight acquisition. The image shows that very low PRFs result in high AASR values, which strongly limits the azimuth scene size of the Staring Spotlight acquisition. Therefore, due to this observation, it was decided to use 6088.55 Hz to perform an experimental acquisition. Even though the Stripmap mode AASR was not better than -17 dB, if the image gets degraded by strong ambiguities, the solution would be simply to reprocess the raw data with a higher azimuth oversampling factor (lower bandwidth). Obviously, this solution is not optimum as it leads to a trade-off between azimuth ambiguity and resolution. Further studies in terms of improving ambiguities are intended to take place in the Master Thesis.

4 Concurrent Imaging Evaluation

In the previous chapter, the design of the concurrent imaging mode was described. This design shall now be evaluated and its performance derived. Therefore, three different acquisitions were performed, one experimental concurrent imaging and two reference acquisitions. So as to keep the imaging parameters uniform across the acquisitions, the imaging of a same area is spaced by eleven days, due to the revisit period of the satellite. In other words, to acquire both Stripmap and Spotlight reference acquisitions, eleven days of wait are necessary due to the repeat cycle of the orbit. With the results from both the experimental and the reference acquisitions, the comparison between them enables determining if the new mode is capable of achieving the desired performance in terms of resolution and sidelobe ratios. It is important to notice that a corner reflector must be within the scenes in order to be able to do this comparison.

The evaluation of resolution and sidelobe ratios both in range and in azimuth is done by a point target analysis. The first step is to identify the corner reflector in the scene. This can be done by looking for the point of maximum intensity in the focused image and then comparing it with the expected geographical position. After identifying the corner reflector, a cut in azimuth and range is done. As the SAR principle exhibits an approximate separability in range and azimuth, often only the 1-D cuts in range and azimuth are used to characterize the 2-D impulse response function (IRF). It is important to note that in SAR systems the impulse response is obtained by measuring the system response to a single and isolated scatterer on the ground (Cumming; Wong, 2005). Corner reflectors are designed to reflect the incoming wave, reversing its orientation regardless of the direction of arrival. Therefore, due to their geometry and behavior, corner reflectors behave as a single strong scatterer and are used to assess the IRF of the system.

Given that the acquired data is originally complex, the data must be first transformed into intensity by calculating the square of its absolute value. Besides, an interpolation (oversampling) of the image is necessary in order to get more refined and precise results. In this case, a zero-padding interpolation was applied to each of the original complex-valued cuts.

Depending on the application, the desired parameters can be defined in different ways.

In this analysis, spatial resolution δ_{az} and δ_{rg} are defined as the distance in meters between the -3 dB points with respect to the peak of the main lobe of the IRF in azimuth and range direction, respectively. A better (lower) value is desirable as the spatial resolution of an imaging system is a measure of its ability to distinguish between adjacent targets.

Moreover, the peak-to-sidelobe ratio (PSLR) is defined as the ratio of the peak intensity of the main lobe I_{peak} to the peak intensity of the most intense sidelobe I_{side}. In this case, a higher value is desired as the PSLR is the worst case measure of the SAR ability to identify a weak target from a nearby strong target. It can be obtained from

$$\mathrm{PSLR} = 10\log_{10}\left(\frac{I_{\mathrm{peak}}}{I_{\mathrm{side}}}\right) = I_{\mathrm{peak\_dB}} - I_{\mathrm{side\_dB}}. \tag{4.1}$$

Finally, the integrated sidelobe ratio (ISLR) is defined as the ratio of the energy of the main lobe E_{main} to the energy of the sidelobes E_{side}. In this case, the main lobe is considered as the region centered on the IRF peak with a width of twice the spatial resolution. Differently, the sidelobe region is defined as the region centered on the IRF peak with a width of twenty times the spatial resolution, but excluding the main lobe region just defined. Once again it is desired to obtain a higher ISLR value, as it characterizes the ability to detect weak targets in the vicinity of bright targets. It can be obtained from

$$\mathrm{ISLR} = 10\log_{10}\left(\frac{E_{\mathrm{main}}}{E_{\mathrm{side}}}\right). \tag{4.2}$$

In summary, the analysis of a corner reflector in the focused image returns not only resolution, but also PSLR and ISLR in range and azimuth. Some digital signal processing (DSP) techniques can be applied during processing to change the balance between these parameters. As an example, a window function can be applied during compression to improve sidelobe ratios and ambiguities while deteriorating resolution. In every acquisition performed in this work a generalized Hamming window ($\alpha = 0.6$) was applied both in range and azimuth. As a result, there is a deterioration of approximately 18% in resolution, but at the same time an improvement in PSLR, ISLR and AASR.

4.1 Experimental Concurrent Imaging Acquisition

In the first experimental acquisition, the selected target is a corner reflector in Surat Basin, Queensland, Australia located at latitude -27.02392492° and longitude 150.57682628°. The PRF of the acquisition was chosen to be 6088.55 Hz based on the previous timing and ambiguity analyses. The satellite position resulted in an incidence angle of 39°.

4.1.1 Stripmap Concurrent Imaging Acquisition

In short, as described in Chapter 3, a concurrent imaging mode acquisition is done by interleaving Stripmap and Spotlight pulses. Therefore, as a matter of simplicity, the pulse characteristics chosen to be used in this experiment were the same as the ones used for operational TerraSAR-X acquisitions. The Stripmap mode uses a linear chirp with a bandwidth of 100 MHz, whereas the Staring Spotlight mode uses the same chirp but with a higher bandwidth of 300 MHz. For the concurrent imaging mode, however, different chirps are used in order to reduce the cross-interference. Therefore, the Stripmap pulses of the experimental acquisition uses an up-chirp and the Spotlight ones a down-chirp. By doing so, the cross-interference will be smeared as echoes from one mode will not be properly focused on the image of the other mode.

After processing, the first experimental acquisition resulted in the two desired images. First, the Stripmap image is shown in Fig. 4.1.

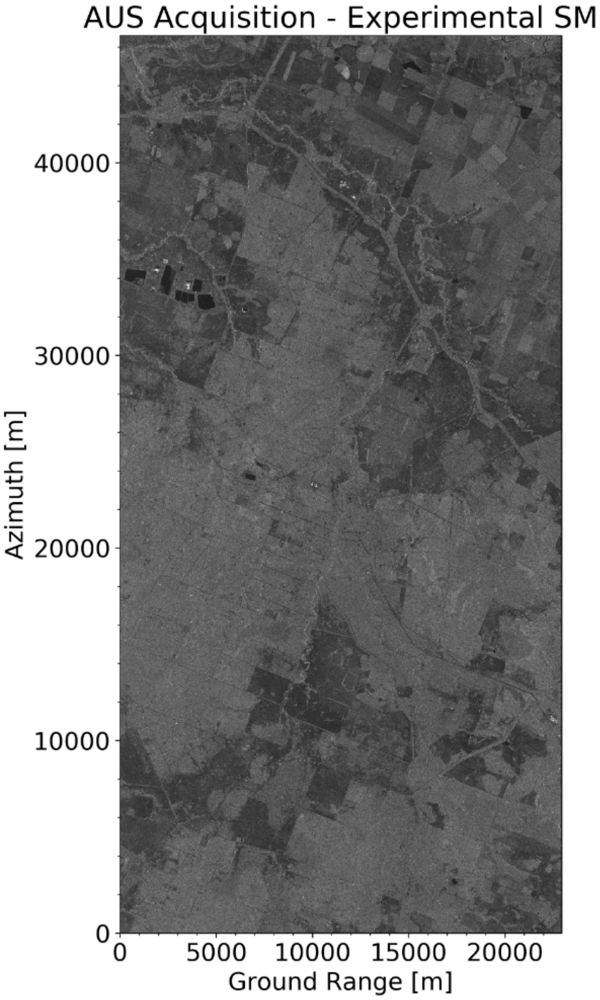

FIGURE 4.1 – Focused image of the experimental Stripmap acquisition over Queensland.

Even though the image obtained is visually reasonable and comparable with what is expected from a successful SAR acquisition, an impulse response analysis is still necessary as only visual inspection is not enough to determine resolution and sidelobe performance. The point target analysis of the corner reflector in the Stripmap image resulted in the azimuth and range cuts shown in Fig. 4.2.

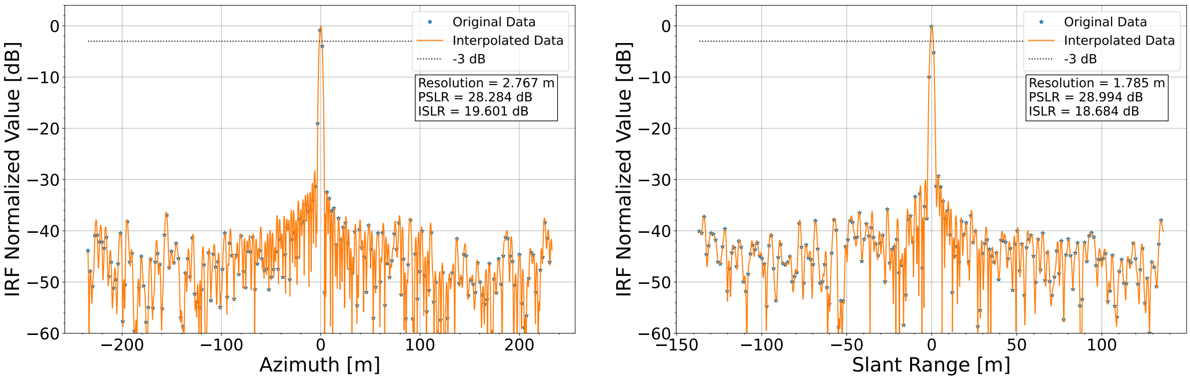

(a) Cut in azimuth.

(b) Cut in range.

FIGURE 4.2 – Impulse responses from a corner reflector in the Stripmap scene of the experimental concurrent mode acquisition.

In order to evaluate if the resolution and the sidelobe ratio parameters are according to what is expected, a theoretical prediction is performed. The azimuth and range resolutions can be estimated theoretically, according to (Cumming; Wong, 2005), by

$$\delta_{\mathrm{az,SM}} = \frac{v_{\mathrm{g}}\gamma_w}{\Delta f_{\mathrm{d}}} = \frac{7114.0 \text{ m/s} \cdot 1.179}{3044.27 \text{ Hz}} = 2.755 \text{ m and} \tag{4.3}$$

$$\delta_{\mathrm{rg,SM}} = \frac{c_0\gamma_w}{2B_r} = \frac{3 \cdot 10^8 \text{ m/s} \cdot 1.179}{2 \cdot 100 \cdot 10^6 \text{ Hz}} = 1.767 \text{ m}, \tag{4.4}$$

where γ_w represents the broadening factor of the window applied, v_{g} the satellite ground speed, Δf_{d} the processed Doppler bandwidth, c_0 the speed of light and B_r the signal bandwidth.

The resolutions obtained in the Stripmap acquisition of the concurrent mode – $\delta_{\mathrm{az}} = 2.767$ m and $\delta_{\mathrm{rg}} = 1.785$ m – match quite well the expected theoretically ones, with an absolute error of less than 2 centimeters and relative of 1%. Moreover, PSLR and ISLR – $\mathrm{PSLR}_{\mathrm{az}} = 28.3$ dB, $\mathrm{PSLR}_{\mathrm{rg}} = 29.0$ dB, $\mathrm{ISLR}_{\mathrm{az}} = 19.6$ dB and $\mathrm{ISLR}_{\mathrm{rg}} = 18.7$ dB – are well within the TerraSAR-X mission specification (Fritz; Eineder, 2013), which are 25 dB for the PSLR and 18 dB for the ISLR of a Stripmap acquisition.

4.1.2 Spotlight Concurrent Imaging Acquisition

The Spotlight image obtained is also visually satisfactory and according to the expectations. The focused image is shown in Fig. 4.3.

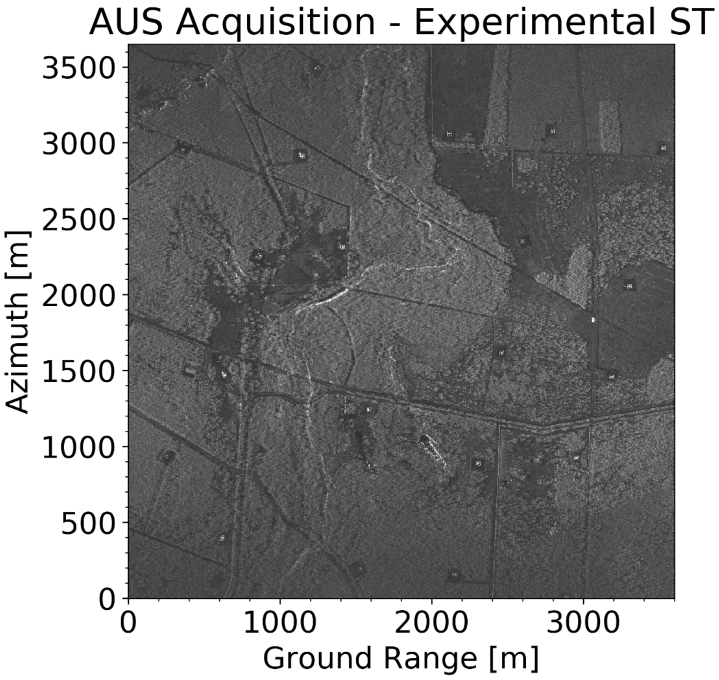

FIGURE 4.3 – Focused image of the experimental Staring Spotlight acquisition over Queensland.

The same corner reflector that was used to perform the point target analysis in the Stripmap image was acquired by the Spotlight acquisition. The same analysis was carried out and the results are shown in Fig. 4.4.

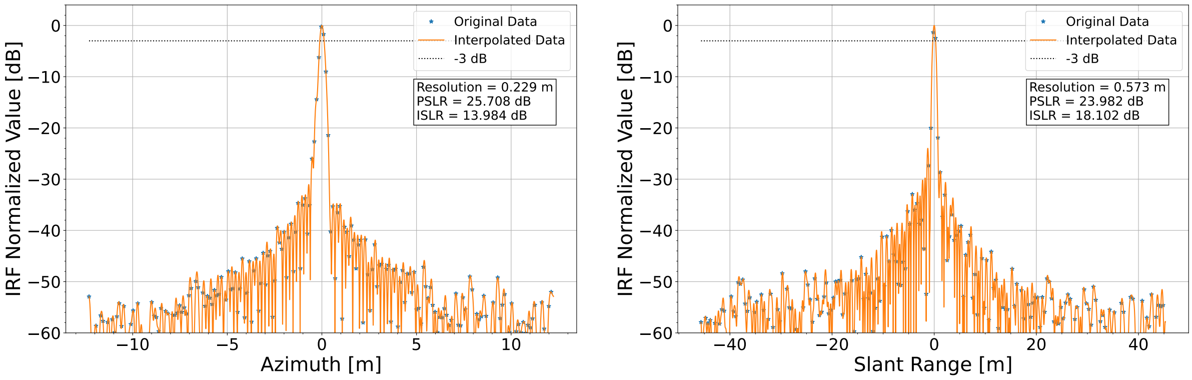

(a) Cut in azimuth.

(b) Cut in range.

FIGURE 4.4 – Impulse responses from a corner reflector in the Staring Spotlight scene of the experimental concurrent mode acquisition.

Another theoretical analysis is necessary in order to validate the results obtained.

According to (Mittermayer *et al.*, 2014) and (Cumming; Wong, 2005), the azimuth and range resolutions of a Staring Spotlight acquisition are given, respectively, by

$$\delta_{\mathrm{az,ST}} = \frac{\lambda v_{\mathrm{g}} \gamma_w}{2 v_{\mathrm{s}} \Delta\theta_{span}} \approx \frac{0.03106 \text{ m} \cdot 7114.0 \text{ m/s} \cdot 1.179}{7680.0 \text{ m/s} \cdot 0.07766 \text{ rad}} = 0.218 \text{ m and} \tag{4.5}$$

$$\delta_{\mathrm{rg,ST}} = \frac{c_0 \gamma_w}{2 B_r} \approx \frac{3 \cdot 10^8 \text{ m/s} \cdot 1.179}{2 \cdot 300 \cdot 10^6 \text{ Hz}} = 0.589 \text{ m}, \tag{4.6}$$

where λ represents the signal wavelength, v_{s} the satellite speed and $\Delta\theta_{span}$ the total steering azimuth angle that is swept during the acquisition.

Table 4.1 summarizes the parameters obtained and expected from the point target analysis for this concurrent mode experiment. The resolutions in the Staring Spotlight acquisition of the concurrent mode – $\delta_{\mathrm{az}} = 0.229$ m and $\delta_{\mathrm{rg}} = 0.573$ m – match quite well the ones expected theoretically, with an absolute error of less than 2 centimeters and relative of 5%. The specified minimum PSLRs are 20 dB and 25 dB for azimuth and range respectively, whereas the minimum ISLRs are 16 dB and 18 dB. Therefore, the range PSLR – $\mathrm{PSLR}_{\mathrm{rg}} = 24.0$ dB – obtained is 1 dB off and the azimuth ISLR – $\mathrm{ISLR}_{\mathrm{az}} = 14.0$ dB – is 2 dB off-specification (Fritz; Eineder, 2013). The other parameters – $\mathrm{PSLR}_{\mathrm{az}} = 25.7$ dB and $\mathrm{ISLR}_{\mathrm{rg}} = 18.1$ dB – are within the specified range. These small deviations are not a huge concern not only because 1 or 2 dB is not enough to deteriorate the quality of the image, but also due to fact that the concurrent mode processing is still in preliminary phase. With further development of the proposed mode, the processing is expected to be improved in order to correct this sort of issue.

TABLE 4.1 – Summary of the first experimental SM/ST concurrent mode acquisition over Australia and its comparison with the expected results or the specifications.

Parameter		**Staring Spotlight**	**Expected**	**Stripmap**	**Expected**
Resolution	**Azimuth**	0.229 m	0.218 m	2.767 m	2.755 m
	Slant Range	0.573 m	0.589 m	1.785 m	1.767 m
Scene Size	**Azimuth**	3.65 km	x	46.59 km	x
	Ground Range	3.60 km	x	22.94 km	23.14 km
		Staring Spotlight	**Specification**	**Stripmap**	**Specification**
PSLR	**Azimuth**	25.7 dB	20.0 dB	28.3 dB	25.0 dB
	Slant Range	24.0 dB	25.0 dB	29.0 dB	25.0 dB
ISLR	**Azimuth**	14.0 dB	16.0 dB	19.6 dB	18.0 dB
	Slant Range	18.1 dB	18.0 dB	18.7 dB	18.0 dB

The terms in the table which are represented by a ‘x’ are those which no expected value was predicted. These parameters depend on external factors which are not under analysis in this work.

The results of this first concurrent acquisition are quite satisfactory and the experiment can be seen as successful. This first acquisition was highly important to confirm whether the idea of a ST/SM concurrent imaging mode was really feasible and would return reasonable results. Besides, the experiment also brought to light the fact that specific work must be done in terms of processing a concurrent mode acquisition in order to correct some impulse response anomalies, specially seen in the Staring Spotlight point target analysis.

Finally, the idea of replacing two reference acquisitions, which take 11 days to be performed, by only one concurrent mode is promising, but deserves further analysis. Therefore, two reference acquisitions were ordered. Comparing these reference images with the concurrent mode ones allows to conclude, or at least have some clues, on the real world usage of the proposed mode. The following sections will present the reference acquisitions and some discussion comparing them with the concurrent mode results obtained in this section.

4.2 Reference Acquisition

The motivation for the reference acquisitions is to create the gold standard (state-of-the-art) images to which the concurrent mode results shall be compared. From an optimistic perspective, in case the concurrent mode results are similar, or at least relatively close, to the reference ones, then it would indicate that the new mode has potential to become an useful tool and, therefore, it is worth investing more time and resources in it. However, this comparison may also end up showing strong weakness and intrinsic problems of the concurrent mode, which would make one to rethink its value and possibly discontinue the development. The objective of this section is to explain and obtain the reference acquisitions.

The concurrent mode experiment returned one Staring Spotlight and one Stripmap image of a given region in Australia. In order to keep the same conditions, reference acquisitions of the same modes were ordered over the same region at the same incidence angle. By doing so, the same corner reflectors with fixed alignments can be analyzed in order to assess the image performance parameters of interest. The inputs of the reference acquisitions are only the target on Earth, the satellite position (incidence angle) and the desired mode. The PRF is chosen automatically by the radar parameter generated tool which is used by DLR to maximize the image quality.

4.2.1 Stripmap Acquisition

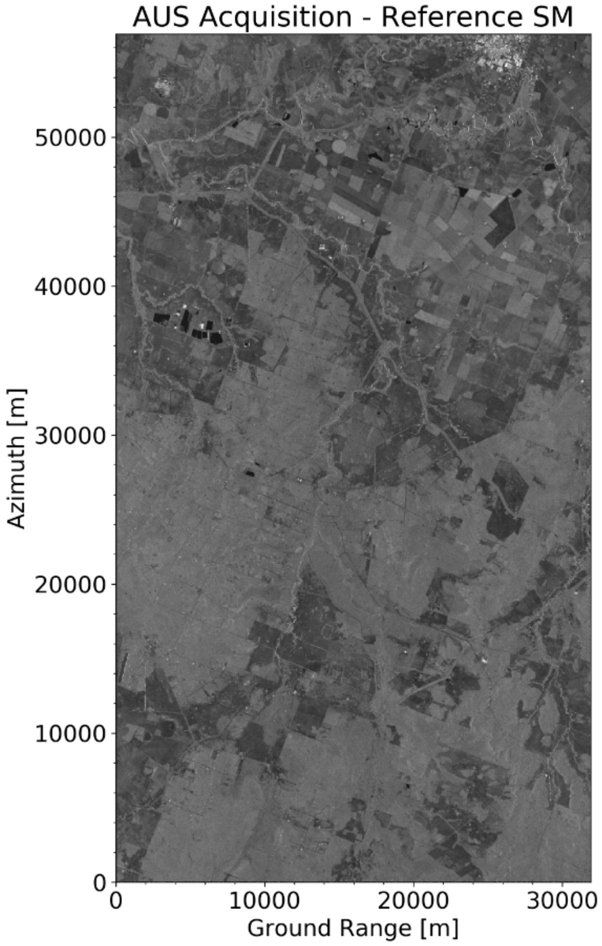

FIGURE 4.5 – Focused image of the reference Stripmap acquisition over Queensland.

Once again, an impulse response analysis is necessary as only visual inspection is not enough to determine resolution and sidelobe performance. The point target analysis of the corner reflector in the Stripmap image resulted in the azimuth and range cuts shown in Fig. 4.6.

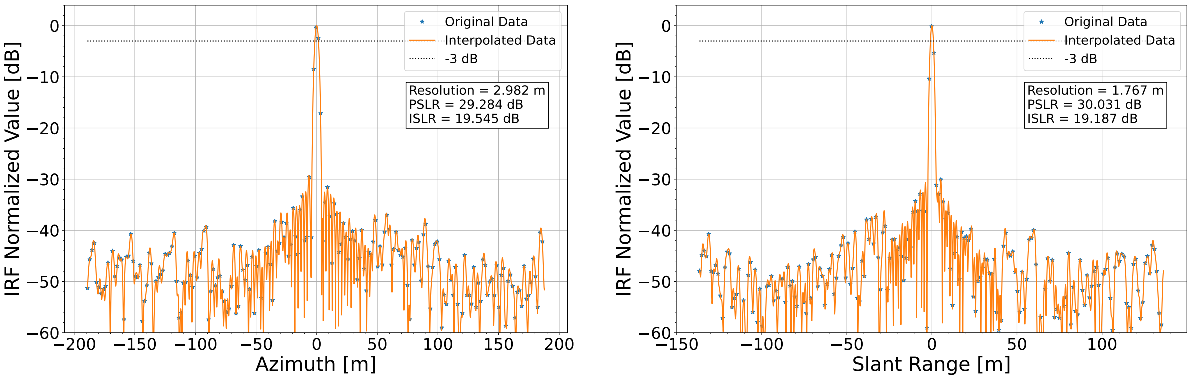

(a) Cut in azimuth.

(b) Cut in range.

FIGURE 4.6 – Impulse responses from a corner reflector in the Stripmap scene of the reference acquisition.

The reference Stripmap acquisition uses an processed azimuth bandwidth of 2765 Hz, different than the 3044 Hz used in the experimental processing. Therefore, the expected azimuth resolution can be recalculated by

$$\delta_{\mathrm{az,SM}} = \frac{v_{\mathrm{g}}\gamma_w}{\Delta f_d} \approx \frac{7114.0\ \mathrm{m/s} \cdot 1.179}{2765\ \mathrm{Hz}} = 3.033\ \mathrm{m}. \tag{4.7}$$

As expected from a reference acquisition, all the parameters of interest are respecting the specifications.

4.2.2 Staring Spotlight Acquisition

The Spotlight image obtained is once again visually satisfactory and according to the expectations. The focused image is shown in Fig. 4.7.

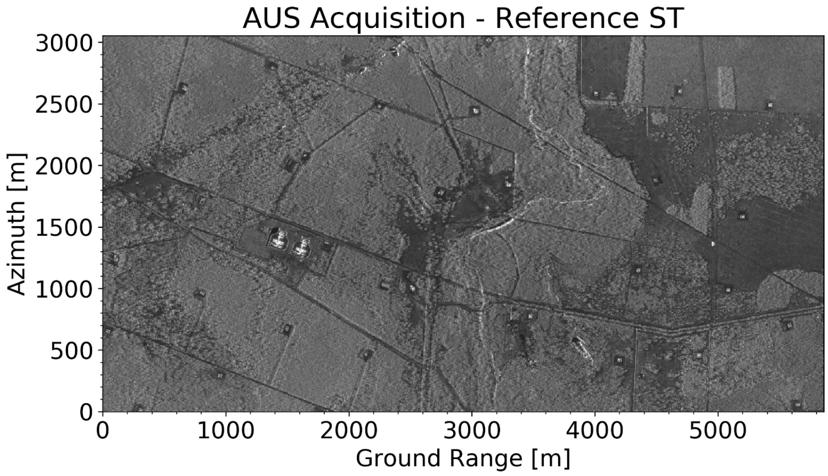

FIGURE 4.7 – Focused image of the reference Staring Spotlight acquisition over Queensland.

The same corner reflector that was used to perform the point target analysis in the Stripmap image was acquired by the Spotlight acquisition. The analysis was carried out and the results are shown in Fig. 4.8.

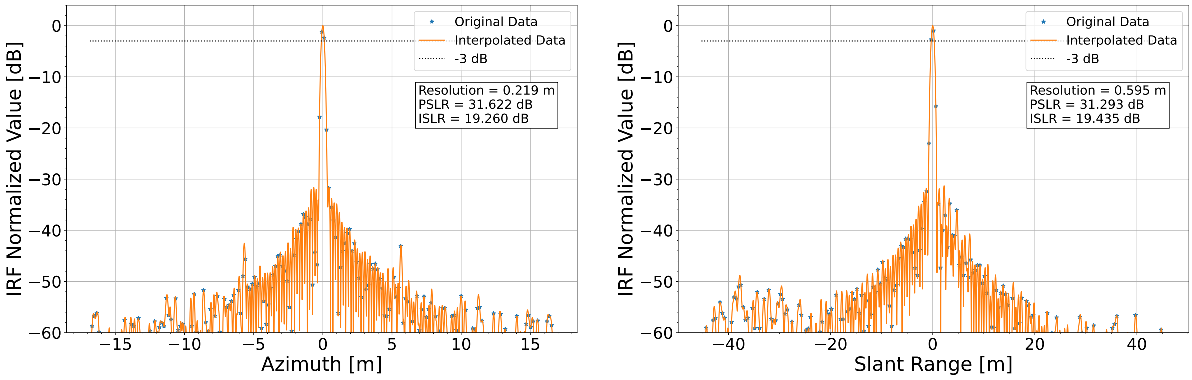

(a) Cut in azimuth.

(b) Cut in range.

FIGURE 4.8 – Impulse responses from a corner reflector in the Staring Spotlight scene of the reference acquisition.

All the parameters of interest in the reference Staring Spotlight acquisition are once again respecting the specifications. The results obtained from the reference acquisitions are summarized in the Table 4.2.

TABLE 4.2 – Summary of the reference acquisitions over Australia and their comparison with the specifications.

Parameter		Staring Spotlight	Specification	Stripmap	Specification
Resolution	**Azimuth**	0.219 m	0.240 m	2.982 m	3.000 m
	Slant Range	0.595 m	0.600 m	1.767 m	1.800 m
Scene Size	**Azimuth**	3.05 km	2.50 - 2.80 km	56.91 km	50.00 km
	Ground Range	5.86 km	4.60 - 7.50 km	31.92 km	30.00 km
PSLR	**Azimuth**	31.6 dB	20.0 dB	29.3 dB	25.0 dB
	Slant Range	31.3 dB	25.0 dB	30.0 dB	25.0 dB
ISLR	**Azimuth**	19.3 dB	16.0 dB	19.5 dB	18.0 dB
	Slant Range	19.4 dB	18.0 dB	19.2 dB	18.0 dB

4.3 Discussions - Reference vs. Experimental

According to the initial objective of comparing the concurrent imaging mode with the reference acquisitions, a side by side comparison of the results is presented in Table 4.3.

TABLE 4.3 – Comparison between the first experimental SM/ST concurrent mode acquisition over Australia and the reference ones.

		Staring Spotlight		Stripmap	
Parameter		Concurrent	Reference	Concurrent	Reference
Resolution	**Azimuth**	0.229 m	0.219 m	2.767 m	2.982 m
	Slant Range	0.573 m	0.595 m	1.785 m	1.767 m
Scene Size	**Azimuth**	3.65 km	3.05 km	46.59 km	56.91 km
	Ground Range	3.60 km	5.86 km	22.94 km	31.92 km
PSLR	**Azimuth**	25.7 dB	31.6 dB	28.3 dB	29.3 dB
	Slant Range	24.0 dB	31.3 dB	29.0 dB	30.0 dB
ISLR	**Azimuth**	14.0 dB	19.3 dB	19.6 dB	19.5 dB
	Slant Range	18.1 dB	19.4 dB	18.7 dB	19.2 dB

A side by side comparison enables a more comprehensive and meaningful analysis of the results obtained. For instance, it is clear that the concurrent mode has similar capabilities in terms of resolution both in azimuth and range. However, there is a clear reduction in ground range scene size in both of the experimental images. Besides, due to the concurrent mode processing tool being in an early stage, a deterioration in the sidelobe parameters in the experimental Staring Spotlight image is also present.

On the one hand, the reduction in the swath width of the experimental Stripmap image results from the use of a higher PRF in the concurrent mode, which is necessary to acquire both images with sufficient azimuth bandwidth and reasonable ambiguity performance. The high PRF implies a lower PRI and, therefore, tighter timings. In summary, the receive echo window is too short and there is not enough time between the transmit pulses to receive from a large scene. This is a physical limitation and there are techniques which can be applied to partially improve it. Some of these techniques are developed and analyzed in more details in chapter 5.

The Staring Spotlight, on the other hand, is not time limited. However, the use of a higher chirp bandwidth results in a huge amount of data that needs to be saved into the internal memory of the satellite. Combining this high data rate with the Stripmap image which is being acquired simultaneously, the Staring Spotlight scene size must be reduced in order to respect the satellite memory limitations. As this is more of an internal satellite limitation, it should not be fully attributed as a concurrent mode downside, but rather as a limitation of the previous generation of SAR systems. It is important to note that TerraSAR-X was launched in 2007 and is performing much longer than the initial expectations.

Finally, as the concurrent mode is still a project under development, the cause of the deterioration in the sidelobe parameters in the experimental Staring Spotlight image is still under investigation. The most plausible cause is the processing algorithm. The concurrent mode being in the early stages of development, there is still no specific processing tool to obtain the focused image from the raw data. Therefore, with further developments in the processing of the proposed mode, this anomaly in the Staring Spotlight impulse response is expected to be solved.

4.4 Ambiguity Assessment

Besides resolution, scene size and sidelobe ratios, which are undeniably important image parameters, there is also the ambiguity behavior that needs to be assessed. Chapter 3 analyzed the impact of the PRF selection on ambiguities. The uniqueness of the concurrent mode requires very high PRFs in order to accommodate both modes in a single acquisition. Therefore, an ambiguity assessment is essential in order to get a better picture of the real performance of the proposed mode.

The visualization of ambiguities, however, is not an easy task. Once it is desirable to obtain ambiguity-to-signal ratios of around −20 dB, the ambiguities will only show up as strong interferences in case there is a high backscatter discrepancy in the scene. The acquisition over Australia shown in this chapter is not a good example to assess ambiguities, as the scene is fairly homogeneous. Due to the specular reflection characteristic of calm water (low backscatter), the most suitable scenes to observe and assess ambiguities are generally water-to-land transitions.

From the motivation above, two water-to-land transition scenes were acquired. Once the acquisition over Australia showed to be successful, these new acquisitions were designed to use the same antenna patterns and PRF in order to keep most of the parameters constant. The objective now is only to assess ambiguities by using more critical targets. The areas of interest chosen are the city of Buenos Aires, the capital of Argentina, and the small city of Piúma in the state of Espírito Santo, Brazil. The Google Earth images of the areas and the Stripmap acquisition ranges (in green) are shown in Figs. 4.9a and 4.9b.

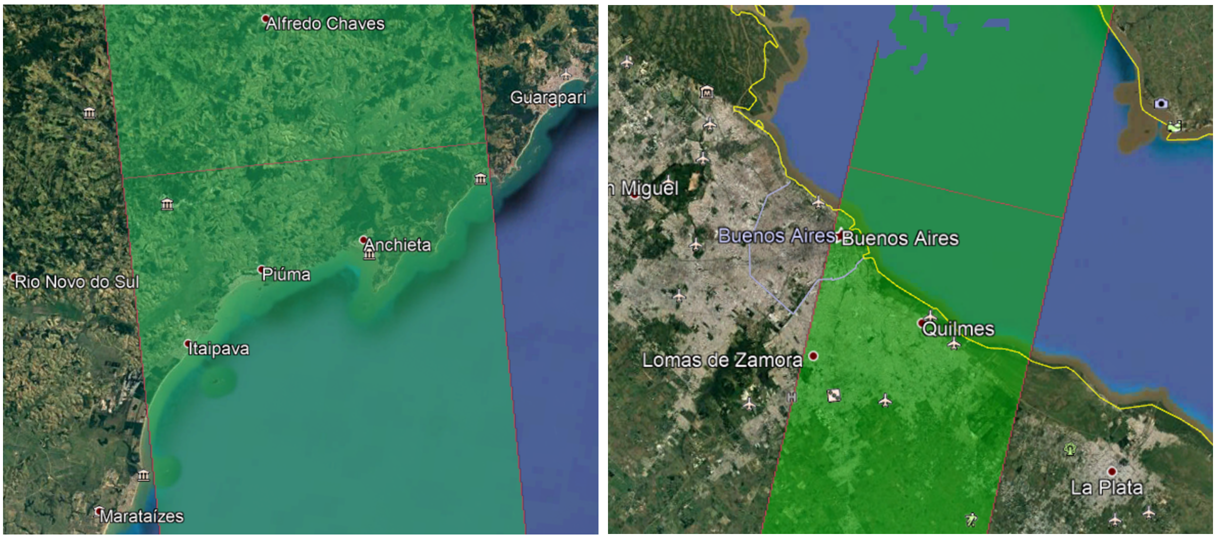

(a) Piúma-ES, Brazil.

(b) Buenos Aires, Argentina.

FIGURE 4.9 – Areas of interest to assess ambiguity performance of the concurrent mode.

The reasoning behind the choice of the cities is that they are intrinsically different in terms of building density and geographic profile. Therefore, the scenes will likely provide distinct data and conclusions, which will enrich the concurrent mode ambiguity analysis. As these acquisitions are focusing on the analysis of the ambiguity performance of the Stripmap part, the acquisitions are not optimized for the Staring Spotlight images. Those images are located in the water areas and therefore do not add much to the analysis.

4.4.1 Azimuth Ambiguities

The city of Piúma has a very low population density and an urban area with only approximately 22000 people. The region nearby consists mostly of open fields, the Atlantic Forest and some low mountains. Therefore, apart from the city center and a mining company (upper right of Fig. 4.10), there are not many buildings or potential strong scatterers in the region nearby. Given that the city and the ocean are roughly aligned in azimuth, azimuth ambiguities are expected to show up. The distance between the target and its first ambiguities in azimuth can be calculated by

$$D_{\mathrm{az}} = \frac{\lambda \cdot \mathrm{PRF} \cdot R_0}{2 \cdot v_{\mathrm{s}}} = \frac{0.031\ \mathrm{m} \cdot 3044.5\ \mathrm{Hz} \cdot 652.36\ \mathrm{km}}{2 \cdot 7680\ \mathrm{m/s}} \approx 4\ \mathrm{km}. \tag{4.8}$$

In the equation R_0 represents the slant range of closest approach and v_{s} the satellite speed.

The Stripmap image obtained from the city of Piúma is depicted in Fig. 4.10. As expected, there are strong azimuth ambiguities visible to the eye in the focused image. The yellow arrow depicts the distance between target and ambiguity calculated from the image and confirms the distance predicted theoretically.

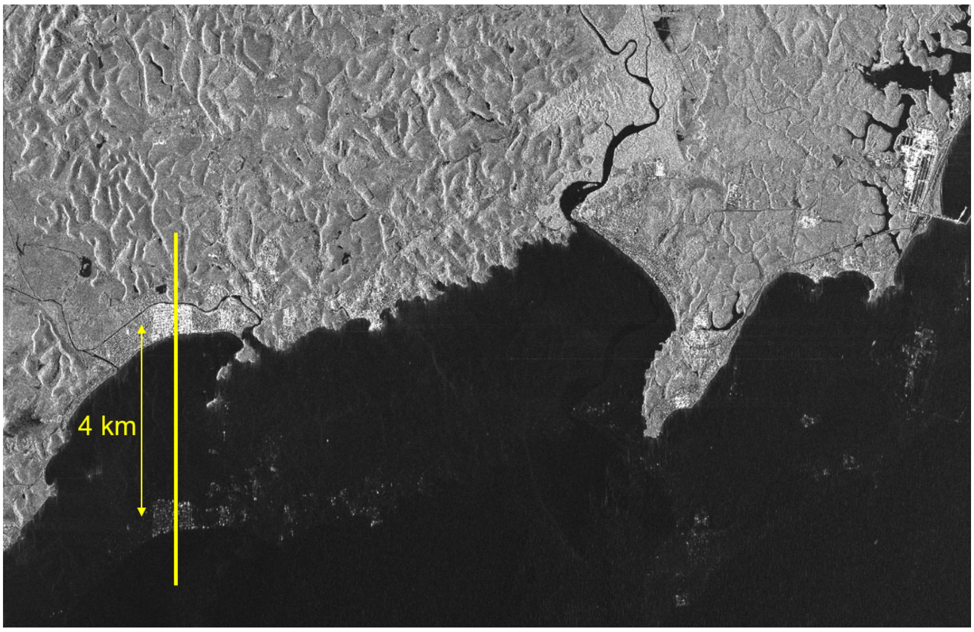

FIGURE 4.10 – Focused image of the experimental Stripmap acquisition over Piúma-ES, Brazil.

The AASR can be measured from the image obtained by comparing the city and the ambiguity response. Therefore, a cut in azimuth was performed as depicted by the yellow thick line in Fig. 4.10. In order to improve the accuracy of the measurement of the AASR, an averaging was done in range with 51 lines and additionally also a moving average of

101 samples was done in azimuth. The averaging can be seen as a low pass filter and has as objective the reduction of excessive noise. The plot shown in Fig. 4.11 depicts the cut obtained.

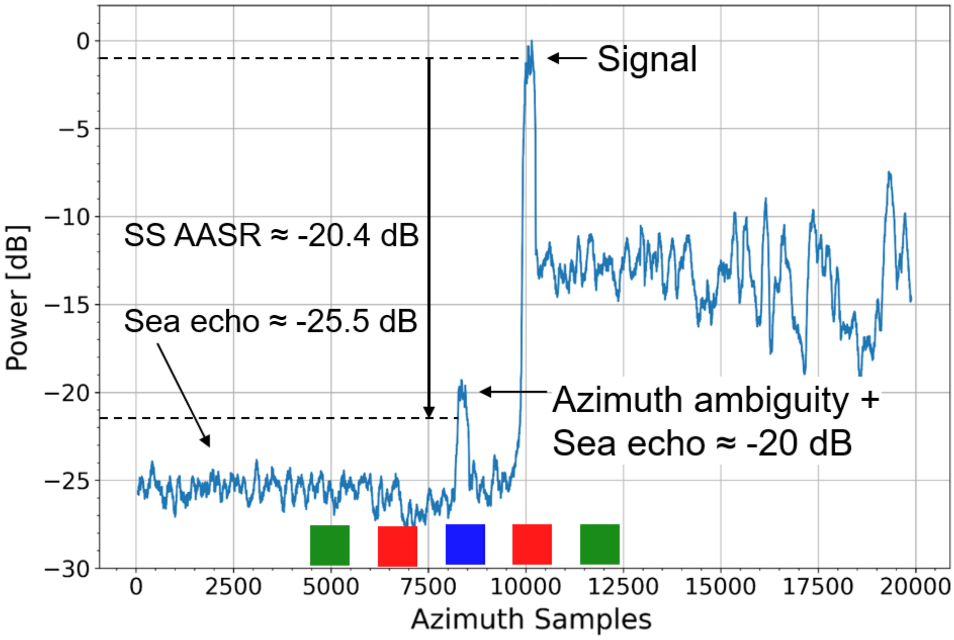

FIGURE 4.11 – Cut in azimuth over the azimuth ambiguity region of the experimental Stripmap acquisition over Piúma.

There are four very distinct regions in the plot. First, the city center, represented by the arrow 'Signal', is the strongest scatterer in the scene. Next and 4 km apart, the ambiguity caused by the city on the ocean is observed and pointed out by the 'Azimuth ambiguity + Sea echo' arrow. To the right of the city there are chains of low mountains and open fields, which have visibly lower backscatter when compared to the city. The same ambiguous signal as recognized in the open sea is expected to appear on the late-azimuth/right side of the city. However, the same power peak is not visible in this region due to its response – between -10 dB and -15 dB – being high enough to hide the azimuth ambiguity caused by the city. Finally, the weakest backscatter in the scene is naturally the ocean, at approximately -25.5 dB. The AASR can be obtained directly by comparing the powers from the city and from the ambiguity region.

It is worth noting that the lower peak in the plot consists not only of azimuth ambiguity from the city, but also of echoes from the sea itself. Visually and roughly ignoring the noise in the peaks, the total normalized power from the city is at around -1 dB. Moreover, the ambiguity with the sea echo being at around -20 dB and the sea echo at -25.5 dB, the azimuth ambiguity purely can be calculated to be at -21.4 dB. The difference between the power from the city and from the ambiguity can be seen as an approximation to the single-sided azimuth ambiguity-to-signal ratio ($\mathrm{AASR}_{\mathrm{SS}}$) and is equal to about -20.4 dB.

The understanding of this new concept becomes clearer with the help of the colored squares in the plot. The blue square depicts the target of the radar at a given moment in time. At this given satellite position, the main peak of the azimuth antenna pattern is pointing directly towards this region in the ocean represented by the azimuth samples where the blue square is. In this moment, the antenna receives ambiguous echoes from other azimuth positions, represented by the other squares. The red squares represent the first azimuth ambiguities, which are the most relevant ones due to the azimuth antenna pattern. Next, the green squares represent the second ambiguities and have a much lower effect on the total azimuth ambiguity power.

Using the same color scheme, the significance of each ambiguity can be better seen in the azimuth antenna pattern. This is depicted in Fig. 4.12, where it becomes clear that the first ambiguities are the most relevant ones. It is important to notice that the plot is in dB and, therefore, the absolute difference in power between the first and the second ambiguities are much higher than what they appear in the plot. For instance, the maximum power achieved by the first ambiguities is approximately -10 dB, whereas the second reach only -27 dB, which represents a power inferior by a factor of 50.

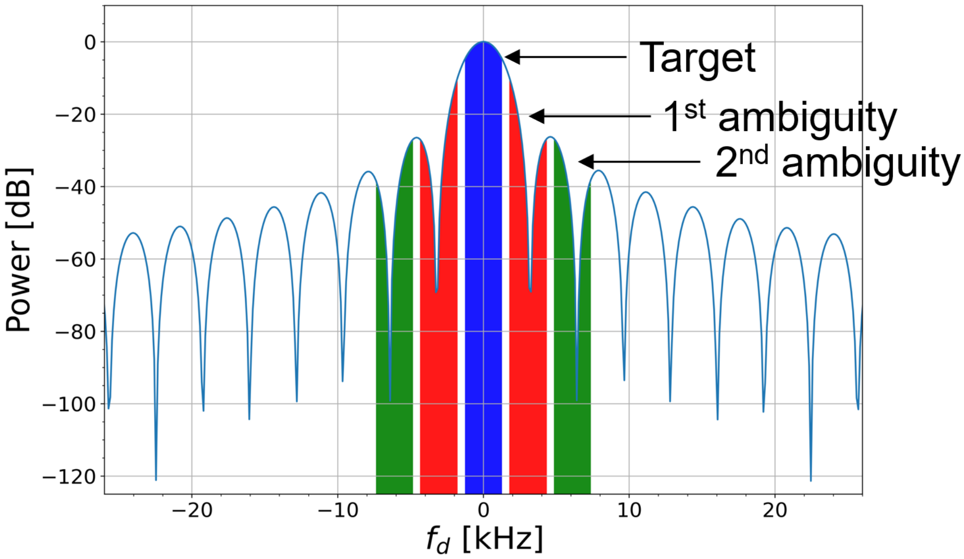

FIGURE 4.12 – Target and azimuth ambiguity positions in the antenna pattern using a PRF of 3044 Hz and an azimuth oversampling factor of 1.2.

Due to the symmetry of the azimuth antenna pattern, the same amount of power is expected from targets at positive and negative Doppler frequencies. Therefore, ignoring ambiguities of higher order, the total ambiguity power caused by the city can be seen as half the total power expected by the AASR prediction. Finally, the AASR can be related to the AASR_{SS} by

$$\text{AASR} = \text{AASR}_{\text{SS}} + 3\ \text{dB} = -17.4\ \text{dB}. \tag{4.9}$$

The value obtained is 1.7 dB off of the −19.1 dB (Table 3.1) predicted theoretically. There are many factors that contribute to this difference observed. The most important ones are the estimation of the sea echo power in the region of ambiguities and of the signal power, the visual measurement of the $\mathrm{AASR}_{\mathrm{SS}}$ from the plot and the accuracy of the theoretical prediction. Even after applying moving averages and averaging in range, the power coming from the city is still quite unsteady and can vary up to 3 dB. The same occurs at the sea, where there is a strong noise in its power. All these factors contribute, at some extent, to the 1.7 dB offset. Given the circumstances, this error is expected and acceptable for an experimental assessment.

The azimuth ambiguities, however, can still be improved during processing. In case lower ambiguities are required, it is not necessary to perform the acquisition again. Simply by reducing the processed azimuth bandwidth, i.e., increasing the azimuth oversampling factor, the ambiguities over the sea can be gradually vanished. As expected, this improvement comes with a trade-off. Once the processed bandwidth is reduced, so is the azimuth resolution. In short, it is required to abdicate of some azimuth resolution in order to improve the ambiguity performance. This trade-off is presented in Fig. 4.13, where the azimuth ambiguities gradually vanish as the processed bandwidth and the resolution are reduced.

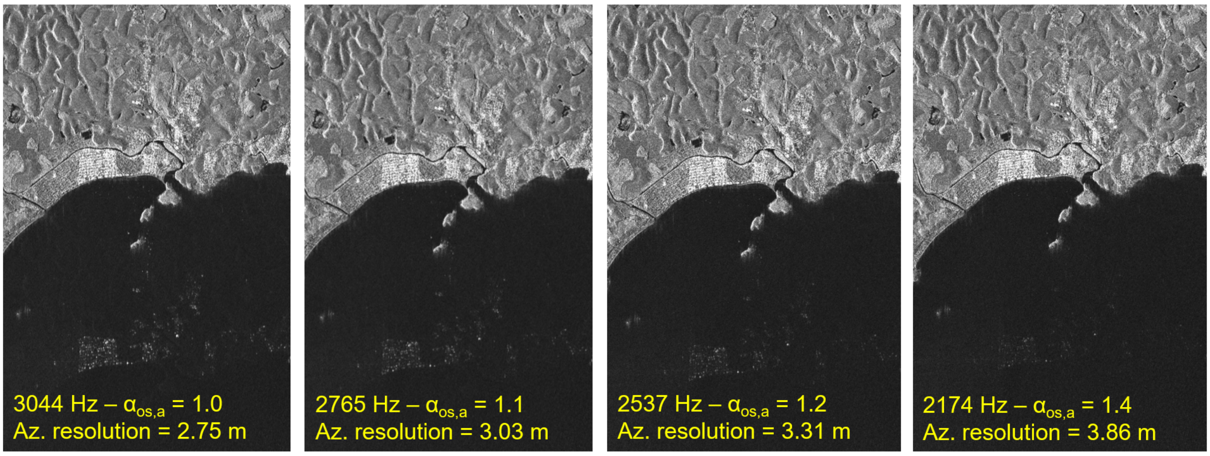

FIGURE 4.13 – Trade-off between resolution and ambiguity in the experimental Stripmap acquisition of Piúma. The processed azimuth bandwidth is reported together with the resulting azimuth oversampling factor $\alpha_{os,a}$.

4.4.2 Range Ambiguities

In contrast to the city of Piúma, the city of Buenos Aires is a huge metropolis with lots of buildings and potential strong scatterers. The conurbation, known as the Greater Buenos Aires, has a population of approximately 17 million people. Due to the dimension and urban characteristic of the city, it is expected to show up not only azimuth but also range ambiguities in the image. The slant range position of the first ambiguity can be calculated by

$$R_{\text{amb}} = R_0 \pm \frac{c \cdot \text{PRI}}{2}, \tag{4.10}$$

where R_{amb} is the slant range of the first ambiguity and R_0 is the slant range of the target being imaged.

Given the acquisition under analysis, the distance in ground range between the target and its first ambiguity in far range is equal to $D_{\text{rg}} \approx 39.4$ km. Due to the size of the city, there still are buildings and constructions 40 km away from the ocean, which are responsible for the range ambiguities in the scene. The Stripmap image obtained from the city of Buenos Aires is shown in Fig. 4.14. As expected, there are strong range ambiguities visible to the eye in the focused image. However, the ambiguities seem to be much stronger than expected, which motivates a deeper analysis.

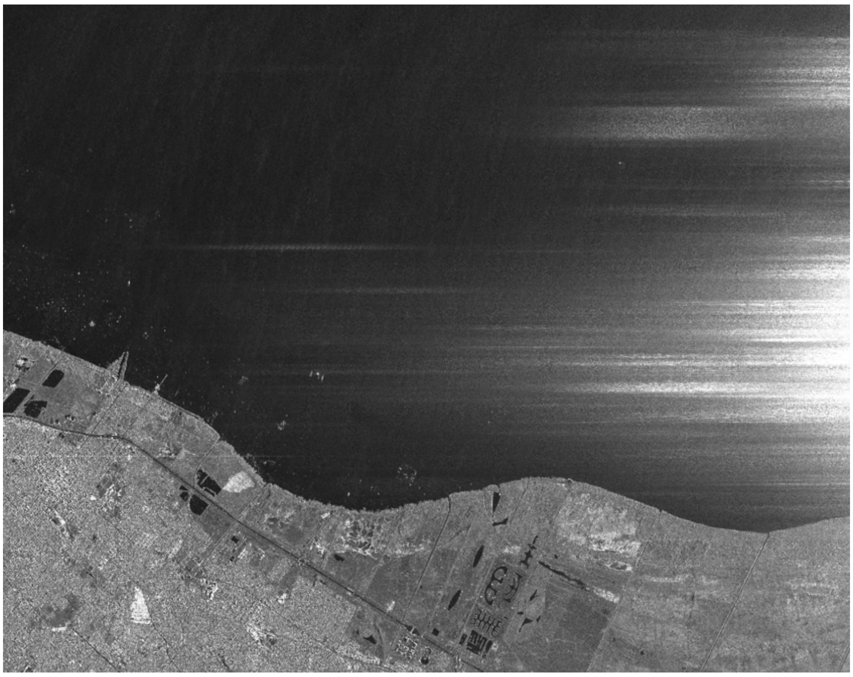

FIGURE 4.14 – Focused image of the off-nominal experimental Stripmap acquisition over Buenos Aires, Argentina.

In this concurrent imaging mode experiment, the Stripmap and the Staring Spotlight modes are using up and down chirps, respectively. Due to this fact, range ambiguities caused by the other mode would naturally show up as unfocused blurs. Besides, just like in azimuth, the first ambiguities in range are the most relevant ones due to the antenna pattern. Coincidentally, the first range ambiguities in a concurrent acquisition come from the other mode. Therefore, the strong interference in the image are likely cross range ambiguities, i.e., ambiguities caused by the other mode, by Staring Spotlight pulses in this case.

In order to check the hypothesis, further analyses are required. A fairly useful tool in digital signal processing is a spectrogram. Spectrograms are visual representations of the spectrum of frequencies of a signal as it varies with time. This signal processing tool can be used to analyze the ambiguities in the Stripmap image. However, it is important to analyze the data before focusing in order to avoid the spreading caused by an up-chirp focusing algorithm being applied to a down-chirp signal.

The spectrogram analysis is done by first obtaining a cut in range over the region with strong ambiguities in the raw data. Next, the cut is divided into many small consecutive chunks of data. By applying a Fourier transform, the spectrum of each of these chunks of data is obtained. The spectrogram is obtained by plotting all these spectrums in time. Longer chunks of data result in coarser resolution in time and finer resolution in frequency. The opposite effect occurs, i.e., shorter chunks of data result in better time resolution but worse frequency resolution. There is no optimum decision in this trade-off, but it is interesting to keep minimum resolution in each axis in order to keep a nice and clear visualization of the spectrogram. Finally, interpolation can be applied to improve visualization if necessary.

The spectrogram obtained in the range ambiguity area of the experimental acquisition over Buenos Aires is depicted in Fig. 4.15.

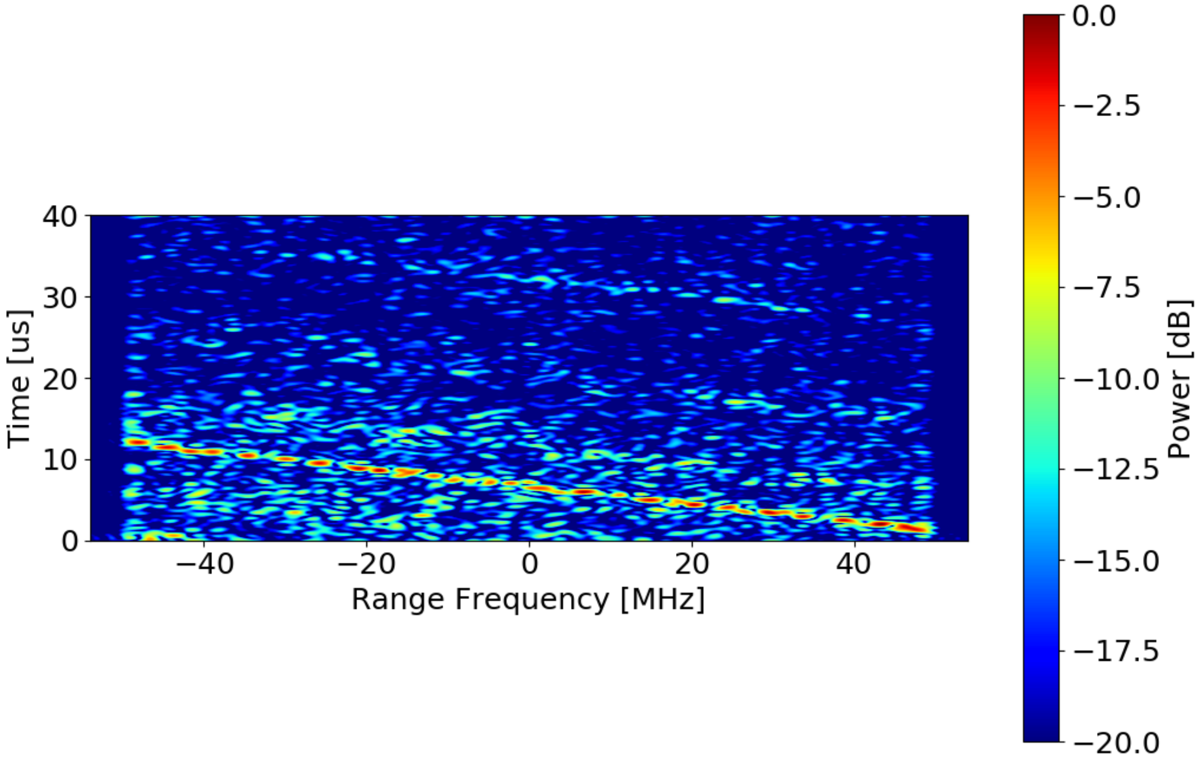

FIGURE 4.15 – Spectrogram of the range ambiguity region of the acquisition over Buenos Aires, Argentina.

The spectrogram obtained shows a very strong and clear signal with a linearly decreasing frequency. The signal frequency goes from 50 MHz to -50 MHz in roughly 11 μs, resulting in a chirp rate of -9.1 MHz/μs. The Staring Spotlight transmit pulse had a bandwidth of 300 MHz and a duration of 32.32 μs, resulting in a chirp rate of -9.28 MHz/μs. Therefore, the chirp slope and rate suggest a strong presence of Staring Spotlight pulses in the Stripmap image, confirming the hypothesis.

The hypothesis of a significant cross-interference between the modes has been confirmed. However, the ambiguity power observed was much higher than expected. Therefore, further investigation had to be carried out. An attentive comparison between the expected scene, shown by the green strip in Fig. 4.9b, and the actual imaged scene provided the answer to the strong ambiguities. Overlapping the green strips with the image obtained, a large offset in range was observed. In other words, the Stripmap scene was acquired with the wrong antenna pattern in elevation. This error caused the near range not to be illuminated by the main lobe, which drastically reduced the target power, making the ambiguities much more relevant and bright. This acquisition is, therefore, named as an ‘off-nominal acquisition’, and was acquired in this way due to the reasons as follows.

The concurrent imaging mode is not yet operationally available for TerraSAR-X. Each acquisition requires manual effort to generate the instrument commands. In order to limit the effort in manual commanding the scene over Buenos Aires was acquired using exactly the same instrument commanding as for the scene over the CRs in Australia, but shifted around the orbit. Because the scene in Australia was acquired in ascending geometry and the scene in Buenos Aires in descending, the orbit height is significantly different for both scenes. This difference caused a 4 km shift in height, which led the acquired scene in Buenos Aires to be shifted towards near range, as observed. From a different perspective, the echo window was not illuminated with the appropriate elevation antenna beam. Once it is desirable to know the quality of the Stripmap image when performing a proper concurrent mode acquisition, another acquisition over Buenos Aires was ordered but with the correct antenna pattern in elevation. The result is shown in Fig. 4.16.

FIGURE 4.16 – Focused image of the nominal experimental Stripmap acquisition over Buenos Aires, Argentina.

A visual comparison between the nominal acquisition in Fig. 4.16 and the off-nominal in Fig. 4.14 shows a considerable difference in range ambiguities. The proper selection of antenna patterns shows an acceptable final result, with weak azimuth and range ambiguities. It is worthwhile noting that these ambiguities will only show up in specific targets in which there is a calm water near strong scatterers. Besides, the azimuth ambiguities still can be reduced by slightly reducing the processed bandwidth.

Combining the great performance parameters discussed in the concurrent mode acquisition over Australia and the satisfactory ambiguity performance shown by the acquisitions over Piúma and Buenos Aires, the final conclusion is that the concurrent imaging mode is quite promising. The advantages of acquiring two images simultaneously are unquestionable and of vast use. Moreover, the concurrent mode comes with a possible reduction in swath width due to the high PRF and light ambiguities in critical scenes. In summary, to this point of development, the concurrent mode can be recommended to be vastly used, with exceptions when a high performance acquisition is required over critical areas such as water to land transitions or when a large swath is required.

5 Concurrent Imaging Derivations

The previous chapter presented a promising use of the concurrent imaging mode. The objective of this chapter is to further explore the mode to maximize its use and also to assess its potential from a statistical point of view. This chapter is not an attempt to exhaust the possibilities of the concurrent mode, but rather to explore and analyze some impactful and experimentally feasible derivations. The following proposals were thought to already be tested and applied in current generation SAR systems.

5.1 Multi-Target

The acquisitions shown on previous chapters are denoted as *overlapping* concurrent acquisitions. The naming comes from the fact that both the Stripmap and the Spotlight acquisitions are imaging the same area, i.e., the Spotlight is within the Stripmap image. However, since each mode is, to some extent, independent, they can also use distinct elevation antenna patterns in order to illuminate areas at different incidence angles. These sorts of acquisitions are, therefore, denoted as *non-overlapping* concurrent acquisitions.

The idea of acquiring over disjoint scenes opens new possibilities. One interesting derivation is to acquire, for example, two disjoint Stripmap images. This would not be meaningful in an overlapping acquisition as the Stripmap scenes would be the same. Besides, there are situations in which different clients want acquisitions over regions that are even hundreds of kilometers apart. In these cases, the non-overlapping concurrent imaging mode may end up being quite useful by performing both simultaneously. However, naturally not every two targets can be imaged with the concurrent mode due to timing restrictions.

The timing analysis for non-overlapping concurrent acquisitions is rather similar to the one described in Section 3.1. In short, given the desired target areas and the satellite orbit, the first step is to obtain the possible incidence angle ranges of each area for each flyover. Then, to each PRF that respects the ambiguity restrictions – between 5000 Hz and 7000 Hz, as shown in chapter 3 – the timing diagram provides the answer to whether the target areas respect both transmission and Nadir interference.

In order to test and validate the idea, a non-overlapping concurrent acquisition must be performed. Once again, the same region of Queensland will be imaged with the same PRF. The Spotlight mode will be performed over the exact same area as in the previous chapter. The Stripmap mode, conversely, targets a region at a higher incidence angle. Fig. 5.1 depicts every possible target of the non-overlapping imaging using the same PRF of 6088 Hz. The yellow strips are in ground range and they represent the possible targets from a timing point of view. Every two of them can be used in the acquisition. The regions chosen to be imaged are pointed by white arrows. The text in the box describes the incidence angle range and expected swath width of each strip. It is noticeable that target areas at higher incidence angles are tied to shorter scene sizes.

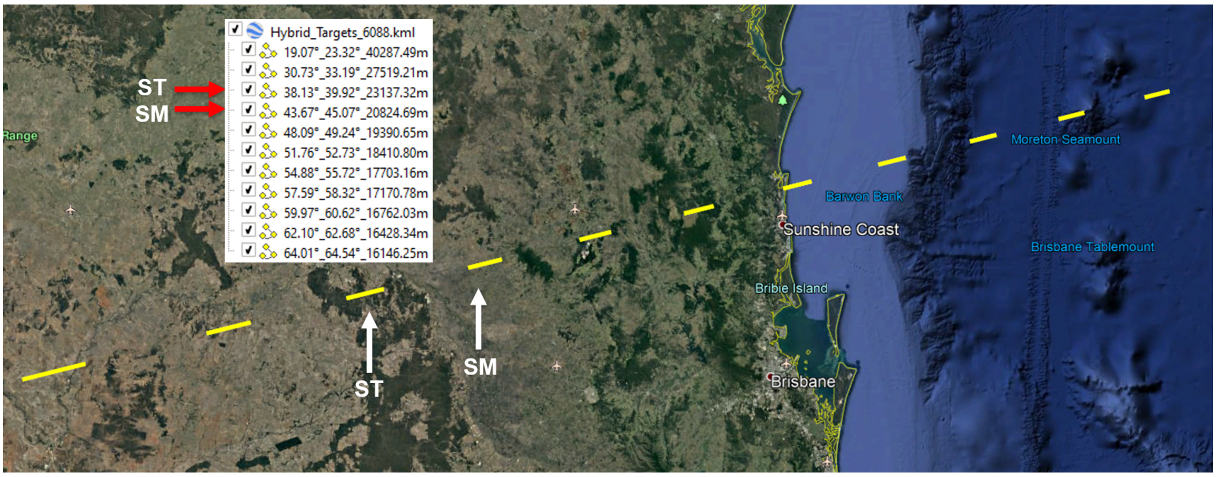

FIGURE 5.1 – Possible targets of the non-overlapping concurrent acquisition over Queensland using a PRF of 6088 Hz.

After processing, the non-overlapping experimental acquisition resulted in the two desired images. The Stripmap and the Spotlight images are shown in Figs. 5.2 and 5.3, respectively.

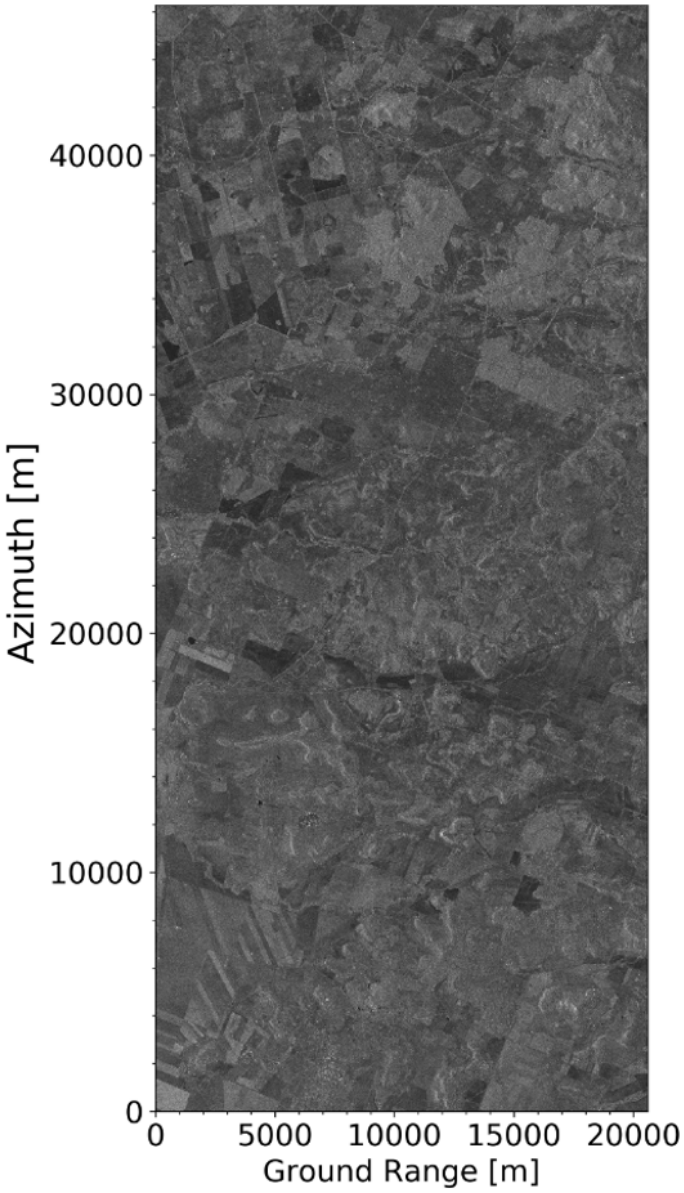

FIGURE 5.2 – Focused image of the experimental non-overlapping Stripmap acquisition over Queensland.

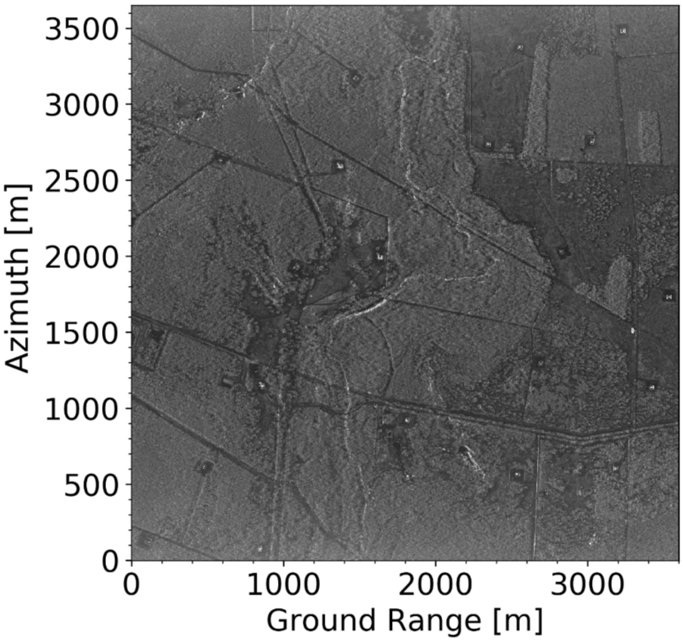

FIGURE 5.3 – Focused image of the experimental non-overlapping staring Spotlight over Queensland.

Corner reflectors are present in both scenes, which allows for an impulse response assessment. A point target analysis was carried out and pointed nominal performance in both acquisitions. Table 5.1 summarizes the performance parameters obtained in this non-overlapping acquisition.

TABLE 5.1 – Summary of the non-overlapping experimental SM/ST concurrent mode acquisition over Australia and its comparison with the expected results or the specifications.

Parameter		**Staring Spotlight**	**Expected**	**Stripmap**	**Expected**
Resolution	**Azimuth**	0.248 m	0.218 m	2.709 m	2.755 m
	Slant Range	0.593 m	0.589 m	1.765 m	1.767 m
Scene Size	**Azimuth**	3.65 km	x	46.1 km	x
	Ground Range	3.60 km	x	20.7 km	20.8 km
		Staring Spotlight	**Specification**	**Stripmap**	**Specification**
PSLR	**Azimuth**	23.5 dB	20.0 dB	30.6 dB	25.0 dB
	Slant Range	31.7 dB	25.0 dB	29.7 dB	25.0 dB
ISLR	**Azimuth**	23.7 dB	16.0 dB	21.6 dB	18.0 dB
	Slant Range	25.2 dB	18.0 dB	21.8 dB	18.0 dB

The non-overlapping concurrent mode has proven to also have great imaging performance. This enables very valuable possibilities in which disjoint areas can be imaged with different independent imaging modes. The concurrent imaging brings to the current generation of satellites a higher flexibility and image output rate, not giving up on imaging performance. The next sections discuss the Earth coverage of the concurrent mode. Finally, a multiple PRI proposal is presented aiming to improve the global availability.

5.2 Earth Coverage

The possibility of acquiring over multiple regions with the concurrent mode leads to questioning whether a given set of targets on Earth can be simultaneously imaged. The concept of *availability* arises as the solution. Therefore, one can say that a concurrent acquisition is *available* if any two targets on Earth's surface respect both timing and ambiguity constraints for a selected PRF.

A limiting factor on TerraSAR-X is that the antenna pattern of reception must be the same as the previous transmission due to commanding restrictions. Consequently, there must be an even number of traveling pulses at the moment of reception of each mode. Studies are being carried out to bypass this limitation. Besides, the echoes from each target must arrive at the antenna when the radar is in reception mode with the proper antenna pattern. Receiving while the system is in transmission mode is not possible due to the high difference in power, and the Nadir echoes must be avoided due to their strong backscatter profile (Balkoski; Bordoni, 2012; Wollstadt; Mittermayer, 2008).

The following subsections present a more detailed numerical analysis of the availability in specific scenarios.

5.2.1 Availability for Overlapping Areas

A potential scenario is when both targets are within the same region of interest. Illustratively, they can be considered to be part of the same yellow strip from the multiple ones depicted in Fig. 5.1. In order to obtain a quantitative measurement of the Earth coverage, a specific target and the minimum required scene size of each mode must be specified. Considering the initial idea of a Spotlight patch within a Stripmap scene, the timing constraint is reduced to only analyzing the Stripmap acquisition, as the Spotlight one is much shorter in range and within the same region. In addition, the Stripmap scene is required to be 30 km wide symmetrically around the simulated point target. Situations in which one imaging area is entirely within the other are named *overlapping areas.*

The simulation described here considers one hundred thousand uniformly distributed random points on the Earth's surface. For each of them, the satellite orbit and available PRFs are checked in terms of timing and ambiguity constraints. The acquisition is judged as being available if both the timing is feasible without transmit or Nadir interference and the predicted ambiguity levels are below a predefined threshold. Besides, the scene center incidence angle must be fixed within a specific range in order to guarantee sufficient performance in terms of range resolution, range ambiguities, shadowing and layover (Massonnet; Souyris, 2008). The *full performance* range is defined as the incidence angles between 20° and 45° (Fritz; Eineder, 2013). A looser restriction comes with the *data collection* range, which is defined as the incidence angles between 14° and 60°. One simulation for each of the defined ranges is performed for overlapping areas.

Due to the TerraSAR-X orbit being sun synchronous, there is a higher fly-over rate for targets at higher latitudes (D'Amico *et al.*, 2004). Therefore, one can expect targets near the equator to have the lowest availability. Fig. 5.4 depicts the availability rate for the scenario described, i.e., random targets with a 30 km symmetric scene and proper PRF for a concurrent imaging. The figure shows that the probability of a target being available increases at higher latitudes. In Fig. 5.5, the latitude is fixed to zero to obtain a roughly worst-case result and the available targets are shown in green, while those in red are not available given the constraints imposed.

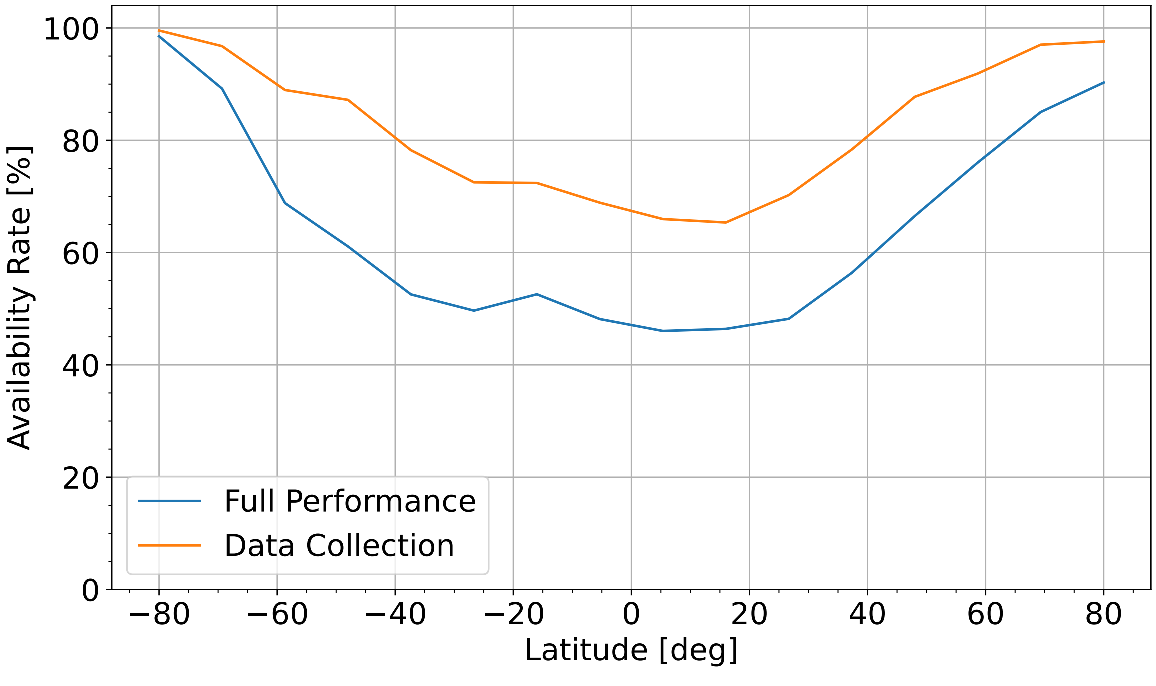

FIGURE 5.4 – Availability rate in terms of latitude for the overlapping concurrent mode. The plot represents the probability of a random point at a certain latitude to be accessible for a 30 km/5 km SM/ST concurrent acquisition. SM scene must extend at least 15 km to far and near range to obtain a 30 km symmetrical scene. The blue line represents the full performance incidence angle range, while the orange line represents the data collection range.

FIGURE 5.5 – Available targets at latitude zero are depicted in green, whereas areas which are not accessible with the concurrent imaging technique are depicted in red. A symmetrical 30 km/5 km SM/ST overlapping scenario is considered. Scene center incidence angle must be within the data collection range.

The results obtained show that even at low latitudes, the availability remains at least above 65% for the data collection range and 45% for the full performance range. This represents reasonable Earth coverage, and the mode can be considered to be widely available. However, there is clearly room for improvement, as a close to 100% overall availability would be of great value.

The simulations here are intended to more homogeneous scenes. Highly sensitive acquisitions in terms of ambiguities would need tighter PRF restrictions to avoid image degradation. These scenes are typically regions with high contrast in backscatter, like cities close to the sea. In these cases, the concurrent mode at the actual state of development with the PRF range from 5 kHz to 7 kHz could degrade the images. These specific situations have not been considered in the simulations.

5.2.2 Availability for Non-overlapping Areas

The applications in which the regions of interest are at different yellow strips, according to Fig. 5.1, are named *non-overlapping areas.* Earth coverage statistics can be similarly obtained by availability simulation. For non-overlapping areas, other scenarios are analyzed. Not only SM/ST but also SM/SM acquisitions are investigated. The first scenario is a 20 km or 30 km Stripmap scene combined with a 5 km Spotlight one. As a second case, two 20 km Stripmap scenes are considered.

The simulation considers two targets randomly placed at the equator separated by a distance of up to 250 km. Every fly-over resulting in an incidence angle between 14° and 60° (data collection range) is considered. Then, the available on-board PRFs are checked in terms of timing and ambiguities constraints. The targets must only be within the required swath width, and this represents a looser restriction compared to the symmetrical scene in the previous simulation. Besides, the latitude has been fixed to zero to obtain a worst-case scenario. Figs. 5.6 and 5.7 depict the availability for the SM/ST and SM/SM simulations, respectively. Twenty thousand random targets were simulated.

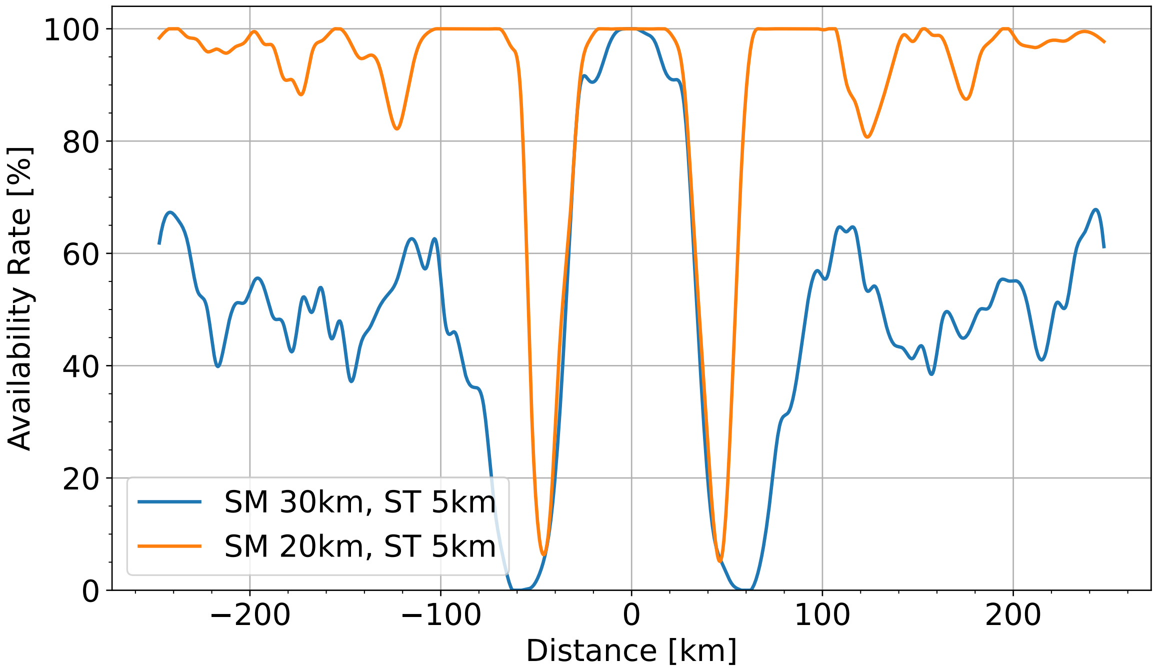

FIGURE 5.6 – Availability rate in terms of the distance between the targets for non-overlapping concurrent imaging acquisitions. The plot depicts the probability of two random points on the equatorial line to be accessible in a SM/ST concurrent acquisition. Targets must be within the imaged swath, not necessarily in its center.

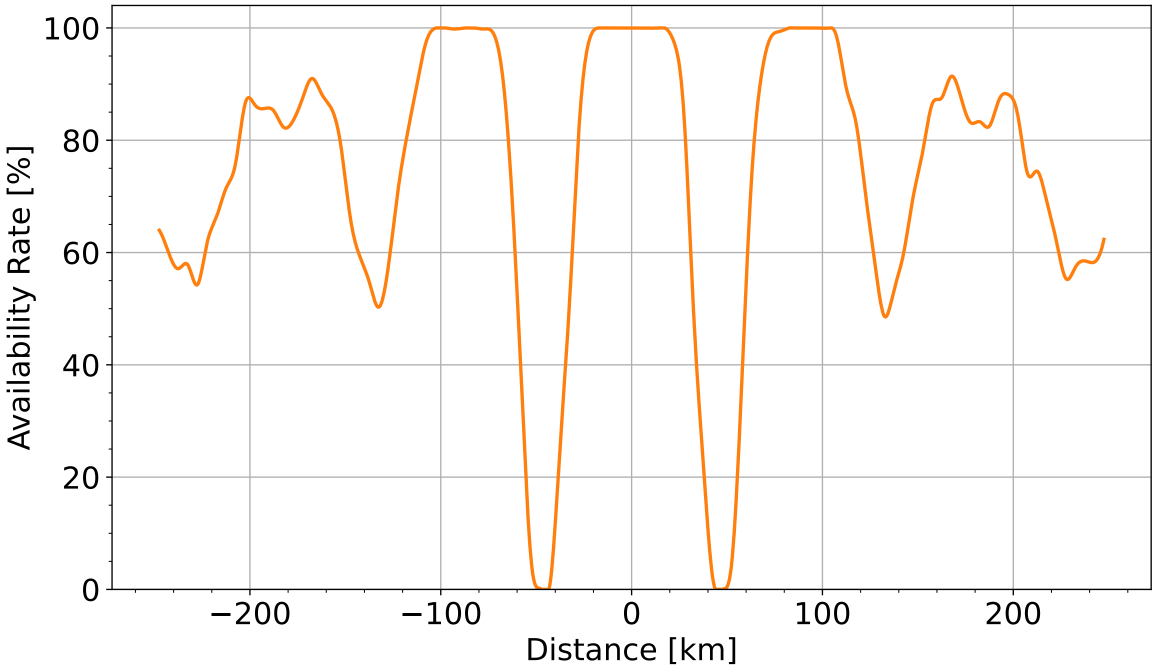

FIGURE 5.7 – Availability rate in terms of the distance between the targets for non-overlapping concurrent imaging acquisitions. The plot depicts the probability of two random points on the equatorial line to be accessible in a 20 km/20 km SM/SM concurrent acquisition. Targets must be within the imaged swath, not necessarily in its center.

The non-overlapping simulation represents a generalization of the overlapping one, as for distances near zero both acquisitions would be on the same yellow strip (Fig. 5.1), i.e., within the same area of interest. However, since here the targets must not necessarily be in the scene center, the availability climbs to 100% for overlapping areas. When the distance is between 40 km and 60 km, the availability drops down to zero. This effect is mainly caused by the fact that reception cannot take place while the radar is transmitting.

Considering the 30 km/20 km SM/ST scenario, Fig. 5.6 shows an approximately 50% availability for distances greater than 100 km. The low availability is caused mostly by the limited number of PRFs that enables the acquisition of a 30 km scene because of the limited echo window length for high PRFs. Reducing the Stripmap scene size to 20 km, the availability oscillates between 80% and 100% overall, only going to zero for distances from 40 km to 70 km.

Fig. 5.7 represents the Stripmap scene size reduction from 30 km to 20 km, and considers another 20 km Stripmap scene instead of the 5 km Spotlight. Comparing to the previous simulation, this is an intermediate scenario in terms of availability. The simulation returned an availability oscillating between 50 and 100%, only dropping down to zero for distances between 30 km and 60 km.

5.3 Multiple PRI

In concurrent acquisitions, the reception alternates between the modes. For a fixed PRI, the echo window length of each mode is the same and must be long enough to accommodate both scenes. Maximizing the swath width in Stripmap acquisitions is usually desired. Taking a SM/ST concurrent acquisition as an example, the SM echo window is totally utilized to maximize the swath width. Conversely, the ST echo window has very poor use of the time domain, as only roughly 5 km are being imaged. Fig. 5.8 depicts this bad use of time as the ST echo window is not completely used. Keeping the effective PRI constant, increasing the SM echo window, and reducing the ST echo window would greatly benefit the time domain use efficiency. The effective PRI can be obtained by the sum of the individual PRIs: $T_{\text{PRI,eff}} = T_{\text{PRI,SM}} + T_{\text{PRI,ST}}$.

To concurrent SM/ST acquisitions, the multiple PRIs idea can be summarized by

$$T_{\text{PRI,SM}} = \frac{T_{\text{PRI,eff}}}{2} + T^*, \tag{5.1}$$

$$T_{\text{PRI,ST}} = \frac{T_{\text{PRI,eff}}}{2} - T^*, \tag{5.2}$$

where T^* represents the exchange of time duration between the echo windows of the modes.

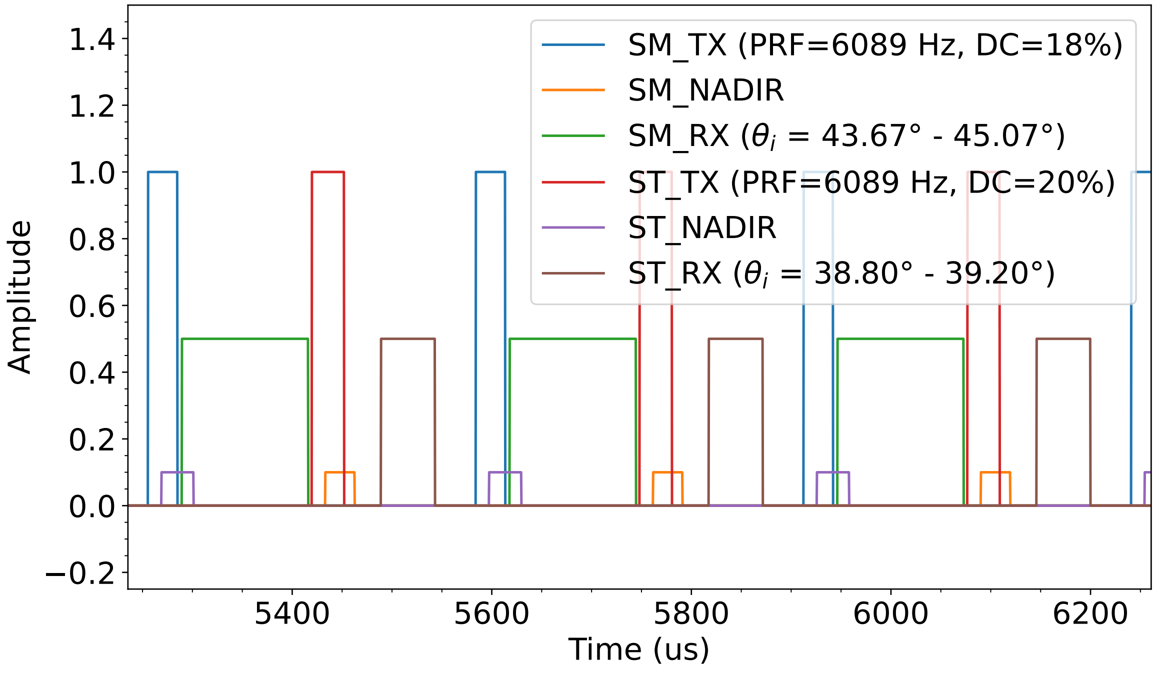

FIGURE 5.8 – Signals in time for a fixed PRI acquisition. Amplitude values are for illustration only. The figure shows that the ST echo window is not completely used, representing a less efficient system.

5.3.1 Modified Timing Diagram

The idea of increasing the echo window of one mode by reducing the other can be seen as each mode having a different PRI, or PRF. This subsection proposes and evaluates the multiple PRIs idea. The main objective is to achieve gains in flexibility, efficiency, and availability in concurrent imaging acquisitions. The improvement is not restricted only to SM/ST, but to any possible combination.

The typical method to determine the PRFs that respect timing constraints is the timing diagram (Curlander; McDonough, 1991), also known as diamond diagram. Given the target position by its incidence angle (θ_i), the satellite height and the duty cycle (DC), the timing diagram as shown in Fig. 2.2 indicates the PRFs in which there are neither Nadir nor transmission (TX) interference.

In the case of the concurrent mode with different PRIs, a more generic approach is required as there is one extra degree of freedom. The modified timing diagram presented in Fig. 5.9 is proposed for the concurrent imaging mode with multiple PRIs. Customarily when designing an acquisition, one or more targets on the Earth's surface are predefined. Fixing the incidence angle of a target and the duty cycle for each mode, the modified timing diagram indicates every possible PRF combination that respects the timing constraints. Effective PRFs lower than 2.5 kHz are discarded as they result in unsatisfactory azimuth ambiguities. Interference with the Nadir echo and the radar transmission are depicted in purple and green, respectively. Available PRF combinations are the remaining white regions.

To assess whether a PRF combination respects the timing constraints for an extensive scene, multiple modified timing diagrams must be checked for the whole incidence angle range of interest. This extra dimension of simulation directly results from the additional degree of freedom imposed by the use of different PRIs in each mode.

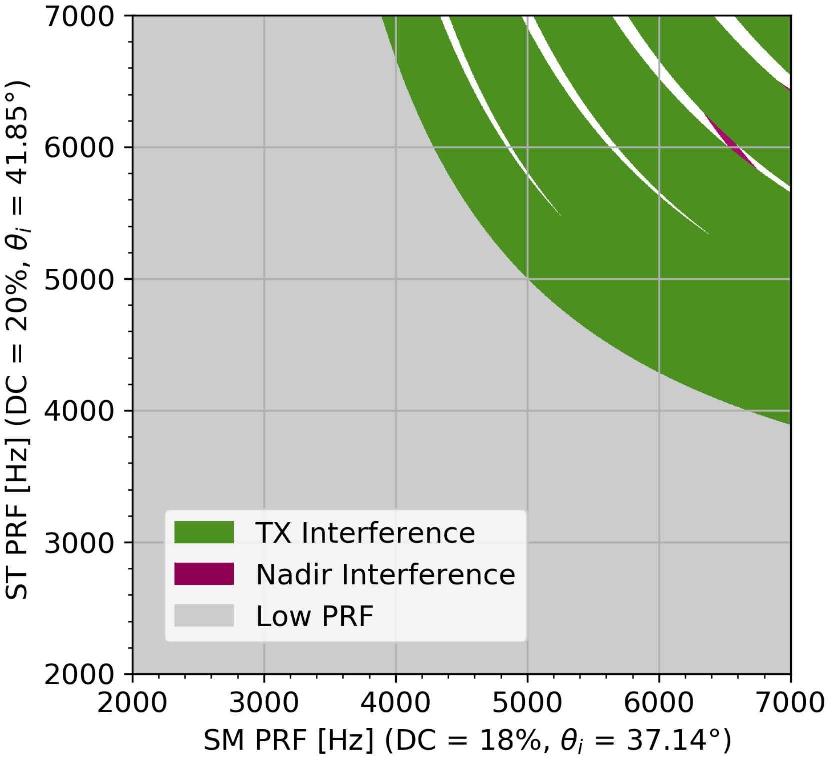

FIGURE 5.9 – The modified timing diagram for an orbit height of 519 km. The green areas indicate transmit interference, the purple Nadir interference and the gray low performance PRFs. Both types of interference need to be avoided by proper PRF selection for the incidence angles of interest. Those usable PRFs combination are depicted by the white areas. Each axis represents one acquisition mode attached to a duty cycle and a target.

5.3.2 Swath Width Evaluation

When designing a real acquisition, assessing the scene extension is a mandatory step to guarantee the minimum specification. Naively, one could think of plotting multiple modified timing diagrams for each incidence angle and checking one by one, but this is not a very practical approach. Given two targets and a PRF combination, however, each scene's maximum swath width is a fixed value that can be obtained from the timing analysis.

A lower PRF is expected to provide larger scene sizes, as the available echo window is longer. This approximation, however, is not always true as there are interference events that can eventually fall inside the receive echo window. This effect is visible for an exemplary concurrent acquisition in which the Stripmap mode has a duty cycle of 18% and images a target at an incidence angle of 37.14°. In comparison, the Spotlight has a DC of 20% and images a target at an incidence angle of 41.85°. In this scenario, the PRF combination 5 kHz in SM and 7 kHz in ST results in a 30 km swath width for the SM acquisition. Reducing the SM PRF to 4.4 kHz reduces the swath to only 12 km, as a Nadir echo appears in the receive echo window. Fig. 5.10 summarizes the SM swath width for the available PRFs obtained in Fig. 5.9.

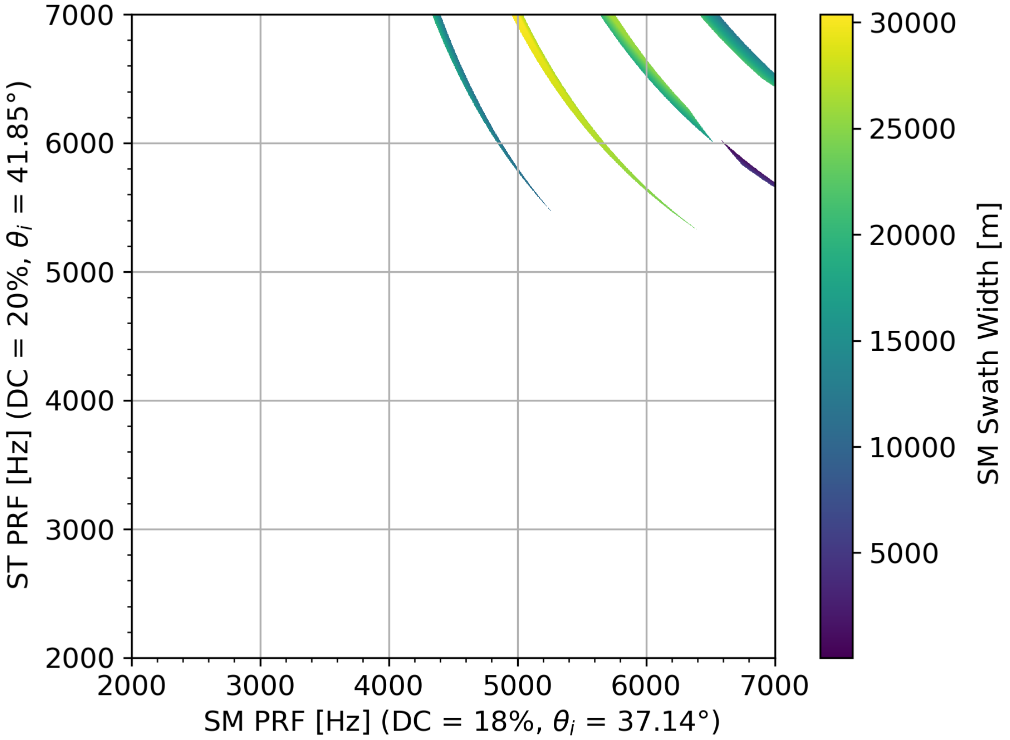

FIGURE 5.10 – Stripmap swath width in meters for multiple PRIs concurrent acquisitions. The SM mode utilizes a duty cycle of 18% and images a target at an incidence angle of 37.14°.

The swath width is one additional performance parameter that can be used to define the optimum PRFs. Its application widely varies based on the acquisition. For SM/SM acquisitions, as an example, the swath width of both images can be summed to maximize the total scene extension. A minimum scene size for each image may also be defined. In summary, the swath width analysis greatly depends on the desired imaging performance, being the main factors the required scene size of each mode and the available PRFs.

5.3.3 Global Availability Improvement

The proposal of having different echo window durations for each mode leads to a more efficient and flexible use of the time domain. Consequently, certain acquisitions that are not feasible with fixed PRIs may become realizable with different PRIs. A global availability improvement is expected in concurrent acquisitions using multiple PRIs. This subsection aims to analyze the effect of multiple PRIs on the Earth coverage of the concurrent imaging mode using TerraSAR-X. The improvement in availability for the same scenarios presented in subsection 5.2.2 is investigated.

The first scenario of analysis is a concurrent acquisition comprised of one 30 km Stripmap and one 5 km Spotlight scene separated by a distance of up to 250 km. This SM/ST combination represents the original scenario to which the concurrent imaging mode was designed. Besides, these scene sizes are approximately the standard values for operational acquisitions. Therefore, managing to perform these sorts of acquisitions would be ideal. Using fixed PRIs, a 50% percent average availability was observed in Fig. 5.6. In order to turn the concurrent imaging into an operational mode, improvement in availability is definitely necessary.

It is worth reiterating that in these simulations the randomized target must only be within the scene, not necessarily in its center. Besides, the availability rate describes the probability of two random targets separated by a given distance on the equatorial line to be accessible in a specific imaging configuration. The improvement in availability of the 30 km/5 km SM/ST acquisition is depicted in Fig. 5.11.

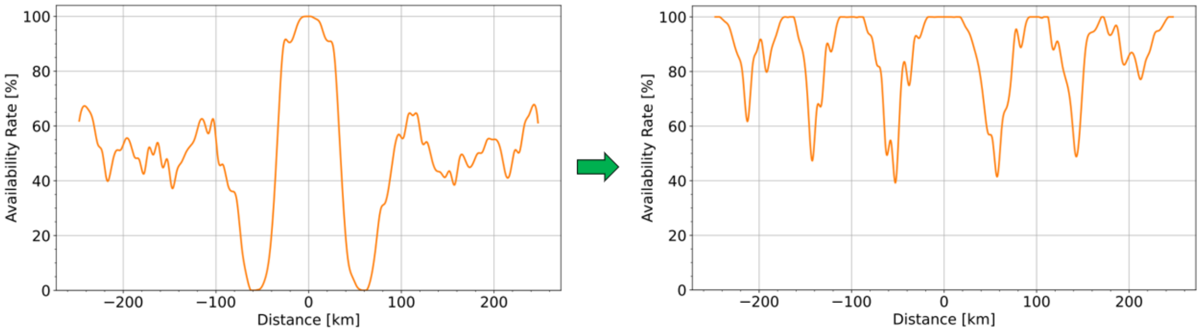

FIGURE 5.11 – Improvement obtained by the multiple PRI technique of the availability rate for non-overlapping 30 km/5 km SM/ST concurrent imaging acquisitions.

The result obtained shows that the use of multiple PRIs leads to a great improvement all over the distance range. The availability increases and oscillates between 50% and 100%. However, some plateaus can be seen at 100%, while 50% is only seen for a much lower amount of distances. Given that the simulation was run for targets at the equator and two operational modes were performed simultaneously, the availability obtained with multiple PRIs can be considered as acceptable.

The next scenario is the reduction of the Stripmap scene size to 20 km. Fig. 5.12 depicts the improvement obtained by the technique proposed.

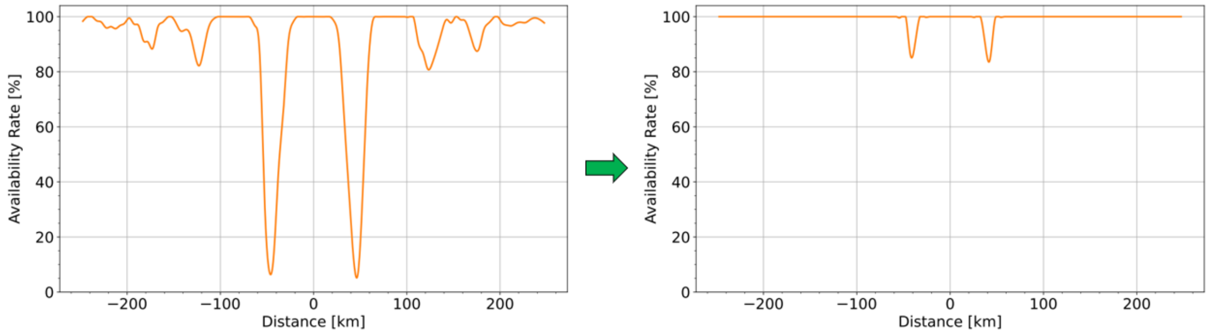

FIGURE 5.12 – Improvement obtained by the multiple PRI technique of the availability rate for non-overlapping 20 km/5 km SM/ST concurrent imaging acquisitions.

The improvement is clear as, for most distances, there is a 100% availability rate. The worst-case occurs for targets separated by approximately 40 km, in which the availability drops to a minimum of 85%. Considering that this result represents worst-case scenario around the globe, i.e., at the equator, the concurrent imaging mode with multiple PRIs has an almost 100% availability for anywhere on the globe when two 20 km Stripmap acquisitions are desired for targets up to 250 km apart. Even though the Stripmap length is not the nominal – 30 km –, this result is already quite important, as it guarantees a worldwide usability of the SM/ST concurrent mode.

Finally, the last scenario is the acquisition of two 20 km Stripmap scenes. The improvement provided by the multiple PRIs technique is presented in Fig. 5.13.

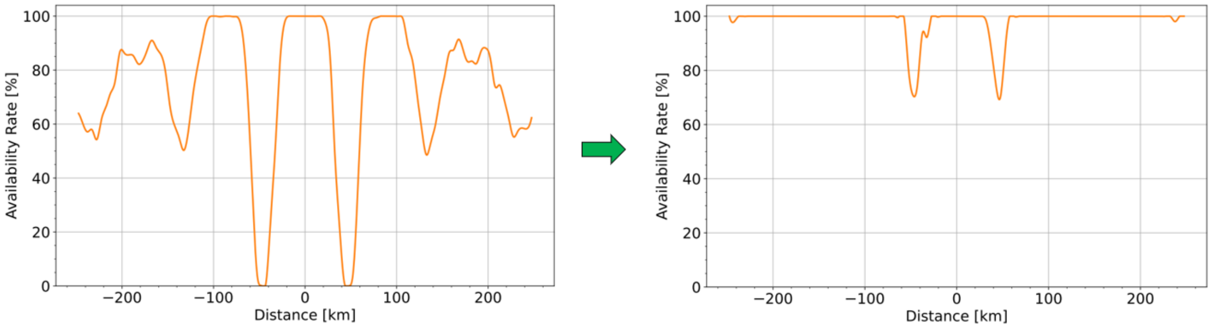

FIGURE 5.13 – Improvement obtained by the multiple PRI technique of the availability rate for non-overlapping 20 km/20 km SM/SM concurrent imaging acquisitions.

Once again, a roughly 100% availability throughout the distance range is obtained. A minimum of 70% is observed for targets separated by approximately 40 km. In summary, the concurrent mode can simultaneously produce two 20 km Stripmap images of two targets separated by up to 250 km almost everywhere on the globe.

6 Conclusion

6.1 Final Remarks

In this thesis, it was described a concurrent imaging technique that can acquire two SAR images simultaneously by a pulse-to-pulse interleaving of the imaging modes. The proposed mode is able to acquire an overview image in Stripmap mode and, at the same time, to provide a zoom on a target of high interest, e.g., an airfield, power plant, or other critical infrastructure. Because of the pulse-to-pulse interleaving, the mode is complex in terms of timing and ambiguity performance. A thorough analysis of these aspects for the TerraSAR-X case is provided. Additionally, an analysis of the global availability of concurrent acquisitions demonstrates the potential of this mode even on a global scale. For high and medium latitudes, an availability for nominal SM/ST overlapping acquisitions of more than 70% can be achieved. The experimental acquisitions and the analysis w.r.t. impulse response function and ambiguity characteristics highlight that the expected performance can be achieved. The results demonstrate the potential of this mode. By compromising scene size and ambiguity performance in a very controlled way, two SAR products can be acquired at the same time, either on the same or over disjunctive areas, as desired by the customer.

As the mode brings great versatility and an increased image output rate, developing methods to increase its availability is of great interest. The multiple PRIs technique is introduced and shown to bring significant improvements in the global coverage of the mode. By exchanging reception time duration between each mode, more flexibility and time efficiency were obtained. A quantitative analysis of the availability improvement confirmed the benefits of the technique. Finally, using the multiple PRIs technique, almost 100% availability was obtained for either two 20 km Stripmap or one 20 km Stripmap and one 5 km Spotlight acquisitions. Very high availability was also obtained for the nominal 30 km Stripmap and 5 km Spotlight concurrent acquisitions. Besides the already achieved promising results, there are ideas for further improvements that will be investigated in the near future.

6.2 Outlook of Further Work

The results shown in the previous chapters are already very promising. Nevertheless, there are opportunities for further improvements, e.g., with respect to ambiguity performance, swath coverage, and global availability of a potential operational concurrent mode for the TerraSAR-X mission.

Due to the necessity of high PRFs, the concurrent imaging technique is demanding from an ambiguity point of view. However, there are promising techniques to reduce ambiguities. One is the use of waveform encoding and dual-focus processing to reduce range ambiguities (Villano *et al.*, 2018a; Villano *et al.*, 2018b). The other is to employ multiple channels in azimuth, probably even in a bi- or multistatic configuration, so as to allow for an azimuth ambiguity suppression (Krieger *et al.*, 2004; Gebert *et al.*, 2009; Kraus *et al.*, 2019). At the current time, the TerraSAR-X and TanDEM-X satellites are still in close orbit formation. After completing the global digital elevation model (DEM) mission (Krieger *et al.*, 2007; Zink *et al.*, 2014; Rizzoli *et al.*, 2017), they are serving a multitude of scientific purposes. This close-formation could serve as an excellent testbed for bistatic concurrent imaging.

In this thesis, a concurrent Stripmap/Spotlight mode using the TerraSAR-X Staring Spotlight mode and a two-beam Stripmap were discussed. However, also a concurrent Stripmap/Spotlight using the TerraSAR-X High-Resolution Spotlight mode can be investigated in more detail in the future. It can further enlarge the trade-off between resolution and ambiguity performance. The High-Resolution Spotlight mode offers decreased azimuth resolution compared to Staring Spotlight, but with improved azimuth ambiguity performance and azimuth scene size (Fritz; Eineder, 2013).

Bibliography

Airbus Defence and Space. **TerraSAR-X Image Product Guide - Basic and Enhanced Radar Satellite Imagery**. [S.l.], mar. 2015. 24 p. Issue 2.1.

Balkoski, J.; Bordoni, F. Nadir echo properties, a study based on TerraSAR-X data. In: **Proc. 20th Telecommunications Forum (TELFOR)**. [S.l.: s.n.], 2012.

Calabrese, D.; Mastroddi, V.; Federici, S.; Serva, S. Discrete stepped strip (DI2S) for multi-swath acquisitions. In: **IEEE 5th Asia-Pacific Conference on Synthetic Aperture Radar (APSAR)**. [S.l.: s.n.], 2015. p. 191–195.

Cumming, I. G.; Wong, F. H. **Digital Signal Processing of Synthetic Aperture Radar Data: Algorithms and Implementation**. [S.l.]: Artech House, Incorporated, 2005. (Artech House signal processing library). ISBN 9781580530583.

Curlander, J.; McDonough, R. **Synthetic Aperture Radar: Systems and Signal Processing**. [S.l.]: Wiley, 1991. (Wiley Series in Remote Sensing and Image Processing). ISBN 9780471857709.

D'Amico, S.; Arbinger, C.; Kirschner, M.; Campagnola, S. Generation of an optimum target trajectory for the TerraSAR-X repeat observation satellite. In: **Proc. 18th International Symposium on Space Flight Dynamics**. Munich, Germany: [s.n.], 2004.

Danby, J. M. A. **Fundamentals of Celestial Mechanics**. [S.l.]: Willmann-Bell, Inc, 1988.

Fritz, T.; Eineder, M. TerraSAR-X basic product specification document. **DLR Public Document TD-GS-PS-3302**, n. 1.9, 2013.

Garthwaite, M. C.; Hazelwood, M.; Nancarrow, S.; Hislop, A.; Dawson, J. H. A regional geodetic network to monitor ground surface response to resource extraction in the northern surat basin, queensland. **Australian Journal of Earth Sciences**, Taylor and Francis, v. 62, n. 4, p. 469–477, 2015. Disponível em: <https://doi.org/10.1080/08120099.2015.1040073>.

Gebert, N.; Krieger, G.; Moreira, A. Digital beamforming on receive: Techniques and optimization strategies for high-resolution wide-swath SAR imaging. IEEE, v. 45, n. 2, p. 564–592, 2009.

Kraus, T.; Krieger, G.; Bachmann, M.; Moreira, A. Spaceborne demonstration of distributed SAR imaging with TerraSAR-X and TanDEM-X. IEEE, v. 16, n. 11, p. 1731–1735, 2019.

Krieger, G.; Gebert, N.; Moreira, A. Unambiguous SAR signal reconstruction from nonuniform displaced phase center sampling. IEEE, v. 1, n. 4, p. 260–264, 2004.

Krieger, G.; Moreira, A.; Fiedler, H.; Hajnsek, I.; Werner, M.; Younis, M.; Zink, M. TanDEM-X: A satellite formation for high-resolution SAR interferometry. v. 45, n. 11, p. 3317–3341, 2007.

Massonnet, D.; Souyris, J.-C. **Imaging with Synthetic Aperture Radar**. [S.l.]: EPFL Press, 2008.

Mittermayer, J.; Wollstadt, S.; Prats-Iraola, P.; Scheiber, R. The TerraSAR-X staring spotlight mode concept. **IEEE Transactions on Geoscience and Remote Sensing**, v. 52, n. 6, p. 3695–3706, 2014.

NASA. **GET TO KNOW SAR - Overview**. [n.d.]. `https://nisar.jpl.nasa.gov/mission/get-to-know-sar/overview/`. Accessed: 2021-06-04.

National Imagery and Mapping Agency. **Technical Report 8350.2 Third Edition**. [S.l.], 2000.

Rizzoli, P.; Martone, M.; Gonzalez, C.; Wecklich, C.; Tridon, D. B.; Bräutigam, B.; Bachmann, M.; Schulze, D.; Fritz, T.; Huber, M. *et al.* Generation and performance assessment of the global TanDEM-X digital elevation model. Elsevier, v. 132, p. 119–139, 2017.

Villano, M.; Krieger, G.; Moreira, A. Nadir echo removal in synthetic aperture radar via waveform diversity and dual-focus postprocessing. IEEE, v. 15, n. 5, p. 719–723, 2018.

Villano, M.; Krieger, G.; Moreira, A. Waveform-encoded SAR: A novel concept for nadir echo and range ambiguity suppression. In: . [S.l.: s.n.], 2018. p. 1–6.

Wikipedia contributors. **Orbital elements — Wikipedia, The Free Encyclopedia**. 2021. [Online; accessed 4-November-2021]. Disponível em: <https://en.wikipedia.org/w/index.php?title=Orbital_elements>.

Wiley, C. A. Synthetic aperture radars. **IEEE Transactions on Aerospace and Electronic Systems**, AES-21, n. 3, p. 440–443, 1985.

Wollstadt, S.; Mittermayer, J. Nadir margins in TerraSAR-X timing commanding. **Proceedings of the Committee on Earth Observation Satellites (CEOS)**, p. 4, 2008.

Zink, M.; Bachmann, M.; Bräutigam, B.; Fritz, T.; Hajnsek, I.; Moreira, A.; Wessel, B.; Krieger, G. TanDEM-X: The new global DEM takes shape. IEEE, v. 2, n. 2, p. 8–23, 2014.

Appendix A - Orbital Mechanics

A.1 Orbital Mechanics

In order to assess the performance of a given SAR acquisition, it is essential to know, among many other parameters, the power received, the ambiguity positions and the relative position between target and radar. One of the most common approaches is to consider a circular orbit and approximate the equations to obtain analytical results (Curlander; McDonough, 1991; Cumming; Wong, 2005). However, when dealing with a real satellite and developing a real acquisition mode, it is possible and of highly importance to consider the actual parameters involved. This chapter will present a brief description of the orbital parameters needed to evaluate a satellite SAR acquisition.

A.1.1 Keplerian Elements

The first information needed is the spatial position of the satellite, commonly known as the orbit. This trajectory of the satellite can be approximated as an elliptical Keplerian orbit. The main drawback of this approach is the fact that it ignores the effects of general relativity. However, given the fact that most satellites are endowed with control systems to keep them as close as possible to their nominal orbit, the influence of general relativity and of other celestial bodies' gravitational fields will be ignored.

As it would be expected, Earth is considered the *primary* while the satellite the *secondary*. In other words, Earth's center of mass is the point of reference for the satellite elliptical orbit. Among many possible mathematical descriptions, the Keplerian elements are six parameters capable of fully describing a Keplerian orbit (Danby, 1988).

The first two parameters are eccentricity (e) and semi-major axis (a). They are responsible for describing the shape and size of the ellipse in which the satellite is embedded. Eccentricity is a dimensionless parameter between zero and one used to mathematically describe the orbit shape. To get a better visual understanding, an eccentricity of zero represents a perfectly circular orbit, while an eccentricity of one represents a parabolic trajectory. The semi-major axis, on the other hand, defines the length of the longest semi-axis of the ellipse. The geometry of an ellipse is fully defined by its eccentricity and semi-major axis.

Besides the shape and size of the trajectory of the secondary, it is also important to define its orientation relative to the primary. The parameters responsible for that are the inclination (i) and the longitude of the ascending node (Ω). In order to understand these parameters, first some references must be defined. These references are known as the *reference plane* and the *reference direction* (Υ). As a matter of simplicity, in geocentric orbits, the reference plane is defined as the Earth's equatorial plane and the reference direction as the vernal equinox (First Point of Aries). The inclination of an orbit is defined as the angle between the reference plane and the orbit plane measured counter-clockwise when looking from the ascending node to the origin of the reference frame. When the plane of reference is defined as the equatorial plane, the longitude of the ascending node is commonly renamed as the right ascension of the ascending node (RAAN). The RAAN is defined as the angle between the reference direction and the direction of the ascending node (AN). The AN, on the other hand, is simply the intersection between the plane of reference and the satellite trajectory when going from the Southern to the Northern Hemisphere.

In order to completely describe the satellite trajectory, two additional constraints are necessary. These parameters are known as the argument of perigee (ω) and the true anomaly (ν). Being the perigee the point of closest approach between satellite and Earth, the argument of perigee is the angle between the ascending node and the vector connecting Earth's center of mass to the perigee. This parameter is responsible for defining the orientation of the conic section in the orbital plane. Finally, the true anomaly is what describes the position of the satellite inside its trajectory. It is defined as the angle in the orbital plane between the perigee and the satellite position measured in the direction of motion. Finally, these two parameters are often simplified into one parameter known as the argument of latitude (u), given $u = \omega + \nu$. It is a common practice to determine the position of a satellite which orbit is well defined only by its argument of latitude.

The previous description is summarized in Figure A.1.

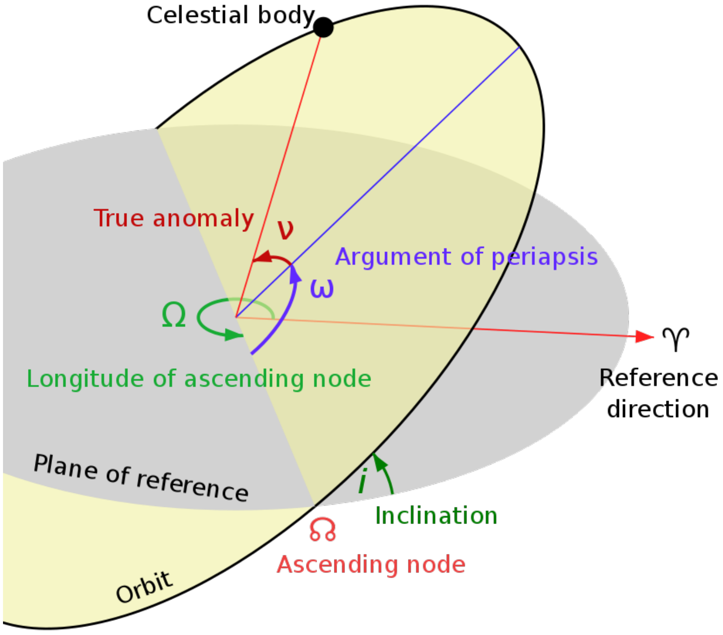

FIGURE A.1 – Diagram of orbital elements (Wikipedia contributors, 2021).

Table A.1 summarizes the Keplerian elements of TerraSAR-X, the satellite under analysis in this thesis.

TABLE A.1 – Keplerian elements of the satellite TerraSAR-X.

Eccentricity	**Semi-Major Axis**	**Inclination**	**RAAN**	**Argument of Perigee**
0.0001712	6886.39 km	97.44°	211.4446°	85.9782°

A.1.2 Coordinate Frames

From the previous discussion, the position of the satellite at any given point in time is well known. Therefore, the next logical step is to define a coordinate system in order to be able to mathematically express the position of satellites and targets on Earth in a common frame. Earth-centered coordinate frames are usually well-fitted to describe both a satellite in orbit and a given position on Earth's surface. These coordinate systems can be separated into two big categories.

The first group of Earth-centered coordinate frames is comprised of those that do not rotate relative to distant starts. The frames inside this group receive the name Earth-centered inertial (ECI) coordinate frames. In order to achieve this inertial feature, these frames do not rely on intrinsic Earth's characteristics, but on astronomical ones. For example, one of the most commonly used ECI frames is the J2000. This coordinate frame is defined using the mean equator and equinox on January 1, 2000 12:00 Terrestrial Time as a reference.

The other group of Earth-centered coordinate frames is comprised of those that rotate with Earth. In other words, coordinates of a fixed point on Earth do not change over time. Due to this characteristic, they are called Earth-centered rotational (ECR) or Earth-centered, Earth-fixed (ECEF). As expected, these frames use Earth's fixed points to define itself. For example, the World Geodetic System WGS 84 uses the IERS Reference Pole (IRP) as its z-axis and the intersection of the IERS Refrence Meridian (IRM) and the plane passing through the origin (Earth's center of mass) and normal to the z-axis as its x-axis. The y-axis is naturally a consequence of the other two axes by completing a right-handed orthogonal coordinate system.

From these descriptions, it can be noticed that each group of coordinate frames has its own advantages. Inertial systems are the most suited when interested in celestial objects. On the other hand, with rotational systems it is easier to describe terrestrial elements. When dealing with satellite SAR systems, the main objective is the acquisition of images from the Earth's surface. Therefore, WGS 84 was the coordinate system of choice throughout the following analysis.

A.1.3 WGS 84

As previously described, the WGS 84 is a world geodetic system created by the former National Imagery and Mapping Agency (NIMA), now National Geospatial-Intelligence Agency (NGA), with the objective of establishing a common worldwide geodetic reference system to ensure interoperability between different military and humanitarian activities worldwide (National Imagery and Mapping Agency, 2000). The WGS 84 coordinate system is graphically represented in Figure A.2.

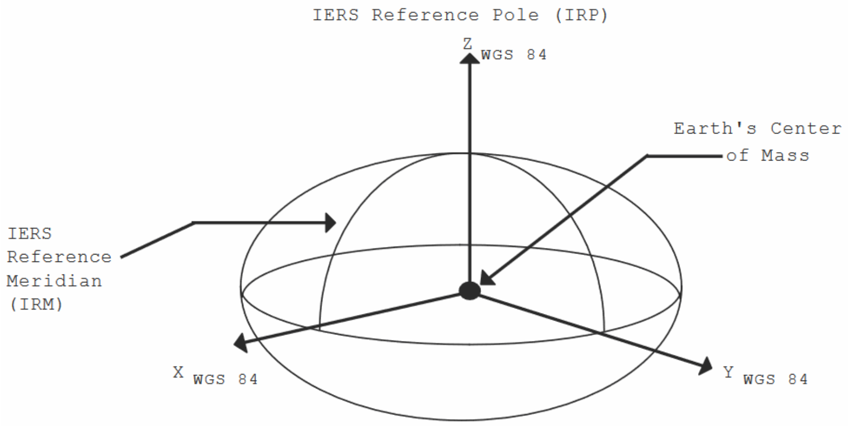

FIGURE A.2 – WGS 84 Coordinate System Definition (National Imagery and Mapping Agency, 2000).

Alongside the coordinate system, WGS 84 also defines a mathematical reference Earth's surface, known as the WGS 84 Ellipsoid. It was initially defined by four major parameters: the semi-major axis (a), the Earth's gravitational constant (GM), the normalized second degree zonal gravitational coefficient ($\overline{C}_{2,0}$) and the angular velocity (ω) of the Earth. In order to refine the model, these parameters have been adjusted throughout the years. Ultimately, the four defining parameters are a, GM, ω and flattening (f). The actual parameters are summarized in Table A.2.

TABLE A.2 – WGS 84 primary ellipsoid parameters.

Parameter	**Notation**	**Value**
Semi-major Axis	a	6378137.0 m
Reciprocal of the Flattening Factor	$1/f$	298.257223563
Angular Velocity of the Earth	ω	7292115 x 10^{-11} rad/s
Earth's Gravitational Constant	GM	(3986004.418 ± 0.008) x 10^8 m^3/s^2

From the basic parameters presented, it is possible to derive useful geometric and physical constants. These values are summarized in Table A.3.

TABLE A.3 – WGS 84 derived parameters.

Constant	**Notation**	**Value**
Semi-minor Axis	b	6356752.3142 m
First Eccentricity	e	8.1819190842622 x 10^{-2}
First Eccentricity Squared	e^2	6.69437999014 x 10^{-3}
Mass of the Earth	M	5.9733328 x 10^{24} kg

It is important to reinforce that the WGS 84 Ellipsoid is a model to approximate Earth's surface under a simple mathematical formulation. It must not be misunderstood as a perfect description of Earth's topography.

Finally, once the coordinate system and the ellipsoid are defined, it is possible to convert from geodetic coordinates (latitude ϕ, longitude λ, height h) into spatial coordinates (x, y, z) and vice-versa. This conversion is of high importance as targets on Earth's surface are usually defined by geodetic coordinates while the satellite position is given in spatial coordinates.

The satellite under analysis, TerraSAR-X, has a period of 11 days and therefore has a well defined nominal position over time. The target region must be chosen and then converted to the same coordinate system as the satellite. With this data, many useful information about the acquisition can already be acquired. For example, it is possible to determine the incidence angle, the relative velocity and the distance between radar and target. From a performance point of view, however, these results are still not enough to assess the acquisition quality.

A.1.4 Attitude Steering

In order to perform a quantitative analysis of a given acquisition, other three degrees of freedom are still necessary. Besides its translational position (x, y, z), the satellite rotational position is essential to know its orientation. With these six degrees of freedom, the satellite position and the antenna pointing direction are fully determined. By joining these data with the radar attributes, one can estimate performance parameters of a given acquisition. This section will briefly describe the attitude steering correction and the next chapters will define and obtain the image performance parameters.

The three rotational degrees of freedom can be represented and implemented by many different approaches. The two most common are by using quaternions or Euler angles with rotation matrices. The former approach requires one real and three complex values to define the satellite orientation, while the latter only requires three real values. The Euler angle method has a famous drawback known as Gimbal Lock (GL). However, given that the correction angles are not higher than 5°, it is not considered to be a constraint for the purpose of the following analysis. As it would be expected, each of these methods has its own advantages and disadvantages. In order to keep an intuitive and visually comprehensible approach to the detriment of an easier mathematically one, it was decided to use rotation matrices along with yaw, pitch and roll to correct the angular position of the satellite.

It is important to make it clear that the main goal of this analysis is to obtain the pointing vector of the antenna, i.e., where the antenna boresight is looking at. In the first approach, without any rotation matrix, the nominal orientation of the satellite is determined. This orientation can be obtained from the so called Nadir frame, where the z-axis is pointing along the opposite direction of the vehicle's position vector measured from the center of the Earth. The y-axis is aligned with the cross product of the negative position vector and the inertial velocity vector. The x-axis completes the right-hand system. Under this hypothetical situation with no rotation correction, the antenna normal vector would be given by the z-axis rotated 33.8° counter-clockwise around the x-axis.

However, due to the oblateness and rotational velocity of the Earth, the satellite orientation must be corrected in order to compensate these effects. This change in angular position can be written by yaw, pitch and roll along with rotation matrices. In other words, the vehicle must be rotate in order to ensure a correct antenna pointing and a nominal satellite performance. Mathematically speaking, any vector $\vec{v}_M$ given in the own satellite frame can be converted to Earth-fixed frame by applying the following rotation matrices

$$\vec{v}_{EF} = M_{EF \leftarrow N} M_{\text{yaw}} M_{\text{pitch}} M_{\text{roll}} M_{B \leftarrow M} . \vec{v}_M , \tag{A.1}$$

$$M_{\text{yaw}} = \begin{pmatrix} \cos(yaw) & -\sin(yaw) & 0 \\ \sin(yaw) & \cos(yaw) & 0 \\ 0 & 0 & 1 \end{pmatrix} \tag{A.2}$$

$$M_{\text{pitch}} = \begin{pmatrix} \cos(pitch) & 0 & \sin(pitch) \\ 0 & 1 & 0 \\ -\sin(pitch) & 0 & \cos(pitch) \end{pmatrix} \tag{A.3}$$

$$M_{\text{roll}} = \begin{pmatrix} 1 & 0 & 0 \\ 0 & \cos(roll) & -\sin(roll) \\ 0 & \sin(roll) & \cos(roll) \end{pmatrix} \tag{A.4}$$

$$M_{B \leftarrow M} = \begin{pmatrix} 1 & 0 & 0 \\ 0 & \cos(33.8^\circ) & \sin(33.8^\circ) \\ 0 & -\sin(33.8^\circ) & \cos(33.8^\circ) \end{pmatrix} . \tag{A.5}$$

The last matrix $M_{EF \leftarrow N}$ is responsible for transforming from Nadir to Earth-fixed frame and is given by

$$M_{EF \leftarrow N} = \begin{pmatrix} \text{axisX}[0] & \text{axisY}[0] & \text{axisZ}[0] \\ \text{axisX}[1] & \text{axisY}[1] & \text{axisZ}[1] \\ \text{axisX}[2] & \text{axisY}[2] & \text{axisZ}[2] \end{pmatrix} , \tag{A.6}$$

given that “axisX”, “axisY” and “axisZ” represent the Nadir frame axes written in the ECEF frame. This matrix simply represents a change of basis from the Nadir to the ECEF frame.

A.1.5 Antenna Pointing

From the previous description, it is clear how to convert any vector in the antenna frame into Earth-fixed (WGS 84). The reciprocal, therefore, is also well defined. In other words, knowing the satellite position and given any visible target on Earth’s surface, it is easy to obtain the pointing vector in the antenna frame. The pointing vector is defined as the vector connecting the satellite to a target on Earth. With this information, it is possible to obtain the gain of the antenna in that specific direction.

TerraSAR-X is endowed with a 4.78 m x 0.7 m active phased array antenna with a center frequency of 9.65 GHz. Its radiation pattern can be modeled by two independent axes, which define a plane perpendicular to the physical antenna normal. The axis along the longer side is defined as azimuth axis and the other as elevation. From this definition, the pointing vector can be decomposed into the three axes (azimuth, elevation and normal). This allows to obtain the angles in each independent axis and, therefore, obtain the gain of the antenna.

There are two main possibilities when defining the azimuth and elevation angles. Initially, decomposing the pointing vector into elevation, azimuth and normal would result in the coordinates of the vector in the antenna frame. Using the coordinates, one can define the antenna angles by

$$\theta_{az} = \arctan\left(\frac{\text{azimuth coordinate}}{\text{normal coordinate}}\right) \quad \text{and} \tag{A.7}$$

$$\theta_{elev} = \arctan\left(\frac{\text{elevation coordinate}}{\text{normal coordinate}}\right). \tag{A.8}$$

It is important to notice that these equations describe the angles in the plane defined by the normal vector and the axis.

The second possibility is to define the azimuth angle in the elevation plane. In this approach, the elevation angle remains the same, but the azimuth angle has a different definition, as described by

$$\theta_{az} = \arctan\left(\frac{\text{azimuth coordinate}}{\sqrt{\text{normal coordinate}^2 + \text{elevation coordinate}^2}}\right). \tag{A.9}$$

These possibilities are both useful and shall be properly understood and used in the correct situation. Naturally, the other way around is also possible. Given azimuth and elevation angles, one can derive the pointing vector. Using the WGS 84 Ellipsoid and the satellite position, the pointing vector results in a target on Earth's surface.

In summary, this appendix described how to better understand and use the satellite position and orientation. This information is extremely valuable as it allows one to obtain the antenna gain of any target at any point in time. Since all the necessary modeling of the Earth and the satellite has been done, the following chapters will focus on assessing the performance of different SAR acquisition modes and ultimately deriving and evaluating a new experimental mode.

FOLHA DE REGISTRO DO DOCUMENTO

1. CLASSIFICAÇÃO/TIPO TC	2. DATA 03 de novembro de 2021	3. DOCUMENTO Nº DCTA/ITA/TC-019/2021	4. Nº DE PÁGINAS 103

5. TÍTULO E SUBTÍTULO:
Concurrent Imaging Mode Design and Performance Prediction for Experimental SAR Acquisitions using TerraSAR-X

6. AUTOR(ES):
João Pedro Turchetti Ribeiro

7. INSTITUIÇÃO(ÕES)/ÓRGÃO(S) INTERNO(S)/DIVISÃO(ÕES):
Instituto Tecnológico de Aeronáutica – ITA

8. PALAVRAS-CHAVE SUGERIDAS PELO AUTOR:
Synthetic Aperture Radar (SAR); Concurrent Imaging Mode; TerraSAR-X; Ambiguities; Timing Analysis

9. PALAVRAS-CHAVE RESULTANTES DE INDEXAÇÃO:
Radar de abertura sintética; Imagens; Processamento de dados; Engenharia eletrônica.

10. APRESENTAÇÃO: **(X) Nacional** **( ) Internacional**
ITA, São José dos Campos. Curso de Graduação em Engenharia Eletrônica. Orientador: Prof. Dr. Renato Machado; coorientador: Thomas Kraus. Publicado em 2021.

11. RESUMO:

Stripmap e spotlight são os modos de aquisição mais utilizados e difundidos atualmente na indústria de radares de abertura sintética (SAR, *synthetic aperture radar*). Cada modo possui as suas próprias características e é usado de acordo com os requisitos do cliente. No entanto, existem situações nas quais ambos os modos são de interesse, tal como cenas nas quais não apenas uma visão geral, mas também uma imagem de resolução mais fina de uma pequena área se fazem necessárias. Nessas situações, a solução tradicional para obter ambas as imagens é esperar a próxima passagem do satélite pela região, o que pode demorar até 11 dias no caso do TerraSAR-X. O objetivo do trabalho de graduação em questão é projetar e validar uma técnica de aquisição concorrente no qual ambas as aquisições são executadas simultaneamente. Para isso, uma alta frequência de repetição de pulso (PRF, *pulse repetition frequency*) deve ser utilizada. Portanto, o trabalho foca, principalmente, nas restrições temporais e nas métricas de desempenho para avaliação das imagens. Por fim, são realizados experimentos práticos com o satélite em questão, utilizando dados reais para avaliar e validar o projeto e os resultados da técnica de imageamento proposta.

12. GRAU DE SIGILO:
(X) OSTENSIVO **( ) RESERVADO** **( ) SECRETO**